

CHARACTERIZATION OF MECHANICAL BEHAVIOR BASED ON
MICROSTRUCTURAL PHENOMENA IN $\text{Li}_2\text{O} \cdot 2\text{SiO}_2$ GLASS-CERAMICS

By

JEFFREY YATES THOMPSON

A DISSERTATION PRESENTED TO THE GRADUATE SCHOOL
OF THE UNIVERSITY OF FLORIDA IN PARTIAL FULFILLMENT
OF THE REQUIREMENTS FOR THE DEGREE OF
DOCTOR OF PHILOSOPHY

UNIVERSITY OF FLORIDA

1995

ACKNOWLEDGMENTS

I would like to express my sincere gratitude to the individuals who have assisted me on my journey through graduate school. Without the encouragement and guidance of these people my graduate studies and experiences at the University of Florida would not have been so enjoyable and rewarding.

My most sincere thanks go to my cochair, Dr. Kenneth J. Anusavice. I will always feel indebted to Dr. Anusavice for the sage advice and guidance that he gave me during my time in graduate school. Dr. Anusavice has always had my best interest at heart, and he will have my respect, admiration and friendship for life. Special thanks also go to Dr. Larry L. Hench, my chairman, for supporting me throughout my studies and for sharing his knowledge and insight with me. I wish him and his wife June much happiness and success as they embark on their adventures in England. I would also like to give special thanks to Dr. John J. Mecholsky Jr., for countless hours of thought-provoking discussion. I am lucky to know someone as generous with his time and as enthusiastic about his work as Dr. Mecholsky. My best regards also go to Dr. Arthur E. Clark, Dr. E. Dow Whitney, Dr. Peter Ifju, Dr. Peter Mataga and Dr. David Clark, who all contributed to my growth and development. I could not have selected a better group of advisors.

I must also thank the faculty and staff of the Department of Dental Biomaterials for all their help. My appreciation goes to Dr. Karl Söderholm and Dr. Chiayi Shen for their support and friendship. They always had time for me

regardless of their busy schedules. Very special thanks go to Mr. Robert Ben Lee. There does not exist a more friendly and helpful person on this planet. Ben is as good a person as I know. I doubt that I could have completed my research without his assistance.

To my fellow graduate students, especially Ananth Naman, I want to say thanks for their help and camaraderie. I hope all of them fulfill their potential and achieve the success that they deserve.

Finally, I would be remiss if I did not thank the most significant people in my life, my parents and my wife Maria. To my parents I will simply say thanks. Words cannot easily convey the admiration that I have for them. I will never be able to repay them for the love, patience and encouragement that they have given me during my life. I am truly lucky to have them. To my wife Maria I will also say thanks, although that seems woefully insufficient. Her generosity, understanding, support and infinite patience make my life a joy to live. It would be hollow without her.

TABLE OF CONTENTS

	<u>page</u>
ACKNOWLEDGMENTS.....	ii
ABSTRACT.....	vii
 CHAPTERS	
1 INTRODUCTION.....	1
2 FUNDAMENTAL PRINCIPLES AND THEORIES OF GLASS- CERAMIC MECHANICAL BEHAVIOR.....	3
2.1 Glass-Ceramics.....	3
2.1.1 Strength of Glass-Ceramics and Glass-Matrix Composites.....	5
2.1.2 Toughness of Glass-Ceramic and Glass-Matrix Composites.....	14
2.2 Microcracking Associated With Thermomechanical Stress.....	26
2.2.1 Thermomechanical Stresses in Brittle Composites.....	28
2.2.2 Spontaneous Microcracking Near Second Phase Inclusions.....	29
2.3 Fractal Geometry.....	33
2.3.1 Definition of Fractal Geometry.....	34
2.3.2 Fractal Dimension.....	35
2.3.3 Fractal Analysis of Fracture Surfaces.....	37
3 MATERIALS AND EXPERIMENTAL METHODS.....	43
3.1 Materials Preparation.....	43
3.1.1 Glass Composition.....	43
3.1.2 Glass Melting and Specimen Preparation.....	43
3.1.3 Crystallization Heat Treatment.....	45
3.2 Material Property Determination.....	46
3.2.1 Thermal Expansion Coefficient.....	46
3.2.2 Density.....	48
3.2.3 Poisson's Ratio and Elastic Modulus.....	49
3.3 Fracture Toughness Determination.....	50
3.3.1 Quantitative Fractography Method.....	50
3.3.2 Controlled-Flaw Strength Method.....	58
3.4 Finite Element Analysis.....	61
3.5 Microcrack Density Determination.....	62

3.6	Fractal Analysis.....	66
3.6.1	Slit Island Technique.....	66
3.6.2	Atomic Force Microscopy Box Counting Technique.....	73
4	RESULTS.....	75
4.1	Microstructure.....	75
4.2	Physical Properties.....	75
4.2.1	Glass Transition Temperature.....	75
4.2.2	Thermal Expansion Coefficient.....	95
4.2.3	Density.....	95
4.2.4	Poisson's Ratio.....	100
4.3	Fracture Toughness.....	100
4.3.1	Fracture Toughness Determined by Quantitative Fractography.....	100
4.3.2	Fracture Toughness Determined by the Controlled-Flaw Flexure Strength Method.....	109
4.4	Finite Element Stress Analysis.....	113
4.5	Microcrack Density.....	115
4.6	Fractal Dimension.....	120
4.6.1	Fractal Dimension Determined by the Slit Island Technique.....	120
4.6.2	Fractal Dimension Determined by the Atomic Force Microscopy Box Counting Technique.....	120
5	DISCUSSION.....	126
5.1	Microstructure.....	126
5.2	Physical Properties.....	128
5.2.1	Glass Transition Temperature.....	128
5.2.2	Thermal Expansion of Lithia Disilicate Glass-Ceramics...	130
5.2.3	Density of Lithia Disilicate Glass-Ceramics.....	132
5.2.4	Elastic Modulus of Lithia Disilicate Glass-Ceramics.....	134
5.3	Fracture Toughness.....	140
5.3.1	Fracture Toughness of Lithia Disilicate Glass-Ceramics..	140
5.3.2	Effect of Microcracking on the Mechanical Properties of Lithia Disilicate Glass-Ceramics.....	148
5.4	Spontaneous Microcracking.....	156
5.5	Fractal Analysis.....	166
5.5.1	Fractal Analysis of Lithia Disilicate Glass-Ceramics.....	166
5.5.2	Fractal Analysis of Crystal and Glass Phases in Lithia Disilicate Glass-Ceramics.....	175
6	CONCLUSIONS.....	183

APPENDICES

A	FINITE ELEMENT ANALYSIS CODE FOR DETERMINATION OF THERMAL MISMATCH STRESSES ADJACENT TO A SPHERICAL CRYSTAL IN A GLASS MATRIX.....	187
B	FINITE ELEMENT ANALYSIS CODE FOR DETERMINATION OF THERMAL MISMATCH STRESSES ADJACENT TO A ELLIPTICAL CRYSTAL IN A GLASS MATRIX.....	189
C	FINITE ELEMENT ANALYSIS CODE FOR DETERMINATION OF THERMAL MISMATCH STRESSES ADJACENT TO TWO SPHERICAL CRYSTALS IN A GLASS MATRIX.....	191
REFERENCES.....		194
BIOGRAPHICAL SKETCH.....		205

Abstract of Dissertation Presented to the Graduate School of the
University of Florida in Partial Fulfillment of the Requirements for the
Degree of Doctor of Philosophy

CHARACTERIZATION OF MECHANICAL BEHAVIOR BASED ON
MICROSTRUCTURAL PHENOMENA IN $\text{Li}_2\text{O} \cdot 2\text{SiO}_2$ GLASS-CERAMICS

By

Jeffrey Yates Thompson

May, 1995

Chairman: Larry L. Hench

Cochairman: Kenneth J. Anusavice

Major Department: Materials Science and Engineering

The mechanical behavior of lithia disilicate glass-ceramics was characterized in terms of microstructural phenomena. The specific objectives of this study were to characterize the effect of crystal volume fraction and crystal size on the fracture toughness and fracture surface fractal dimensional increment of lithia disilicate glass-ceramics. Lithia disilicate was chosen as a model system because there are no compositional variations between the glass and crystal phases, eliminating the problem of property changes with compositional variation in the glass phase. The fracture toughness and fractal dimensional increment were each found to increase with increasing crystal volume fraction in the absence of spontaneous microcracking that occurs as a result of the thermal mismatch between the glass and crystal phases. It is concluded that optimal mechanical properties can only be obtained for lithia disilicate glass-ceramics with mean crystal sizes below the critical dimension for spontaneous microcracking. The critical crystal size for spontaneous microcracking was shown to decrease with increasing crystal volume fraction.

The fracture toughness increased from $1.01 \pm 0.3 \text{ MPa}\cdot\text{m}^{1/2}$ for lithia disilicate glass to $3.02 \pm 0.04 \text{ MPa}\cdot\text{m}^{1/2}$ for lithia disilicate glass-ceramic with a crystal volume fraction of 0.98 and a mean crystal size of $15 \text{ }\mu\text{m}$. The fractal dimensional increment increased from 0.09 ± 0.01 for lithia disilicate glass to 0.23 ± 0.01 for lithia disilicate glass-ceramics with crystal volume fractions of 0.98 and mean crystal sizes of $15 \text{ }\mu\text{m}$ and $27 \text{ }\mu\text{m}$. The fractal dimensional increment was also shown to be significantly different for the glass and crystal phases for lithia disilicate glass-ceramic fracture surfaces. It is concluded that the relationship between fracture toughness and fractal dimensional increment for lithia disilicate glass-ceramics represents a unique family of materials on the fracture toughness versus fractal dimensional increment plane.

CHAPTER 1 INTRODUCTION

Glass-ceramics offer great promise for applications in areas such as the fabrication of dental prostheses. They offer certain advantages over conventional ceramic materials, including low temperature processing, low processing shrinkage, control and variation of translucency, and the ability to fabricate complex shapes with little difficulty. One of the limitations of glass-ceramic materials is that they generally have low fracture strength and fracture toughness. To optimize the structural performance of these materials, it is first necessary to understand the relationships between the properties of the different phases and the microstructure, and how these relationships affect mechanical behavior.

This study was undertaken as part of an effort to develop novel dental ceramic materials. The overall goal of this study was to characterize microstructure / property relationships in a simple glass-ceramic system, in order to apply the knowledge obtained in the optimization of the mechanical behavior of new dental glass-ceramic materials. A simple binary system was chosen in order to eliminate factors that would complicate the analysis of mechanical behavior. For example, a glass-ceramic system with multiple components, *i.e.*, more than two oxide precursors, will present the problem of an ever-changing glass composition during crystallization. This causes great problems in defining the properties of the glass matrix phase when analyzing behavior. A binary glass system that devitrifies to produce a crystal phase with the same composition is

ideal for use in modeling mechanical behavior, since it eliminates the problem of compositional variation.

The lithia disilicate glass-ceramic system was chosen for this study for the previously mentioned reason and because it is the precursor system for a more complex lithia-alumina-calcia-silicate glass-ceramic system that is being developed for use as a dental restorative material. The similarities in the crystallized microstructures of these two systems give an indication that they will behave in a similar manner mechanically. Therefore it is reasoned that knowledge of the mechanical behavior of the simpler binary lithia disilicate system will translate into knowledge that can be used to optimize the performance of the more complex system.

The specific objectives of this study were to 1) characterize the effect of crystal volume fraction and crystal size on the fracture toughness of lithia disilicate glass and glass-ceramics with crystal volume fractions ranging from 0 to 0.98, 2) determine how the thermal mismatch stresses, developed as a result of the thermal expansion mismatch between lithia disilicate glass and crystalline lithia disilicate, affect the physical and mechanical properties of lithia disilicate glass-ceramics, 3) characterize the relationship between the fracture toughness and the fracture surface fractal dimension of lithia disilicate glass-ceramics to determine the effect of the microstructure on crack propagation, 4) determine the fracture mechanisms that dominate the fracture behavior of lithia disilicate glass-ceramics, and 5) characterize the microstructural parameters that control these mechanisms.

CHAPTER 2 FUNDAMENTAL PRINCIPLES AND THEORIES OF GLASS-CERAMIC MECHANICAL BEHAVIOR

2.1 Glass-Ceramics

Glass-ceramics are defined as polycrystalline solids which are prepared by the controlled crystallization of glasses. Generally, a desired shape is produced by forming molten glass, and crystallization is accomplished by subjecting the formed glass to a controlled series of heat treatments. The number of crystals produced, their growth rate, and their final size are determined by the heat treatment schedule used. In most glass-ceramic systems a small amount of residual glass is present even when the crystallization process is taken to completion.

The development of functional glass-ceramics is a relatively recent occurrence, even though it has been known for hundreds of years that almost any glass can be crystallized if it is heated at a suitable temperature for a sufficient period of time (McMillan, 1979; Strnad, 1986). Réaumur, a French chemist, is credited with the earliest documented production of a glass-ceramic. In the early 1700s he crystallized glass bottles by heat-treating them in sand. The opaque porcelain-like objects Réaumur produced had low mechanical strengths and were subject to physical distortion during heat treatment. Although he was able to produce polycrystalline materials, Réaumur was

unable to achieve the controlled crystallization needed to produce usable glass-ceramic articles.

In the 1950s, S.D. Stookey of Corning Glass Works, made a serendipitous discovery that led to the development of the first viable glass-ceramic material (McMillan, 1979). Stookey found that when he heated a photosensitive opacified glass above its normal heat treatment temperature, the glass was converted into an opaque polycrystalline material, with mechanical properties far superior to those of the parent glass. The glass-ceramic produced was free of physical distortion and displayed only minor dimensional changes. Stookey attributed this controlled crystallization to the presence of small metallic crystals within the glass. The metallic crystals acted as nucleation sites for the formation of large crystallites. The use of nucleating agents, such as TiO_2 , P_2O_5 , or Pt, is now quite common in the production of commercial glass-ceramics, although the ultimate microstructure is controlled also by the temperature and time of the heat treatment process.

Currently, glass-ceramics are used in commercial applications ranging from cookware and missile nose cones to dental restorations (Grossman, 1982; Beall and Duke, 1983). As a group of materials, glass-ceramics offer certain advantages over conventional polycrystalline ceramics, including low temperature processing, low processing shrinkage, control and variation of translucency, and ability to fabricate complex shapes with little difficulty. One of the limitations of many glass-ceramic materials is that they possess low fracture strength and fracture toughness (0.5 to 3.0 $\text{MPa}\cdot\text{m}^{1/2}$). The strength and toughness of glass-ceramics are controlled by the properties of the crystalline and glass phases, and the microstructure that is produced during heat treatment. A substantial amount of research has focused on understanding and controlling this behavior.

2.1.1 Strength of Glass-Ceramics and Glass-Matrix Composites

Several investigators have used glass-ceramics or glass matrix composites to analyze the effects of inclusions on the mechanical behavior of two-phase brittle materials. The earliest studies were focused on improving the strength of glasses or single phase ceramics. One of the earliest works on this topic was performed by Binns (1962). Binns studied the effect of thermal expansion and elastic modulus mismatch on the mechanical properties of a series of hot pressed glass matrix composites containing up to 40 volume % zircon ($\text{ZrO}_2\text{-SiO}_2$) or alumina powders with different particle sizes. Binns reported that the maximum benefit of the dispersions was obtained when there was a minimum in the thermal expansion mismatch between the two phases. He also noted that the strength was lowered by a difference in the thermal expansion coefficient of the two phases, and that the lowest strength resulted when the coefficient of thermal expansion of the glass matrix phase was greater than the thermal expansion of the crystal phase.

Binns concluded from his experimental results that multiphase composites should contain phases with matched coefficients of thermal expansion for maximum increases in strength with volume fraction. Binns also concluded that the increase in strength was independent of the particle size, although he pointed out that finer grains could lead to superior materials because they show a lesser tendency to produce cracks. Binns failed to realize that the greater strain energy produced in the larger grain materials, for a given thermal expansion mismatch, was responsible for the formation of cracks adjacent to individual grains.

In the late 1960s and early 1970s, the experimental and theoretical work in this area focused on three mechanisms for increasing or decreasing the

strength of glass matrix composites containing crystalline dispersions. The three mechanisms were 1) alteration of the inherent flaw size in the matrix material, 2) an increase in the composite elastic modulus by high modulus inclusions, and 3) interaction of a propagating crack with second phase dispersions. Each of these mechanisms has its basis in the Griffith-Irwin equation that relates strength, σ , to both the crack size and the fracture energy:

$$\sigma = \frac{K_{IC}}{Yc^{1/2}} = \frac{1}{Y} \left(\frac{2\gamma E}{c} \right)^{1/2} \quad (2.1)$$

where K_{IC} is the critical stress intensity for mode I loading, Y is a geometrical factor that accounts for flaw shape, location, and loading geometry, γ is the fracture surface energy, E is the elastic modulus, and c is the critical flaw size. These three mechanisms spawned three theories for the effects of dispersions, including porosity, on the strength of glass matrix composites.

The first theory, proposed by Hasselman and Fulrath (1966), is flaw oriented. They hypothesized that hard crystalline dispersions will limit the size of Griffith flaws and strengthen the composite. Based on the decrease of elastic energy with the energy needed to form a fracture surface, Griffith derived an expression for the failure strength, σ_o . For an elliptical flaw in a flat plate, the strength is

$$\sigma_o = \left(\frac{2\gamma E}{\pi a} \right)^{1/2} \quad (2.2)$$

where a is the major axis of the ellipse, *i.e.*, the flaw size. They theorized that the effect of dispersions on the size of flaws distributed statistically throughout the bulk or surface of a glass specimen can be divided into two regions. In region I, the flaw size is less than the average distance between particles. On a statistical basis, the size of the average flaw in this region will be reduced.

Hasselman and Fulrath derived the following expression for the effect of dispersions on the strength, σ , of a glass matrix composite in region I:

$$\sigma = \sigma_0(1 - V_f)^{-1/2} \quad (2.3)$$

where σ_f is the failure strength of the unreinforced glass and V_f is the volume fraction of the dispersed phase.

For higher volume fractions or smaller particle sizes, where the average flaw size is greater than the distance between particles, the flaw size is determined by the mean free path between particles. Hasselman and Fulrath (1966) referred to this region as region II. The mean free path, d , is given as

$$d = \frac{4R(1 - V_f)}{3V_f} \quad (2.4)$$

where R is the uniform radius of the particles. Using Griffith's principles for the macroscopic strength of a brittle solid containing an elliptical flaw and their own mean free path hypothesis, they derived the following expression for the strength of a glass matrix composite in region II:

$$\sigma = \left[\frac{3\gamma EV_f}{\pi R(1 - V_f)} \right]^{1/2} \quad (2.5)$$

Experimentally, they found that strengths of a series of sodium borosilicate glasses containing alumina dispersions, with volume fractions between 0.055 and 0.475, agreed with their theory. The experimental results of Hasselman and Fulrath, displaying regions I and II, are shown in Figure 2.1.

Subsequent studies on glass matrix composites and glass-ceramics (Hasselman and Fulrath, 1967; Bertolotti and Fulrath, 1967; Stett and Fulrath, 1968; Freiman, 1968; Stett and Fulrath, 1970; Nivas and Fulrath, 1970; Miyata and Jinno, 1972; Freiman and Hench, 1972; Sproull and Rindone, 1973)

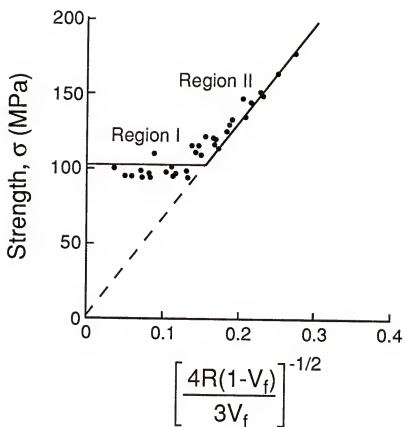


Figure 2.1. Plot, according to Hasselman and Fulrath (1966), of fracture strength versus reciprocal mean free path for glass specimens containing a dispersion of alumina particles.

supported the flaw limitation theory proposed by Hasselman and Fulrath, but each incorporated the concept of micromechanical stress concentrations around inclusions or pores as a contributing factor to the fracture process. These studies concluded that the Griffith flaw limitation mechanism alone was not sufficient to explain the strength behavior observed experimentally for a variety of glass matrix composites. The general consensus of these studies was that internal stresses created by thermal expansion and elastic modulus mismatch would alter the path of fracture and cause the strength behavior to deviate from that predicted by the Hasselman and Fulrath model. The major objection to this theory is that it makes no allowance for changes in the fracture energy even though there is considerable evidence that it is changed by the presence of dispersions.

The second theory, proposed by Frey and Mackenzie (1967), is based on the assumption that glasses containing brittle dispersions will behave as constant strain systems. They attributed the strength increase that was observed in a series of glass matrix composites, containing either alumina or zirconia, to the enhanced elastic modulus of the composite derived from the high modulus particles. They reasoned that when the modulus of a system is increased by the introduction of a dispersed second phase having a higher modulus, an applied load will produce a lower stress in the glass because of the load sharing in relation to the modulus of the individual components. The modulus of the composite and the relative load sharing of the individual components depends on both the modulus and volume fraction of each component. Frey and Mackenzie observed that the strength of their glass/alumina and glass/zirconia composites increased in direct proportion to the increase in the composite modulus.

Frey and Mackenzie's theory of strengthening can be clearly explained using Hooke's law. Consider the load sharing that occurs in a low modulus glass matrix containing particles of a higher modulus second phase. If an applied load is shared by the components in proportion to their elastic moduli, the strain, ϵ , in all components will be the same, *i.e.*,

$$\epsilon_p = \epsilon_g = \epsilon_T \quad (2.6)$$

where the subscripts p, g and T refer to the dispersed phase, the glass matrix and the total system, respectively. Using Hooke's law, equation (2.6) can be rewritten as

$$\frac{\sigma_p}{E_p} = \frac{\sigma_g}{E_g} = \frac{\sigma_T}{E_T} \quad (2.7)$$

and, by rearrangement, we get

$$\sigma_{fT} = \left(\frac{E_T}{E_g} \right) \sigma_{fg} \quad (2.8)$$

where the subscript f refers to the conditions at fracture. In this system, the average applied stress is less than the stress on the high modulus particles and greater than the stress on the glass matrix. Since the strain and stress are constant for the glass, given a defined flaw size, it follows from equation (2.8) that as E_T is increased with the volume fraction of the second phase, the failure stress, σ_{fT} will increase.

Freiman *et al.* (1974), Borom *et al.* (1975) and Borom (1977) reported experimental results for glass matrix composites or glass-ceramics that showed a direct increase in strength with composite elastic moduli. However, these investigators stated that the observed increase in strength could not be completely explained by the concept of stress reduction attributed to the

presence of high modulus particles. The results of these studies imply that the strength of brittle matrix composites is determined by a combination of elastic modulus enhancement and the resultant stress distribution within the composite created from the effects of the elastic modulus and thermal expansion mismatch between the phases.

The third theory, proposed by Lange (1970 and 1971) elaborated by Evans (1972), and supported by the studies of Hing and McMillan (1973) and Nadeau and Bennett (1978), attributes the strengthening of some glass and ceramic composites to the crack growth resistance resulting from direct interaction between the crack and second phase particles. Lange (1970) suggested that the fracture energy of a brittle material should depend on the spacing between particles within the material. He based this theory on observations that the length of a crack front increases when it interacts with a second phase particle within a brittle matrix (Figure 2.2). Using the concept that the crack front has a line energy, *i.e.*, energy per unit length of crack front, Lange proposed that an increase in crack front length should require energy and should therefore increase the energy required to initiate crack propagation. Based on the Griffith-Irwin theory, an increase in fracture energy, γ , should increase the strength of a material.

Lange's model is based on the assumption that the crack front is pinned at second phase inclusions and bows out between them, thus increasing its total length before it breaks away from the pinning positions. He determined that the fractional increase in crack front length per unit crack extension depends on the distance between pinning positions and the curvature of the crack front between these positions. Assuming that the crack front has a line energy, Lange derived the following expression for the fracture energy required to initiate fracture in a brittle matrix composite:

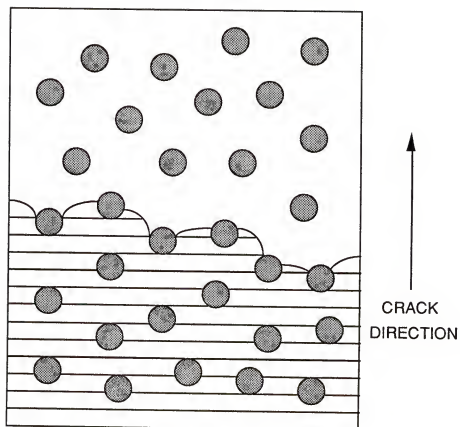


Figure 2.2. Schematic illustration of the crack bowing mechanism proposed by Lange (1970). Propagating cracks are pinned at adjacent inclusions and bow out between them until increased local stress intensity enables the crack to break away from the pinning positions.

$$\gamma = \gamma_0 + \frac{T}{d} \quad (2.9)$$

where γ_0 is the fracture energy of the matrix material, T is the critical line energy per unit length of the crack front, and d is the distance between pinning positions, *i.e.*, the mean free path as defined by Hasselman and Fulrath (equation 2.4). A similarity between the Hasselman and Fulrath and Lange theories is that both incorporate the mean free path between inclusions into their mathematical models. The critical line energy is defined as

$$T \approx c\gamma_0 \quad (2.10)$$

where c is the crack size in the material.

To test his model, Lange (1971) experimentally determined the fracture energy and strength of a sodium borosilicate glass containing alumina dispersions. The glass was formulated so that the thermal expansion mismatch between the two phases was negligible. This was done so that the measured fracture energies and strengths would be independent of the effects of thermal mismatch stresses. Lange found that the experimental data fit his model fairly accurately when it was modified to account for particle size. Lange modified equation 2.6 by incorporating a dimensionless function $F(D)$, dependent on the inclusion size, D , to give the following expression:

$$\gamma = \gamma_0 + F(D) \frac{T}{d} \quad (2.11)$$

where $0 \leq F(D) \leq 1$. Although Lange found reasonably good agreement between his model and experimental data, the model has limitations. Lange ignored the effects of elastic modulus and thermal residual stress on the strength of brittle matrix composite materials. Lange's model does not account for these variables. This may represent an important deficiency since the

majority of glass matrix composites, including most glass-ceramics, display elastic and/or thermal expansion mismatch between phases.

These studies emphasize the importance of internal stresses on the strength of brittle matrix composites containing brittle inclusions. The internal stresses produced by elastic modulus and thermal expansion mismatch between the two phases are critical in determining the mechanisms that control the fracture process and also in determining which mechanism, if any, is dominant.

2.1.2 Toughness of Glass-Ceramic and Glass Matrix Composites

Research on the strength behavior of glass-ceramics and glass matrix composites has gradually shifted to the toughness behavior of these materials. Toughness is a bulk property of the material, while strength is a property that is controlled by the flaw population of a material specimen. Fracture toughness is defined as the resistance of a material to the propagation of a flaw under an applied stress. Toughness is affected by localized stress fields around second phase particles in glass-ceramics or glass matrix composites. Fracture-controlling mechanisms that may be dominant in glass-ceramics include microcracking, crack deflection/interaction, crack bridging and morphological interactions (Mecholsky, 1982; Clarke and Faber, 1987). Another toughening mechanism, that will not be discussed here, is stress-induced phase-transformation, which is primarily important in glass-ceramic systems where metastable zirconia particles are present (Fagherazzi *et al.*, 1980). The toughening mechanisms applicable to glass-ceramics are identical to those that have been observed in other ceramic materials.

The introduction of microcracks is known to affect the fracture toughness of polycrystalline materials. Several studies have implied that microcracking can enhance toughness (Evans, 1978; Evans and Faber, 1981; Green, 1983; Buresch *et al.*, 1983; Miyata *et al.*, 1983; Evans and Faber, 1984; Evans and Fu, 1985; Hutchinson, 1987; Barsoum and Zhou, 1988; Charalambides and McMeeking, 1988; Dolgopolsky *et al.*, 1989). Microcracks ahead of and around the primary direction of crack movement can act as an energy dissipative mechanism similar to a plastically deforming region in ductile materials (Figure 2.3). The increased fracture surface area and subsequent reduction in the effective stress at the crack tip lead to increased resistance to propagation of the primary crack. Toughening will generally increase with increased microcracking until a point is reached where the density of microcracks is so great that crack propagation is enhanced by an increase in fracture surface area, *i.e.*, the material becomes less tough. Therefore, any increase in toughness should pass through a maximum that is controlled by microcracking. Microcracking is controlled by factors such as crystallite or grain size, thermal expansion mismatch and/or anisotropy, and elastic mismatch and/or anisotropy.

Evans (1978) and Evans and Faber (1981 and 1984) proposed that microcrack toughening is caused not only by a process zone of microcracks at the crack tip, but also by the residual energy density in the microcracked process zone wake (Figure 2.4). The residual energy density is derived primarily from the localized material dilatation that accompanies microcracking. This theory is supported by the work of Knehans and Steinbrech (1982), who demonstrated that removal of the microcrack wake in alumina samples reduced the toughness of the material. The concept of residual energy density is similar to the theories associated with crack bridging.

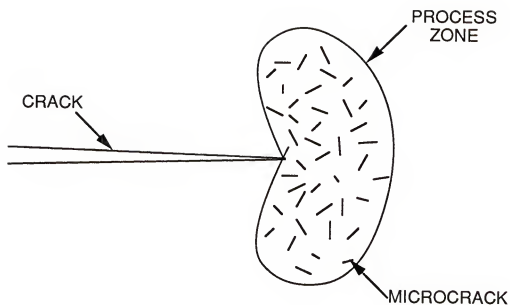


Figure 2.3. Schematic illustration of a microcrack process zone in the vicinity of a crack tip. The localized decrease in elastic modulus, E , associated with the production of microcracks shields the crack tip from applied stresses.

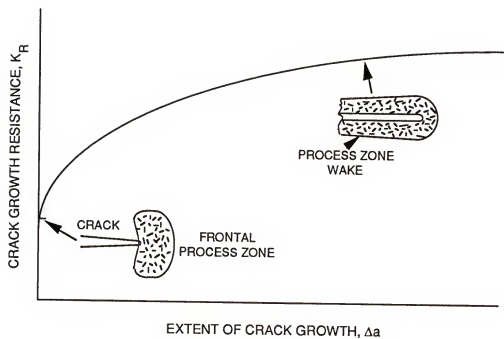


Figure 2.4. Schematic illustration of the R-curve behavior of a brittle material subject to microcrack toughening. Toughening is due to the residual energy density in the microcracked process zone wake.

Evans and Faber (1984) also stated that particle size and particle size distribution are the most important variables in obtaining microcrack toughening. They hypothesized that there is a critical particle size for a given material that yields the maximum toughening benefit derived from microcrack formation (Figure 2.5). The magnitude of this critical particle size is dependent on several material variables. These include: 1) differences in the elastic moduli and/or coefficient of thermal expansion of the matrix and particulate phases, 2) elastic modulus and/or thermal expansion anisotropy of the particulate phase, and 3) the particle shape.

Freiman (1968), Freiman and Hench (1972), and Palmer and Hench (1984) observed microcracking in the lithia disilicate glass-ceramic system. These studies attributed the microcracking to a volume change during crystallization or a difference in the coefficients of thermal expansion of the glass matrix and crystal phase. Mecholsky (1982) attributes the toughness increase corresponding to crystallization in the lithia-disilicate system to microcracking. Mecholsky (1982 and 1983) has also suggested that a major portion of the toughening observed in a zinc-silicate glass-ceramic is associated with microcracking. He described a fracture toughness to grain size relationship that appears similar to the conclusions of Evans and Faber (1981 and 1984). At present, no theoretical model exists to quantitatively explain the toughening benefit derived from microcracking in glass-ceramic materials. It should also be pointed out that although microcrack toughening is a well accepted theory, only Gu *et al.* (1992) have shown clear experimental evidence of microcrack formation at or near the tip of a propagating crack.

Multiphase materials can also show increased toughness because of crack deflection or interaction (Green and Nicholson, 1978; Nadeau and Bennett, 1978; Swearingen *et al.*, 1978; Nadeau and Dickson, 1980; Faber *et*

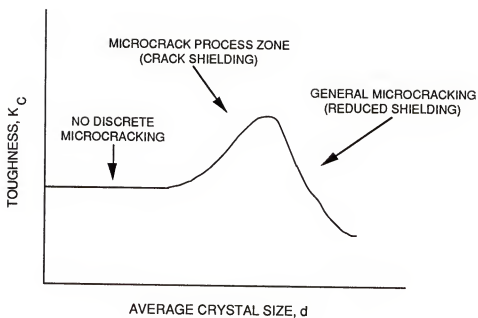


Figure 2.5. Schematic of particle size effect on the toughness of a microcracking brittle material. There is an optimal particle size that will produce the maximum toughness.

al., 1983; Faber and Evans, 1983a and 1983b). The presence of second phase particles located near the tip of a propagating crack can reduce the stress intensity by causing perturbations in the crack front. Crack deflection increases toughness by producing a nonplanar crack which is subject to a local stress intensity lower than that along the planar crack path. The development of a more tortuous path requires more energy for propagation of the primary crack, resulting in increased material toughness. Deflection of the primary crack is caused by residual stress fields around the particles along the path of propagation. Specifically, second phase particles with coefficients of thermal expansion or elastic moduli higher than those of the matrix phase will produce tangential compressive stresses within the matrix adjacent to the particle/matrix interface that will divert the crack around the particle. Similarly, second phase particles with lower coefficients of thermal expansion or elastic moduli than the matrix phase will produce tangential tensile stresses at the particle/matrix interface causing the crack to deflect toward the particle (Figure 2.6).

Crack interaction or crack bowing originates when resistant second phase particles are located in the path of the propagating crack. It has been suggested that the crack front bows between the particles, causing a decrease in the stress intensity along the bowed portion of the crack front. The crack will continue to bow until the fracture toughness of the second phase particles is reached, at which time crack propagation will continue. The fracture toughness and volume fraction of the second phase control the extent of crack bowing and therefore the level of composite toughening. This mechanism, proposed by Lange (1970 and 1971), was explained in greater detail in the previous section on strengthening of glass matrix composites (Figure 2.2).

Nadeau and Dickson (1980) concluded that toughening observed in a series of glass matrix/glass particulate materials was associated with three

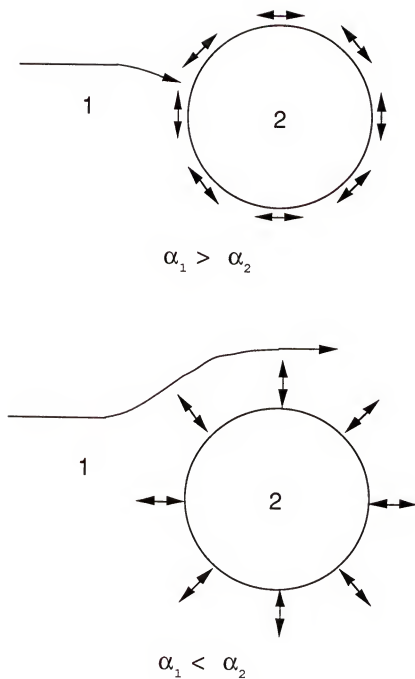


Figure 2.6. Schematic illustration of the effect of thermal expansion mismatch between the matrix phase (1) and the particulate phase (2) on the path of a propagating crack.

different mechanisms. The mechanisms they described were 1) prestressing of the dispersed phase, whereby the particles are made relatively impenetrable by compressive stresses, 2) crack deflection caused by the stress field of the particle, and 3) crack bowing between particles. Mecholsky (1983) concluded that small toughness increases (less than 10%) observed in various glass-ceramic systems can be attributed to elastic mismatch/anisotropy.

A study by Wu *et al.* (1978) analyzed crack propagation in several ceramic materials. They described three modes of crack propagation: 1) crack twisting, 2) crack wandering, and 3) crack branching. Crack propagation behavior was dependent on the microstructural features of each material. Faber and Evans (1983a) developed a model to determine the increase in toughening caused solely by crack deflection processes (Figure 2.7). They suggest that the sign and magnitude of the local residual stress field, caused by thermal expansion or elastic modulus mismatch between the particle and matrix, have no significant influence on the magnitude of crack interaction toughening. In an accompanying study, Faber and Evans (1983b) found that the fracture toughness in a series of lithia-alumina-silicate glass-ceramics was invariant with crystal size. The toughness values were in good agreement with the values predicted by their model. However, analysis of the effect of tensile versus compressive residual stresses on the degree of attainable toughening was not undertaken. In another study, Morena *et al.* (1983) explained that some of the toughening exhibited by a cordierite glass-ceramic was caused by crack pinning, *i.e.*, crack bowing. Although previous studies have shown the existence of crack deflection/interaction toughening mechanisms in brittle matrix/particulate composites, this behavior is not understood fully at present.

Bridging or frictional interlocking of the primary crack by grains or second phase particles can also increase the fracture toughness of polycrystalline

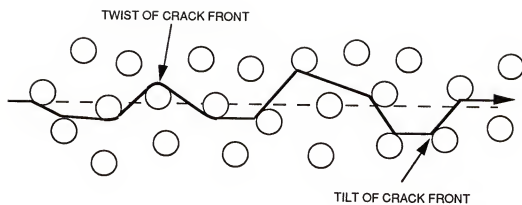


Figure 2.7. Schematic illustration of a crack deflection toughening process in a brittle matrix containing a dispersion of brittle particles.

materials (Figure 2.8). If the primary crack is bridged by crystallites or other inclusions, then additional stress will be necessary to overcome this crack tip shielding and facilitate further propagation, thereby increasing the material toughness. Toughening should increase as the number of crack bridges increases. It is likely that there is a maximum length, related to the microstructure, of this "bridging zone" that will affect the material toughness. This optimal length should vary depending on the morphology of the polycrystalline material.

Swanson *et al.* (1987) attributed the R-curve behavior of a coarse-grained alumina on the presence of grain-localized bridging across the primary crack interface. For the coarse-grained alumina employed in their study, the mean bridge spacing was approximately 2 to 3 grain diameters, and the zone of interfacial bridging behind the crack tip was approximately 100 grains in length. They suggest that for a given material there will be a steady-state activity zone of crack bridging, of a characteristic length, that translates with the growing crack. They further suggest that this toughening mechanism might be active in glass-ceramic materials, but they have not verified this hypothesis through experimentation.

Morphological interaction is another mechanism that can lead to increased fracture toughness in polycrystalline materials. Prior investigations (Freiman *et al.*, 1974; Mecholsky, 1983; Faber and Evans, 1983b) have shown that toughening of glass-ceramic and ceramic materials by the formation of elongated grains as opposed to spherulitic grains. If a propagating crack is forced to move around second phase particles, then longer particles, particles with higher aspect ratios, should increase the tortuosity of the fracture path (Figure 2.9), thereby increasing the overall fracture toughness of the material. The development of highly complex morphologies instead of simple spherulitic

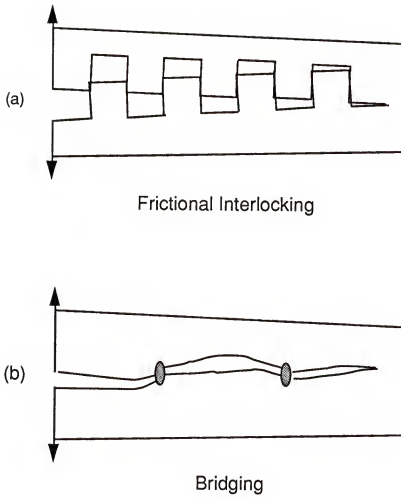


Figure 2.8. Schematic illustration of crack tip shielding by (a) frictional interlocking and (b) crack bridging.

structures should increase the fracture toughness of suitable polycrystalline materials.

Mecholsky and Freiman (1977) analyzed the effect of crystal morphology on the fracture toughness in a baria-silica ($3\text{BaO} \cdot 5\text{SiO}_2$) glass-ceramic system. Because of the very small differences in thermal expansion and elastic moduli between the glass and crystal phases (Freiman *et al.*, 1974), the effect of crystal morphology could be effectively analyzed. Mecholsky and Freiman observed an increase of nearly 100% in the fracture toughness of baria-silica glass-ceramics with tabular crystals compared with those containing spherulitic crystals. It is likely that the tabular morphology produces a more tortuous fracture path which accounts for the increased toughness. Similar enhancement in the fracture toughness of mica-containing glass-ceramics with tabular crystals could be explained by this toughening mechanism (Mecholsky, 1983).

With the exception of morphology related toughening, each of the mechanisms described here can be affected significantly by the presence of internal thermomechanical stresses.

2.2 Microcracking Associated with Thermomechanical Stress

Residual stresses can be produced in glass-ceramics or multiphase ceramic materials as a result of thermal expansion mismatch between the phases. As a material is cooled from the fabrication temperature, the mismatch in thermal expansion coefficients results in incompatible thermal strains that are associated with thermomechanical stresses. In some cases, the magnitude of these stresses is large enough to produce microcracks in either or both of the phases. Previous studies have shown that the extent of this spontaneous

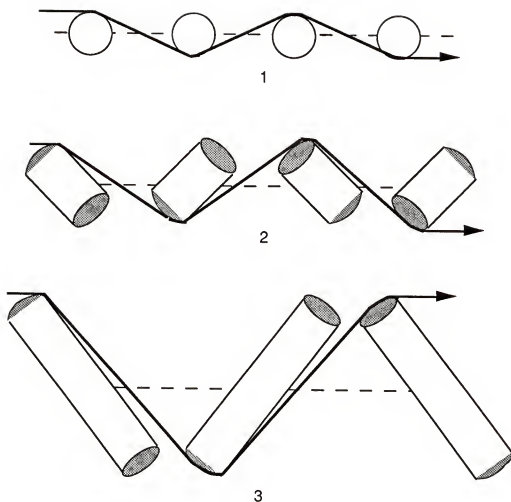


Figure 2.9. Schematic illustration of the effect of particle morphology on the path taken by crack forced to propagate around a dispersed phase. Elongated particles with high aspect ratios (3) will produce a more "tortuous" path than spherical particles (1), and can produce greater incremental toughening.

microcracking is influenced directly by the particle size of the secondary phase. Generally, the incidence of cracking increases when the particle size exceeds a critical value. Spontaneous microcracking can have a significant effect on the mechanical, optical, and thermal properties of a material. Therefore, it is of practical interest to develop an understanding of this phenomenon that can lead to methods for controlling its effects.

2.2.1 Thermomechanical Stresses in Brittle Composites

The localized stresses, produced by an expansion mismatch adjacent to particles in a brittle matrix can be calculated using elasticity theory. Following the techniques of Goodier (1933) and Eshelby (1957), Selsing (1961) derived expressions for the radial and tangential stresses in the matrix of an elastic material containing a spherical particle. The stresses in the matrix, for an isotropic linear elastic continuum, are given by

$$\sigma_{rr} = \sigma_T \left(\frac{R}{r} \right)^3 \quad (2.12a)$$

and

$$\sigma_{\theta\theta} = -\frac{\sigma_T}{2} \left(\frac{R}{r} \right)^3 \quad (2.12b)$$

where σ_{rr} is the radial stress, $\sigma_{\theta\theta}$ is the tangential stress, σ_T is the hydrostatic thermal stress, R is the particle radius and r is the distance from the center of the inclusion. The hydrostatic thermal stress is given by

$$\sigma_T = \frac{(\alpha_p - \alpha_m)(T_f - T)}{(1 + \nu_m)/2E_m + (1 - 2\nu_p)/E_p} \quad (2.13)$$

where α_m and α_p are the coefficients of thermal expansion of the matrix and particle, ν_m and ν_p are the Poisson's ratios of the matrix and particle, E_m and E_p are the elastic moduli of the matrix and particle, respectively, T_f is the fabrication temperature, and T is the ambient temperature. The stresses decrease with the third power of the distance from the particle/matrix interface. The mathematical solutions for the stresses adjacent to an elliptical particle, or for the case where the stress fields of two or more particles overlap, are much more rigorous and will not be detailed here. These complex solutions are more easily solved using finite element computer simulations.

2.2.2 Spontaneous Microcracking Near Second Phase Inclusions

Binns (1962) is generally credited with publishing the first evidence showing that microcracking will occur in glass matrix (m) composites containing particles (p) with different thermal expansion coefficients. He noted that the particle size greatly influenced the development of microcracks during fabrication. Binns found that for $\Delta\alpha = 0$, no microcracking was observed. For specimens in which $\alpha_m \neq \alpha_p$, he observed a large degree of microcracking for large particle sizes, but no microcracking for small particle sizes. Similar observations have been made by several investigators, including Hasselman and Fulrath (1966), Davidge and Green (1968), Utsumi and Sakka (1970), and Freiman and Hench (1972).

Two approaches have been used to estimate the critical particle diameter that will induce spontaneous microcracking in a brittle matrix/brittle particulate composite. Davidge and Green (1968) used an energy balance criterion to estimate the critical particle diameter. They reasoned that when the residual elastic strain energy, U_{SE} , created by thermal mismatch stress, exceeds the

energy required to create fracture surface area, U_s , microcracking can occur. Since these energy terms depend on volume and surface area, a microfracture criterion is obtained in terms of critical particle diameter. This energy balance approach represents a minimum condition for crack formation.

In terms of Davidge and Green's energy balance approach, spontaneous microcracking will occur when

$$U_{SE}f(\phi_f) \geq U_s \quad (2.14)$$

where ϕ_f is the final normalized crack length ($\phi_f = a/R$), a is one-half the major axis of the microcrack produced, R is the particle radius, and $f(\phi_f)$ is the fraction of the residual strain energy required for crack formation. They considered the condition for microcrack formation at the interface between the particle and matrix. For a spherical particle under hydrostatic tension, the residual elastic strain energy is given by

$$U_{SE} = 2\pi k \sigma_T^2 R^3 \quad (2.15)$$

where σ_T is the thermal stress defined in equation (2.13) and k is a constant defined as

$$k = \frac{(1 + \nu_m)}{2E_m} + \frac{(1 - 2\nu_p)}{E_p} \quad (2.16)$$

For the geometry under consideration, equation (2.14) can be rewritten as

$$2\pi k \sigma_T^2 R^3 f(\phi_f) \geq 4\pi R^2 \gamma (1 - \cos \phi_f) \quad (2.17)$$

where γ is the energy required to form a unit area of fracture surface. The failure criterion in terms of a critical particle radius, R_c , is then given by

$$R_c \geq \frac{2\gamma(1-\cos\phi_f)}{k\sigma_T^2 f(\phi_f)} \quad (2.18)$$

Davidge and Green made the arbitrary assumption that $\phi_f \approx \pi/2$ and $f(\phi_f) \approx 0.5$. Using these assumptions, the critical particle size for spontaneous microcracking for the given geometric conditions is estimated as

$$R_c \geq \frac{4\gamma}{k\sigma_T^2} \quad (2.19)$$

Similar expressions for the critical particle size, based on an energetics approach, have been derived by Lange (1974) and Ito *et al.* (1981). A summary of these derivations has been presented by Green (1983). Rice and Pohanka (1979) and Miyata *et al.* (1983) assessed the accuracy of Davidge and Green's energy balance model using experimental techniques. They reported reasonably good agreement between their experimental results and the model.

An alternative method for determining the critical particle size that will produce spontaneous microcracking is based on a stress intensity approach. This approach has been proposed by Evans (1974), and has been described further by Lange (1978). For this approach, the condition for crack extension is given by

$$K_{Rp} \geq K_{ICm} \quad (2.20)$$

where K_{Rp} is the stress intensity associated with the thermal residual stress and K_{ICm} is the fracture toughness of the matrix phase. Evans (1974) examined the criteria for radial crack extension from spherical particle within a stress field associated with a thermal expansion mismatch when $\alpha_m > \alpha_p$, *i.e.*, a particle under hydrostatic compression. The stress intensity factor for this condition is

$$K_{Rp} = \frac{\sigma_{\theta\theta\max}}{2} D^{1/2} (\pi\phi_f)^{1/2} \beta \quad (2.21)$$

where $\sigma_{\theta\theta\max}$ is the maximum tangential stress, D is the inclusion diameter, ϕ_f is the normalized flaw size and β is defined as

$$\beta = \left[1 - \frac{18}{4} \phi_f + 15\phi_f^2 - \frac{175}{4} \phi_f^3 + \dots \right] \quad (2.22)$$

The minimum condition for crack propagation occurs when $K_{Rp} = K_{ICm}$. From equation (2.21), this condition is given by

$$K_{Rp} = K_{ICm} = \frac{\sigma_{\theta\theta\max}}{2} D^{1/2} (\pi\phi_f)^{1/2} \beta \quad (2.23)$$

or , after rearranging,

$$\sigma_{\theta\theta\max}^2 D^{1/2} \geq 30 K_{ICm}^2 \quad (2.24)$$

This expression defines the critical size of a spherical particle below which spontaneous crack extension will not occur. Similar expressions, based on a stress intensity approach, have been developed by Green (1981) to account for applied stress as well as thermal residual stress.

Both the energetic and stress intensity solutions to crack extension agree with experimental observation in qualitatively predicting a critical particle size below which crack formation and extension will not occur (Lange, 1978). However, both approaches are limited in their ability to quantitatively predict the critical particle size. The stress intensity approach is inherently limited by the requirement that the forces, that give rise to the stress field, are unaffected by the crack extension. The energetics approach is limited by the assumptions associated with the function $f(\phi_f)$. Although both models can be refined for better quantitative accuracy, both are valuable in understanding and predicting

the effect of grain size on mechanical behavior in brittle matrix composites, such as glass-ceramics.

The effect of residual stress-induced microcracking, *i.e.*, spontaneous microcracking, on the fracture toughness of brittle materials has been analyzed by several investigators (Rose, 1986; Ortiz, 1988; Sung and Nicholson, 1990a and 1990b; Curtin and Futamura, 1990; Cai *et al.*, 1991; Han *et al.*, 1992). These analytical and experimental studies indicate that this type of microcracking will in most cases lead to a deterioration in the resistance of a material to fracture. Ortiz (1988) stated that any toughness enhancement derived from shielding, *i.e.*, lessening the effect of applied loads by local reduction of the effective modulus of the material, is counterbalanced by the reduction of toughness in the microcracked material. Han *et al.* (1992), in experimental studies on the fracture resistance of alumina reinforced with SiC whiskers, found that some toughness gains can be achieved despite the presence of damage involving microcracking created by the coalescence of intergranular/interfacial cavities in the composite. However, Han *et al.* also state that significant increases in microcrack density lead to decreases in the material toughness. At present, the effects of spontaneous microcracking on the toughness of brittle matrix composites are not completely understood.

2.3 Fractal Geometry

In recent years, quantitative analysis of fracture surfaces has become an integral part of the study of mechanical failure of brittle materials. One of the newer techniques used in this endeavor is fractal analysis. Fractal analysis of fracture surfaces provides a quantitative measure of surface roughness which can be correlated with material parameters such as fracture toughness.

2.3.1 Definition of Fractal Geometry

The science of fractal geometry has evolved from the limitations of Euclidean geometry (Takayasu, 1990). Over the last several centuries, mathematicians such as Peano of Italy, Cantor and Hausdorff of Germany, and Besicovitch of Russia developed geometric constructions that opposed the fundamentals of Euclidean geometry (Devaney, 1990). In the 1970s, B. B. Mandelbrot developed a great interest in these non-Euclidean concepts. He showed that many naturally occurring objects or shapes, such as snowflakes, coastlines, and clouds, could be described quantitatively using non-Euclidean mathematics. Mandelbrot introduced the term "fractal" to represent this branch of mathematics. The word fractal is derived from the Latin "fractus" which means broken or fragmented.

Fractal geometry is defined as a non-Euclidean geometry that permits non-integer dimensions, exhibits self-similarity or self-affinity, and is characterized by scale invariance (Mandelbrot, 1982). Self-similarity describes shapes or processes that are statistically equivalent in different locations and are related by a scalar quantity. Self-affinity describes shapes that have a directional scaling dependence, similar to an anisotropic property. Self-affine processes are related by a vector quantity. Scale invariance implies that the geometrical features of an object appear the same at all scales.

The characteristics of fractal geometry are illustrated in the construction of a scaling fractal. Scaling fractals are constructed using a generator shape and a set scheme of replication. For example, a Koch island (Mandelbrot, 1982) can be generated using this technique (Figure 2.10). The box shown in Figure 2.10a has sides of a specified length. The generator shape next to the box is composed of line segments scaled to one-fourth the length of a side of

the box. Each side of the box is replaced by the scaled generator shape (Figure 2.10b). The generator shape is scaled down to the length of each straight line segment in the new object. The scaled generator shape then has line segments equal to one-sixteenth of the original box segment (Figure 2.10c). If this scaling process is continued indefinitely, a fractal object exhibiting self-similarity and scale invariance is produced.

2.3.2 Fractal Dimension

Empirically, non-complex shapes such as a line, a square, or a cube have integer dimensions of 1, 2, and 3, respectively. These shapes are well described by Euclidean geometry, that defines shapes only by integer dimensions. More complex shapes, such as a snowflake, can not be easily described by Euclidean geometry. In fractal geometry, complex shapes are described by non-integer or fractional dimensions. Fractal geometry is characterized by the use of a fractal dimension, that is based on measurement theory.

As an example, consider the measurement of the length of a line. A measuring tool or ruler is required to accomplish this task. A line is shown in Figure 2.11a. The length of the line is measured by covering it with discs of radius R (Figure 2.11b). The length of the line is given by

$$\text{Length} = (\text{number of discs}) * (\text{disc diameter}). \quad (2.25)$$

For a disc diameter of $2R$ in Figure 2.11b, the length of the line is equal to $44R$. If the disc diameter is doubled to $4R$ and the line is measured again, a new line length is computed (Figure 2.11c). For the disc diameter of $4R$, the length of the

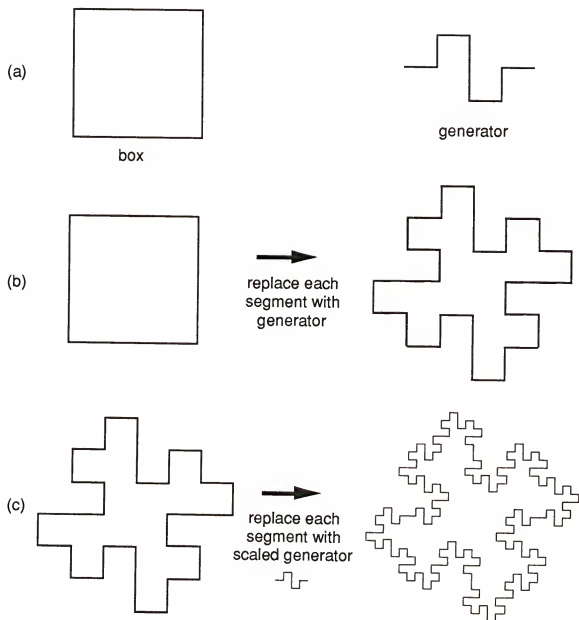


Figure 2.10. Schematic illustration showing one type of construction for a scaling fractal. (a) The generator shape is used to replace each side of the box. (b) The resulting shape after one iteration. (c) The resulting shape after two iterations.

line is equal to $40R$. The tortuous nature of the line gives a length that is scale dependent. As the measuring scale or unit increases, the length decreases.

The measured length of a selected line segment is given by Richardson's equation:

$$L = kS^{1-D} \quad (2.26)$$

where L is the total length of the selected line segment, S is the length of the measuring unit, D is the fractal dimension, and k is a proportionality constant. For a selected line, if D is equal to one, the line is described by Euclidean geometry, and its measured length is not a function of scale. However, if $1 < D < 2$, the line is described by fractal geometry, and the dimension is equal to D . For a fractal object, the length or size is not constant, but the fractal dimension is.

The fractal dimension of a line can be calculated using Richardson's equation. The line is measured using a range of measuring units. A plot of $\log L$ versus $\log S$ will produce a straight line with a slope of $1-D$ (Figure 2.12). The more complex or tortuous the line, the higher the value of the fractal dimension. Hence, the fractal dimension may be regarded as an index of tortuosity.

2.3.3 Fractal Analysis of Fracture Surfaces

Fractal analysis of fracture surfaces is a relatively new field in the science of fractography. The application of fractal geometry to fracture surface analysis developed from the findings of several studies over the last several decades. Poncelet (1958) observed finer mist regions within the mirror region of a glass fracture surface. Abdel-Latif *et al.* (1981) showed that multiple mirror-mist-hackle regions followed the same mathematical relationships as the initial

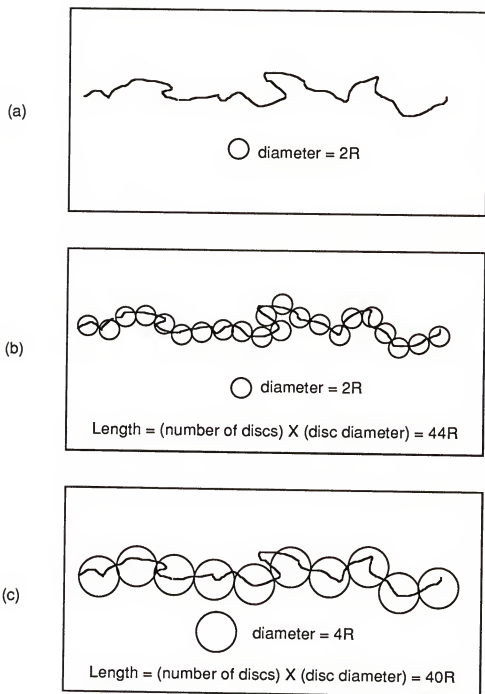


Figure 2.11. Example of the variation in the measured length of a line due to the scale of the measuring unit.

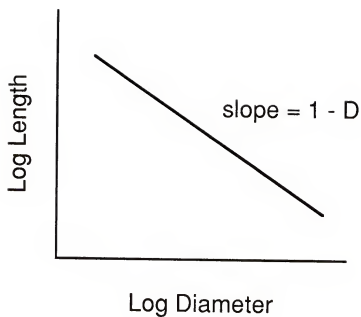


Figure 2.12. Example of a Richardson plot. The fractal dimension, D , is obtained from the slope of the line.

region. Ravi-Chander and Knauss (1984) noted from high speed photographs that the formation of mist and hackle appeared physically similar. These and other findings have lead to concept that the formation of mirror, mist, hackle and crack branching regions on fracture surfaces are self-similar, scale invariant processes. Mandelbrot *et al.* (1984) were the first to note the fractal nature of fracture surfaces. Mecholsky and Passoja (1985) hypothesized that fracture in brittle materials can be defined as a self-similar process, and can therefore be described by fractal geometry. In addition, fractal analysis offers the possibility of relating fracture surface morphology to atomic bonding and structure (Mecholsky *et al.*, 1988).

Mecholsky and Passoja (1985) and Mecholsky *et al.* (1986) determined experimentally that the fractal dimension, D , is related to the fracture toughness, K_{IC} , by the following expression:

$$K_{IC} = K_0 + A(D-1)^{1/2} \quad (2.27)$$

where K_0 is defined as the toughness for smooth planar fracture and A is a constant that represents "families" of materials with microstructural similarities (Mecholsky *et al.*, 1988; Mecholsky *et al.*, 1989). There is no experimental evidence in the literature for planar fracture of primary bonds. Therefore, the value of K_0 is generally assumed to be zero (Thompson *et al.*, 1994). If the value of K_0 is set equal to zero and the term $(D-1)$ is replaced by D^* , equation (2.27) can be rewritten as

$$K_{IC} = A(D^*)^{1/2} \quad (2.28)$$

where D^* is defined as the fractal dimensional increment.

The family parameter, A , identifies a line in the K_{IC} versus D^* plane. Within a specific "family," fracture toughness increases as the fractal dimension

increases. The results of several previous studies on brittle materials, including Mecholsky *et al.* (1986, 1988, and 1989), Fahmy *et al.* (1991) and Naman (1994) support this concept. Contrary to these findings, Baran *et al.* (1992) concluded that there was no relationship between toughness and the fractal dimension for a series of dental porcelains that they examined, although they reported that fractal dimension decreased with an increase in fracture toughness. Studies attempting to characterize the fracture surface of ductile materials, including those by Mandelbrot *et al.* (1984), Pande *et al.* (1987) and Davidson (1989), have also found no quantifiable relationship between toughness and fractal dimension. Although there is sufficient evidence in the existing literature to suggest that the relationship described in equation (2.28) is valid for brittle materials, there is also evidence that suggests that these same relationships may not be valid for materials that undergo plastic deformation during fracture, *i.e.*, most metals and polymers (Mecholsky, 1991).

According to equation (2.28), A must have the dimensions of fracture toughness, since D^* is a dimensionless parameter. Mecholsky *et al.* (1988) proposed that A is a product of the elastic modulus, E , and a characteristic length, a_0 , such that

$$A = E(a_0)^{1/2} \quad (2.29)$$

Substituting for A , equation (2.28) can be rewritten as

$$K_{IC} = E(a_0 D^*)^{1/2} \quad (2.30)$$

For plane stress conditions, fracture toughness is defined as

$$K_{IC} = \sqrt{EG} = \sqrt{2\gamma E} \quad (2.31)$$

where G is the strain energy release rate and γ is the fracture energy. Combining equations (2.30) and (2.31), the following expression is obtained

$$a_0 = \frac{2\gamma}{ED^*} \quad (2.32)$$

The value of a_0 can be determined from experimentally obtained values of γ , E and D^* . At present, the significance of a_0 is unclear. It has been hypothesized that a_0 is related to the characteristic length of a fractal generator (Mecholsky, 1991). For fracture processes, this suggests that a_0 is related to a characteristic bond length, *i.e.*, the strained bond length before fracture, or the radius of an atomic process zone which is involved with fracture initiation at a crack tip. The concept of a characteristic length potentially provides a method for understanding how fracture surfaces are created at the atomic level. This concept also allows a means for relating macroscopic and microscopic fracture processes to fracture at the atomic level.

CHAPTER 3 MATERIALS AND EXPERIMENTAL METHODS

3.1 Materials Preparation

3.1.1 Glass Composition

The lithia disilicate ($\text{Li}_2\text{O} \cdot 2\text{SiO}_2$) glass used in this study had the composition 33.3 mol % (19.9 wt %) Li_2O - 66.7 mol % (80.1 wt %) SiO_2 . The primary constituents of the glass were 5.0 μm Min-U-Sil silica (SiO_2) and reagent grade lithium carbonate (Li_2CO_3). A 70 lb batch of the glass was obtained from Specialty Glass Company (Oldsmar, FL). The glass was produced by melting the primary powders in a covered fused silica crucible in a conventional gas-fired glass melting furnace at a temperature of 1350°C. After a 24 h homogenization period at 1350°C, the glass melt was wet-fritted in deionized H_2O , milled with alumina grinding media, and sieved to -325 mesh. A chemical analysis of the glass powder was performed by CELS - Laboratory Services (Corning Incorporated, Corning, NY) and is presented in Table 3.1.

3.1.2 Glass Melting and Specimen Preparation

The lithia disilicate glass frit was remelted to produce the required specimen configurations. The glass frit was melted in a 150 mL covered ZGS

Table 3.1
Quantitative Chemical Analysis of $\text{Li}_2\text{O} \cdot 2\text{SiO}_2$ Glass

<u>Compound</u>	<u>Weight %</u>
SiO_2	79.7
Li_2O	19.1
Al_2O_3	0.1 - 0.3
$\text{B}_2\text{O}_3, \text{Na}_2\text{O}$	0.03 - 0.1
$\text{BaO}, \text{CaO}, \text{ZnO}$	0.01 - 0.03
MgO	0.003 - 0.01
$\text{FeO}, \text{Fe}_2\text{O}_3, \text{SrO}$	0.001 - 0.003
$\text{CuO}, \text{MnO}, \text{TiO}_2$	< 0.001
BeO	< 0.0005

platinum crucible (Johnson Matthey, Seabrook, NH) in a refractory furnace (Deltech Model DT-31-RS-OS, Deltech Inc., Denver, CO) heated by electrically resistant molybdenum disilicide heating elements. The glass was melted at 1325°C for a minimum of 24 h to ensure homogenization. Disc specimens were prepared for use in biaxial flexure testing. The discs were cut from lithia disilicate glass rods. The rods, 16 mm in diameter and 60 mm in length, were cast by pouring molten glass into a graphite mold. After casting, the glass rods were immediately placed in an electric muffle furnace (Model F6020, Thermolyne Corporation, Dubuque, IA) at 450°C and furnace cooled to room temperature. Slow cooling prevented the glass rods from cracking. Once cooled, the glass rods were sectioned into discs 2.0 mm thick using a low-speed diamond wheel saw (Model 650, South Bay Technology Inc., San Clemente, CA). After sectioning, the specimen surfaces were finished with 320 grit SiC abrasive to remove rough surface irregularities. Fine polishing of all disc specimens was performed after the crystallization process.

3.1.3 Crystallization Heat Treatment

Crystallization of all glass specimens was carried out using a two step heat treatment. The nucleation temperature was selected by determining the glass transition temperature. The glass transition temperature was determined using differential thermal analysis (DTA) and differential scanning calorimetry (DSC). DTA and DSC analyses were performed on a thermogravimeter/differential thermal analyzer (TG/DSC/DTA Model 320, Seiko Instruments, Tokyo, Japan). Nucleation heat treatment was performed at 470°C, followed by a crystal growth heat treatment at 600°C. All nucleation and crystal growth heat treatments were performed in an electric tube furnace (Model 54577, Lindberg

Corporation, Watertown, WI). The times of both the nucleation step and the crystal growth step were varied to produce a matrix of samples with 16 microstructures. Four nucleation times, 0.25 h, 1.5 h, 4 h and 10 h, were used to yield four groups with distinct nuclei densities. Crystal growth times were then varied within each group to yield crystal volume fractions (V_f) of 0.10, 0.30, 0.70 and 0.98. An additional group nucleated for 100 h with $V_f = 0.98$ was also prepared.

The heat treatment schedules were determined by producing a matrix of samples, that were nucleated at 470°C for the times listed above, and then heat-treated at 600°C for a series of times with 5 min increments. Cross-sections of at least two samples at each condition were then polished, and the crystal volume fraction determined using optical micrographs and quantitative stereology as described by Underwood (1970). The times needed to produce the desired volume fractions were then determined by repeating this procedure at smaller time increments of the same approximate time. A plot of the heat treatments used is presented in Figure 3.1. X-ray diffraction data from crystallized specimens obtained from lithia disilicate glass suggest that lithia disilicate ($\text{Li}_2\text{Si}_2\text{O}_5$) was the only crystal phase present in the glass-ceramic specimens (Parsell, 1993; Naman, 1994).

3.2 Material Properties Determination

3.2.1 Thermal Expansion Coefficient

The coefficient of thermal expansion, α , of glass and crystalline lithia disilicate specimens was calculated from expansion data measured with an automatic recording dilatometer (Model EK2, The Edward Orton Jr. Ceramic

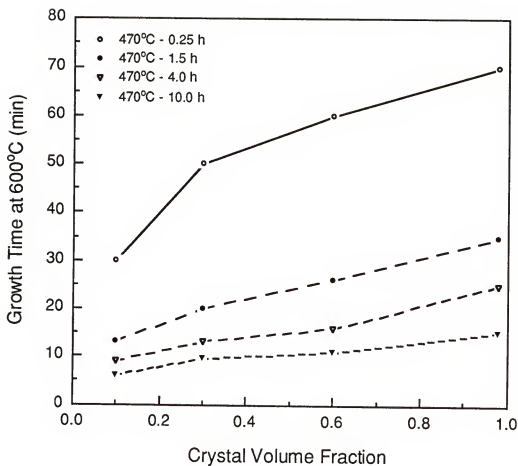


Figure 3.1. Crystal growth times used to produce crystal volume fractions of 0.10, 0.30, 0.70, and 0.98. Each line indicates a different nucleation time.

Foundation, Columbus, OH). Samples used in measuring the coefficients of thermal expansion were prepared by casting glass rods 50 mm in length and 0.5 mm in diameter. Rods with crystal volume fractions of 0.10, 0.30 and 0.98 were prepared for nucleation times of 0.25 h and 10 h. In addition, fully crystalline rods essentially free of microcracks were prepared using a nucleation heat treatment of 100 h at 470°C and a crystal growth heat treatment of 24 h at 600°C. This fully crystalline microstructure was used to approximate the behavior of the spherulitic crystal phase that is formed during crystallization of lithia disilicate. Each rod was ground to a length of 50 ± 0.001 mm prior to thermal expansion testing. Measurements were made for two rods of each microstructure selected. Two measurements were made for each rod to ensure that any residual stresses produced during sample preparation would not influence the test results. The temperature of each sample was increased from 25°C to 450°C at a rate of 4.0°C/min. All measurements were made in air.

3.2.2 Density

The density of specimens was determined from measurements of weight and volume. The density of both monolithic and powder samples was determined for each glass-ceramic microstructure and for glass. Two monolithic disk specimens of each microstructure were cleaned, and then dried for two hours at a temperature of 200°C. The dry weight of each sample was obtained using a precision balance (Model HL 52, Mettler Instruments Corp., Hightstown, NJ). The volume of each specimen was measured using a helium micropycnometer (Model MPY-1, Quantachrome Corp., Syosset, NY). Once the density of the bars was determined, each was ground into powder in a mortar by a pestle. A magnet was run through each powder specimen to ensure that no

metallic particulates were present. The weight and volume of each specimen were then determined using the previously described procedure.

3.2.3 Poisson's Ratio and Elastic Modulus

Poisson's ratio, ν , and elastic modulus, E , of lithia disilicate glass and glass-ceramic specimens were determined using an ultrasonic pulse apparatus (Ultima 5100, Nuson Inc., Boalsburg, PA). The ultrasonic pulse was used to measure the velocity of sound through each specimen. The specimens used in these measurements were 2 mm thick polished disks. Piezoelectric transducers (Ultratran Laboratories Inc., Boalsburg, PA), one pulser and one receiver, were mechanically attached at opposite ends of each specimen to produce a 800 MHz pulse with a pulsewidth of 90 ns. Two types of transducers (Ultratran WC25-10 and Ultratran SWC25-10) were used to generate longitudinal and shear ultrasonic waves. The longitudinal velocity, v_L , and shear wave velocity, v_s , were determined and used to calculate Poisson's ratio and elastic modulus of each specimen. Poisson's ratio is given by the relationship

$$\nu = \frac{1 - 2(v_s/v_L)^2}{2 - 2(v_s/v_L)^2} \quad (3.1)$$

Elastic modulus is given by the relationship

$$E = \frac{\rho v_L^2 (1 + \nu)(1 - 2\nu)}{1 - \nu} \quad (3.2)$$

where ρ is the density.

3.3 Fracture Toughness Determination

Fracture toughness was determined using a quantitative fractography method and a controlled-flaw strength method.

3.3.1 Quantitative Fractography Method

Previous studies (Mecholsky *et al.*, 1976; Mecholsky and Freiman, 1977; Mecholsky *et al.*, 1978) have shown that analysis of the fracture surface features of glass-ceramics can be used to determine values of fracture toughness (K_{IC}) by correlating the size of fracture-initiating flaws with fracture strength. In this study, indented biaxial flexure discs were used to determine fracture toughness by the fractography method. Ten discs were prepared for each of the 17 heat-treatments described previously.

After the two stage heat treatments, that were required to produce the various microstructures, the discs were polished to ensure equivalent surface flaw distributions and to produce parallel surfaces. Each disc was affixed to a stainless steel mounting block with a shellac compound (Kerr Manufacturing Company, Romulus, MI) and ground using a hand lapping fixture (Model 150, South Bay Technology Inc., San Clemente, CA). One side was ground sequentially with 240, 320, 400, 600 and 1200 grit SiC, and 1 μm Al_2O_3 abrasive to produce a uniform flaw distribution on one side. Each disc was then remounted and ground on the opposite side by 240, 320 and 400 grit SiC abrasive to ensure parallel surfaces and a uniform thickness of 1.8 mm.

After polishing, the discs were annealed for 2 h at 450°C and slowly cooled in the furnace by turning off the power supply. This procedure was necessary to relieve polishing-induced stresses and to ensure that all samples

had a well defined thermal history. All discs were annealed in groups of 10 in the same furnace to minimize variations in thermal processing.

Once the discs were annealed, each was indented by a microhardness tester (Model MO Tukon Microhardness Tester, Wilson Instruments Inc., Binghamton, NY) at the center of the finely polished side with a Vickers indenter. An indentation load of 14.7 N was used for all samples. Previous testing by Naman (1994) indicated that this load produced crack sizes of sufficient size to yield fracture toughness values in the plateau region of R-curve behavior exhibited by lithia disilicate glass-ceramics. A drop of paraffin oil was placed on the indentation site prior to indentation to minimize the effects of environmentally assisted crack growth.

Within 30 min of indentation, each disc was fractured using a biaxial flexure test as described by Wachtman *et al.* (1972). In biaxial flexure testing, a disc specimen is supported on three or more points near its periphery and equidistant from its center. The disc is loaded on its upper surface at the center point using a piston or ball. A piece of polymer tape (Type 471, 3M Corporation, St. Paul, MN) is placed on the loading side prior to testing to ensure that the load was evenly distributed over the entire loading area. The maximum tensile stress occurs at the center of the lower surface of the disc. Since the disc is supported inside its periphery, the strength should be independent of edge effects.

In this study, specimens were fractured in an Instron Testing Machine (Model 1125, Instron Corporation, Canton, MA) using a piston-on-three-ball fixture (Figure 3.2). The supporting balls and loading piston were made of stainless steel. The three-ball supporting ring and loading piston had diameters of 12 mm and 1.6 mm respectively. A piece of polymeric tape (3M Type 471, 3M Corporation, St. Paul, MN) was placed on the loading side of each disc to ensure that the load was distributed evenly (Thompson and Anusavice, 1994). All

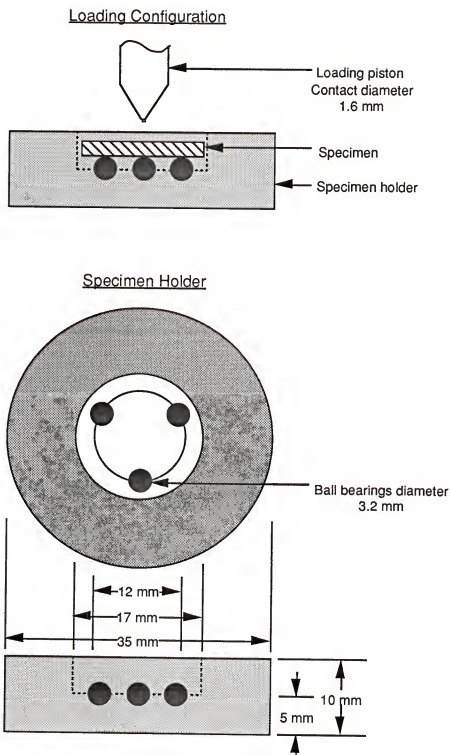


Figure 3.2. Piston-on-three-ball biaxial flexure fixture.

measurements were made in air at room temperature, using a loading rate of 0.5 mm/min. The flexure strength of each disc was calculated using the following equations (Wachtman *et al.*, 1972):

$$\sigma_f = -\frac{3P}{4\pi t^2}(X - Y) \quad (3.3)$$

where

$$X = (1 + \nu) \ln \left(\frac{r_0}{b} \right)^2 + \left[\frac{(1 - \nu)}{2} \right] \left(\frac{r_0}{b} \right)^2 \quad (3.4)$$

and

$$Y = (1 + \nu) \left[1 + \ln \left(\frac{a}{b} \right)^2 \right] + (1 - \nu) \left(\frac{a}{b} \right)^2 \quad (3.5)$$

In this set of equations, P is the applied load at failure, t is the specimen thickness, r_0 is the radius of the piston at the contacting surface, b is the specimen radius and a is the radius of the support circle. For small r_0 , which was the case in this set of experiments where a flat punch was used as the loading piston, an effective value of r_0 was calculated using the following equation developed by Marshall (1980):

$$r_0^* = \left(1.6r_0^2 + t^2 \right)^{1/2} - 0.675t \quad (3.6)$$

For all calculations of biaxial flexure strength, r_0^* , the effective value of r_0 , was used.

The fractured biaxial flexure specimens were analyzed using quantitative fractography. The fractured pieces of each disc were cleaned and sputter-coated (Hummer II Sputter Coater, Anatech, Ltd., Alexandria, VA) with gold-palladium. The fracture surfaces were examined with an optical microscope, and the fracture surface features were measured with a filar eyepiece. The characteristic

fracture surface features exhibited by glass-ceramics can be seen in Figure 3.3. For most of the indented biaxial flexure specimens used in this study, the effective flaw size, c , was measured using optical microscopy. Some specimens with crystal volume fractions greater than or equal to 0.60 required scanning electron microscopy (Model 6400, Joel Corporation, Tokyo, Japan) to accurately measure the critical flaw dimensions. All flaws observed in this study were semielliptical in shape. The following relationship (Mecholsky *et al.*, 1977) was used to calculate flaw size:

$$c = (ab)^{1/2} \quad (3.7)$$

where a and b are the depth and half-width of the flaw, respectively.

Since all biaxial flexure specimens in this study failed from well defined surface flaws, the fracture toughness was calculated using basic fracture mechanics relationships. The relationship between the flaw size, c , and the failure stress, σ_f , of brittle materials with surface flaws that are in planes perpendicular to the applied stress, and are elliptical in shape is well documented in the fracture mechanics literature (Randall, 1966; Mecholsky *et al.*, 1976). The derived stress intensity factor for an elliptical crack is of the form (Green and Sneddon, 1950; Irwin and Paris, 1971)

$$K_I = \frac{\sigma(\pi a)^{1/2}}{\Phi} \left(\frac{a^2}{b^2} \cos^2 \phi + \sin^2 \phi \right)^{1/4} \quad (3.8)$$

where σ is the applied stress, a is the minor axis of the ellipse, b is the major half-axis and ϕ is an angle which describes the a/b ratio. The term Φ is a complete integral of the second kind, and is defined as

$$\Phi = \int_0^{\pi/2} \left[\sin^2 \phi + \frac{a^2}{b^2} \cos^2 \phi \right]^{1/2} d\phi \quad (3.9)$$

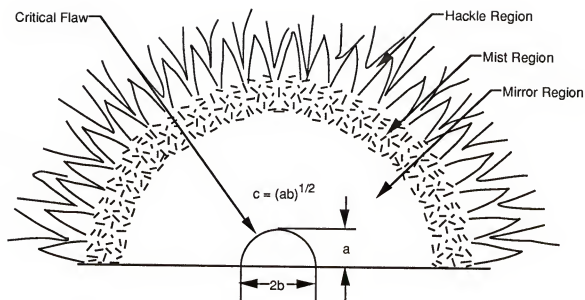


Figure 3.3. General appearance of features on a typical glass-ceramic fracture surface.

and has a value of $\Phi = \pi/2$ for $a/b = 1$. For the elliptical crack in an infinite medium under tensile loading, the point of maximum stress intensity occurs at the intersection of the minor axis with the ellipse, where the stress intensity is defined by

$$K_I = \frac{\sigma(1.2\pi a)^{1/2}}{\Phi} \quad (3.10)$$

Equation (3.10) is often written in the general form

$$K_I = Y\sigma(a)^{1/2} \quad (3.11)$$

where Y is defined as a crack-geometry parameter. Equation (3.10) was modified by Irwin and Paris (1971) to account for plasticity around the flaw. For a semicircular surface crack subjected to a far field stress, that is free of residual stress and that is small relative to the thickness of the cross-section, $\phi = 1.57$ and equation (3.11) becomes

$$K_I = 1.24\sigma(c)^{1/2} \quad (3.12)$$

where c is the flaw size defined by equation (3.7). The value of Y in equation (3.12) has been applied to many glasses, glass-ceramics, and ceramics (Rice, 1974; Mecholsky *et al.*, 1976). This form is generally accepted as valid for studies of glasses and ceramics.

For indented samples, such as the biaxial flexure specimens in this study, equation (3.11) must be modified to account for the residual stresses brought about by the indentation process. Marshall *et al.* (1979) redefined the stress intensity for an indented specimen subjected to an applied stress as

$$K_I = \frac{\chi P}{c^{3/2}} + Y\sigma(c)^{1/2} \quad (3.13)$$

where χ characterizes the intensity of the driving force that develops from indentation-induced residual stresses, P is the indentation load and c is the flaw size. Equation (3.13) describes a system in which equilibrium is maintained by stable growth of the flaw with increasing stress and can be solved for the applied stress as a function of flaw size:

$$\sigma = \left[\frac{K_I}{(Yc)^{1/2}} \right] \left[1 - \frac{\chi P}{K_I(c)^{3/2}} \right] \quad (3.14)$$

For $d\sigma/dc = 0$, equation (3.14) has a maximum at

$$\sigma_m = \frac{3K_{IC}}{4Yc_m^{1/2}} \quad (3.15a)$$

$$c_m = \left(\frac{4\chi P}{K_{IC}} \right)^{2/3} \quad (3.15b)$$

where σ_m is the maximum applied stress and c_m is the maximum crack size. If the failure stress and critical flaw size are measured directly, the fracture toughness, K_{IC} , can be determined directly from equation (3.15a) (Cook and Lawn, 1983):

$$K_{IC} = \left(\frac{4Y}{3} \right) \sigma_f(c)^{1/2} \quad (3.16)$$

where σ_f is now the fracture strength and c is the critical flaw size as defined in equation (3.7). Using the Y parameter value of equation (3.12), equation (3.16) becomes

$$K_{IC} = 1.65\sigma_f(c)^{1/2} \quad (3.17)$$

The fracture toughness of each biaxial flexure disc specimen was calculated using equation (3.17) and the measured values of σ_f and c .

3.3.2 Controlled-Flaw Strength Method

The use of indentation techniques to evaluate the fracture toughness of brittle materials is well established (Evans, 1974; Evans and Charles, 1976; Lawn and Marshall, 1979). The controlled-flaw strength method developed by Chantikul *et al.* (1981) was utilized to obtain a supplementary value of toughness for the disc specimens described in the previous section. This method provided another means of calculating the fracture toughness of the indented biaxial flexure specimens, without requiring any additional sample preparation or analysis. This approach eliminates the need for fractographic measurements of the flaw size from either the indented surface or the fracture surface. The method requires knowledge of the elastic modulus and hardness of the material being tested, but is independent of changes in flaw configuration caused by postindentation growth.

An expression for fracture toughness based on fracture strength and indentation load, that does not include a parameter related to flaw size, can be derived from equations (3.15a) and (3.15b). If the definition of c_m , described by equation (3.15b), is inserted into equation (3.15a), and the subscript m is dropped from the notation, based on the condition that σ now refers to the as-indent strength, the following expression is obtained (Chantikul *et al.*, 1981):

$$K_{IC} = \frac{256}{27} \left[(\pi Y)^{1/2} (\chi P)^{1/3} \sigma \right]^{3/4} \quad (3.18)$$

The parameter χ has been defined by Anstis *et al.* (1981) as

$$\chi = \xi_v^n (E/H)^{1/2} \quad (3.19)$$

where ξ_V^R is a material-independent constant for Vickers-produced radial cracks, E is the elastic modulus of the material and H is the hardness. If the definition of χ is substituted into equation (3.18) it becomes

$$K_{IC} = \eta_V^R (E/H)^{1/8} (\sigma_f P^{1/3})^{3/4} \quad (3.20)$$

where η_V^R is a geometrical constant defined as

$$\eta_V^R = \left[(256/27) (\pi \gamma)^{3/2} \xi_V^R \right]^{1/4} \quad (3.21)$$

and σ_f is the indented fracture strength. Chantikul *et al.* (1981) determined a value of $\eta_V^R = 0.59 \pm 0.12$ through experimental analysis of several ceramic materials. Equation (3.20) was used to calculate the fracture toughness of each indented biaxial flexure disc specimen tested in this study.

The elastic modulus and hardness were not substituted into equation (3.20) as separate parameters when the toughness calculations were performed. Instead, the ratio E/H was determined as a single variable using a technique developed by Marshall *et al.* (1982). The method is based on measurement of the elastic recovery of surface dimensions of Knoop indentations. When fully loaded, a and b are controlled by the indenter geometry such that $a/b = 7.11$. However, when unloaded, the length of the shorter indentation diagonal, b , is reduced because of elastic recovery, whereas the longer diagonal, a , remains relatively unaffected. The extent of this recovery is related to the hardness-to-elastic modulus ratio. A diagram of this behavior is shown in Figure (3.4).

Marshall *et al.* (1982) used elastic theory to derive a solution for the ratio of the unloaded indentation diagonals, a' and b' . The elastic displacements that occur in the material surrounding the indentation site are determined by the hardness and elastic modulus of the material. Calculation of the displacements

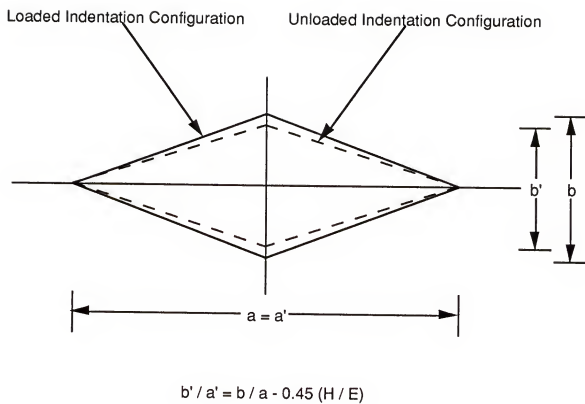


Figure 3.4. Configuration of Knoop indentation impression used in the determination of E/H ratio.

of the unloaded indentation diagonals is related to the solution for an elliptical hole subject to uniaxial stress. The ratio of the unloaded indentation diagonals is given by the following equation:

$$\frac{b'}{a'} = \frac{b}{a} - \alpha \left(\frac{H}{E} \right) \quad (3.22)$$

where α is a constant, H is the hardness and E is the elastic modulus. The constant α was determined experimentally through data fitting, and has a value of 0.45. The E/H ratio for each of the 17 $\text{Li}_2\text{O} \cdot 2\text{SiO}_2$ microstructures in this study was determined using this method.

The E/H values used in equation (3.20) were mean values obtained from optical microscopy measurements of Knoop indentations on polished and annealed specimens representing each of the different microstructures. Fifteen indentations, five each at loads of 4.9 N, 9.8 N and 14.7 N, were made and measured on two specimens for each microstructure. Care was taken to ensure that indentations were at least three indenter lengths from each other. All indentations were made in air at room temperature using a microhardness tester (Model MO Tukon Microhardness Tester, Wilson Instruments Inc., Binghamton, NY). Measurements of the indentation diagonals were made immediately following indentation.

3.4 Finite Element Stress Analysis

Finite element stress analyses were performed to estimate the maximum stresses and stress distribution adjacent to spherical and elliptical particles in a glass matrix. The stresses are produced as a result of thermal expansion and elastic modulus mismatch between the crystal phase and the glass phase. The ANSYS computer code (ANSYS 5.0, Swanson Analysis Systems, Inc., Houston,

PA) was used to perform two-dimensional elastic analyses. A finite element mesh was generated using a two-dimensional, eight-node quadratic solid element type (PLANE82). The axisymmetric option was chosen. Examples of typical finite element layouts used in this study are shown in Figures 3.5 through 3.7. Finite element analysis codes developed for: 1) a spherical crystal in a glass matrix, 2) an elliptical crystal in a glass matrix, and 3) two spherical crystals in a glass matrix are listed in Appendices A, B and C respectively. The material properties used for the glass phase were: elastic modulus ($E = 70 \text{ GPa}$), Poisson's ratio ($\nu = 0.27$), and coefficient of thermal expansion ($\alpha = 12.8 \times 10^{-6}/^{\circ}\text{C}$). The material properties used for the crystal phase were: elastic modulus ($E = 145 \text{ GPa}$), Poisson's ratio ($\nu = 0.20$), and coefficient of thermal expansion ($\alpha = 10.8 \times 10^{-6}/^{\circ}\text{C}$). The material properties were obtained from experimental techniques described earlier. The temperature range over which computer analyses were performed was 450°C to 25°C . This temperature range represents the cooling process from the annealing temperature (450°C) to the ambient temperature (25°C). The principal stresses adjacent to the interface between the crystal and the glass matrix were computed.

3.5 Microcrack Density Determination

The mean microcrack densities were determined using quantitative stereology. Two cross sections for each of two samples of each microstructure were polished through $0.005 \mu\text{m Al}_2\text{O}_3$. Micrographs were recorded for randomly selected areas. At least one area was selected for each cross section, with a total of six areas selected for each microstructure. A ruled overlay with a total length, 10 lines totaling 2.05 mm in the scale of the graph, was applied to each micrograph. The number of intersections with the ruled lines was recorded for

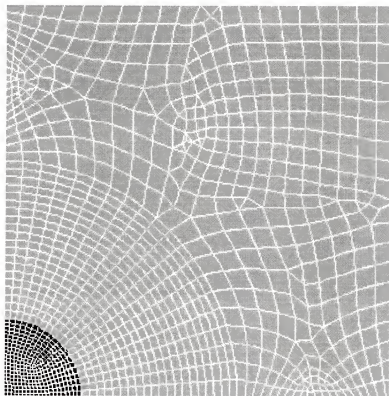


Figure 3.5. Schematic of a typical finite element layout used for the computation of thermal stresses adjacent to a spherical crystal in a glass matrix.

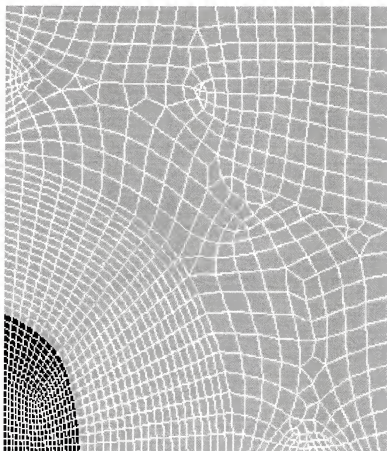


Figure 3.6. Schematic of a typical finite element layout used for the computation of thermal stresses adjacent to an elliptical crystal in a glass matrix.

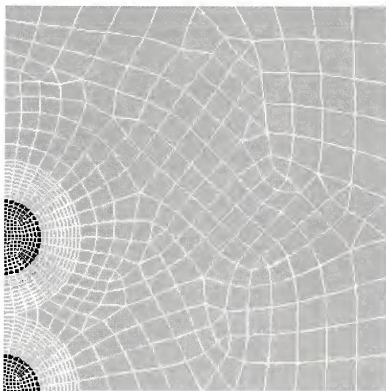


Figure 3.7. Schematic of a typical finite element layout used for the computation of thermal stresses adjacent to two spherical crystals in a glass matrix.

each micrograph. The microcrack density, defined to be the value of microcrack surface area per unit test volume, $(S_V)_{mc}$, was determined for each micrograph using the following relationship:

$$(S_V)_{mc} = 2(P_L)_{mc} \quad (3.23)$$

where $(P_L)_{mc}$ is the number of intersections with microcracks per unit length of test line (Underwood, 1970; Mackert *et al.*, 1994).

3.6 Fractal Analysis

3.6.1 Slit Island Technique

The fractal dimensions of the fracture surfaces of lithia disilicate discs were determined using the Richardson technique (Mecholsky and Plaia, 1991) on slit island contours (Mandelbrot *et al.*, 1984). The fractured disks were cleaned ultrasonically in ethanol. A negative replica of the fracture surface of each specimen was produced using a low-viscosity polyvinylsiloxane impression material (ExtrudeTM Type I, Kerr Manufacturing Co., Romulus, MI) (Figure 3.8). The impressions were degassed for 12 h at room temperature, and then filled with an epoxy resin (Leco Epoxide Resin, Leco Corp., St. Joseph, MI) to produce a replica of the fracture surface. Each epoxy replica was cured for 1 h at 60°C and sputter coated with gold-palladium alloy for 8 min. The coated replicas were transferred to plastic molds, with the fracture surface pointed upward, and the completely covered with the same epoxy resin from which they were fabricated (Figure 3.9). The gold-palladium coating provides a clear contrast between the replica and the epoxy in which it is mounted. The mounted replicas were returned to the curing oven for an additional cure of 1 h.

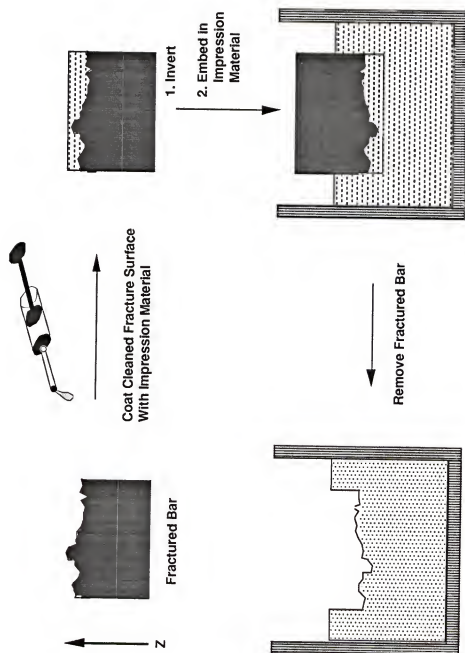


Figure 3.8. Procedure to create a negative replica of a fracture surface.

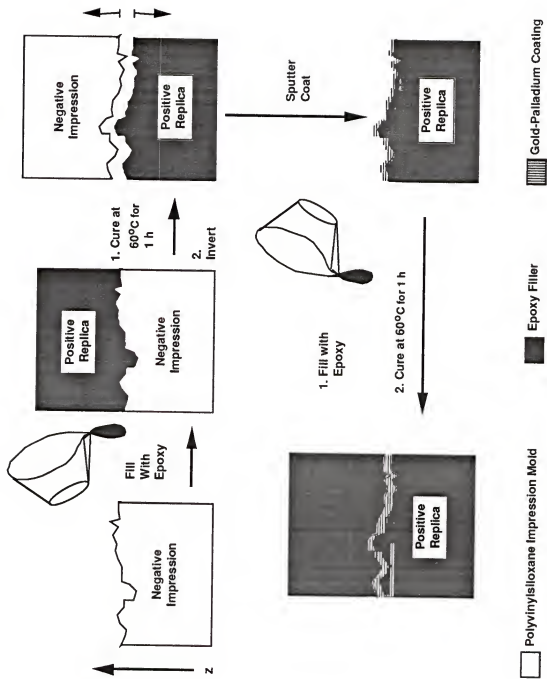


Figure 3.9. Procedure to create a positive replica of a fracture surface.

The embedded replicas were polished approximately parallel to the fracture surface with 1200 grit SiC abrasive until sections of the fracture surface appeared in the polishing plane. These sections appear as islands or boundaries, analogous to coastlines of equal elevation (Figure 3.10). Once a boundary appears the samples were polished for approximately 3 min with 1 μm Al_2O_3 abrasive to increase resolution. Each sample was then viewed at a magnification of 200X using an optical microscope. The boundary, represented by the gold-palladium layer, was photographed 7 to 10 times along its length to create a montage (Figure 3.11). Two boundaries, located at different areas on the fracture surface, were prepared for each specimen analyzed in this study. The boundaries were measured from the montages according to the Richardson equation (Mandelbrot, 1982):

$$L = kS^{1-D} \quad (3.24)$$

where L is the total length of the selected line segment, S is the length of the measuring unit, D is the fractal dimension, and k is a proportionality constant. The total length, L , was measured two times for each different measuring unit, S , to ensure accuracy. Richardson plots of $\log L$ versus $\log S$ were constructed for each sample. These graphs represent the change in the measured length of a line as a function of the scale. A minimum of seven different measuring units (S) were used, ranging from 2.5 to 20.0 μm , in the construction of the Richardson plot of each specimen. The fractal dimensional increment, D^* , was determined from the slope ($-D^*$) of the generated line. An example of a Richardson plot, constructed in this study, is shown in Figure 3.12.

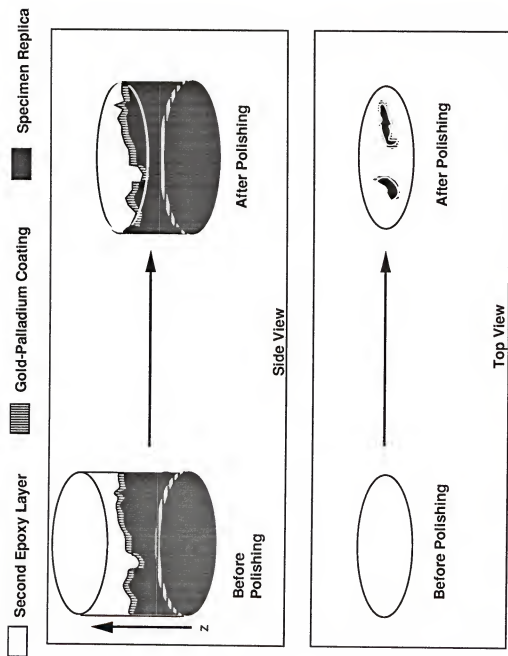


Figure 3.10. Schematic illustration of slit island technique. Coastlines are revealed by polishing parallel to the fracture surface.

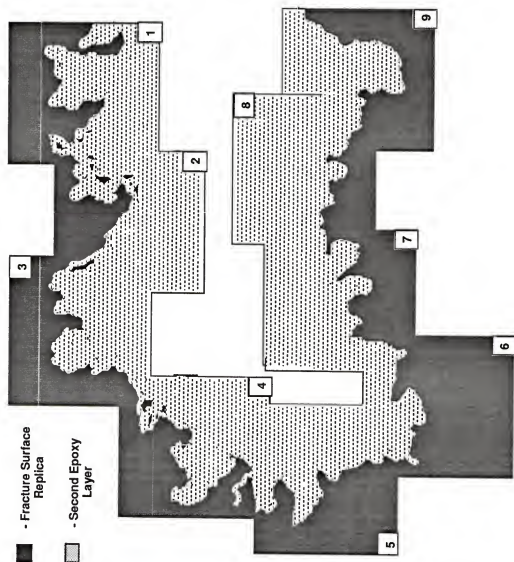


Figure 3.11. Schematic representation of a montage of photographs of the boundary polished sectioned replica of a specimen fracture surface.

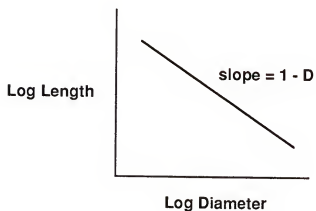
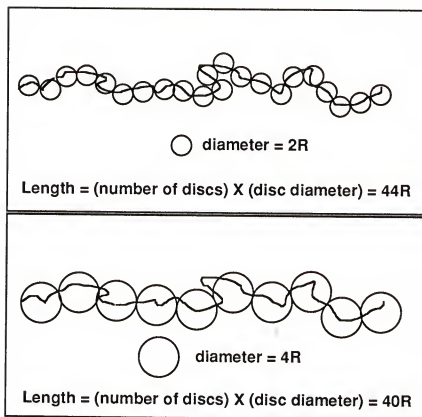


Figure 3.12. Illustration of Richardson plot based on measurements of the fracture surface boundary.

3.6.2 Atomic Force Microscopy Box Counting Technique

Fractal dimensions were also measured through analysis of high resolution three-dimensional atomic force microscopy (AFM) images (Nanoscope® III Scanning Probe Microscope, Digital Instruments, Inc., Santa Barbara, CA). Images were obtained from different areas of the fracture surface of each specimen that was analyzed using the slit-island method. A three-dimensional AFM image of a lithia disilicate fracture surface is shown in Figure 3.13. The AFM technique employed in this study determined the fractal dimension of an image using a box counting method (Mandelbrot, 1982; Takayasu, 1990). A three-dimensional array of cubes was superimposed on the three-dimensional image so that the cubes encompassed the entire image. The size of the cubes was varied and the number of cubes intersected by the image was recorded for each cube size. Fractal dimensions were determined from Richardson plots of the log of the cell size versus the log of the cell count. Fractal analysis was performed on different regions of the fracture surface of each specimen to assess the effect of location, distance and direction from the critical flaw, on the fractal dimension.

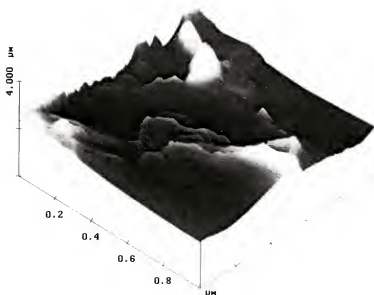


Figure 3.13. Atomic force microscope image of the fracture surface of a lithia disilicate specimen.

CHAPTER 4 RESULTS

4.1 Microstructure

Optical micrographs of polished and etched cross sections of each glass-ceramic specimen group are shown in Figures 4.1 to 4.17. The variable t_n represents the nucleation time used in the crystallization process. All specimens displayed a spherulitic crystal morphology. Specimens with crystal volume fractions, V_f , of 0.98 displayed some closed porosity. The volume fraction of porosity of these specimens varied between 0.02 and 0.04. The mean crystal size of each microstructure, with 95% confidence intervals, and the crystal aspect ratios are listed in Table 4.1.

4.2 Physical Properties

4.2.1 Glass Transition Temperature

Multiple differential thermal analysis (DTA) measurements, μV versus T , of the lithia disilicate glass indicated a glass transition temperature range from 452°C to 474°C. A sample DTA measurement is shown in Figure 4.18a. These results were confirmed by differential scanning calorimetry (DSC). The DSC

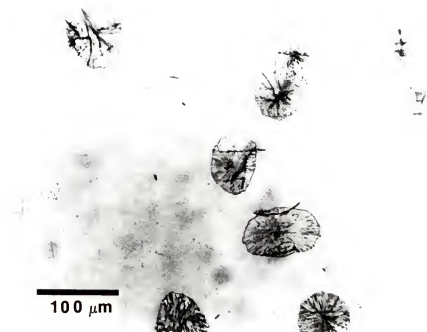


Figure 4.1. Optical micrograph of a lithia disilicate glass-ceramic with $V_f = 0.10$. (Nucleation treatment: $470^\circ\text{C} / 0.25 \text{ h}$; crystal growth treatment: $600^\circ\text{C} / 30 \text{ min}$; mean crystal size: $75.4 \pm 4.1 \mu\text{m}$)

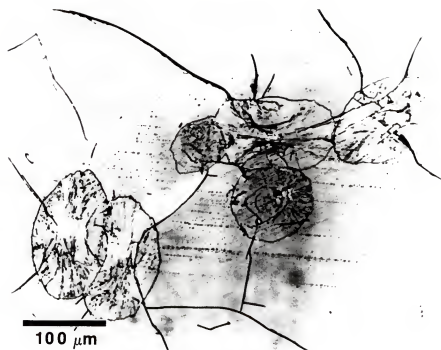


Figure 4.2. Optical micrograph of a lithia disilicate glass-ceramic with $V_f = 0.30$. (Nucleation treatment: $470^\circ\text{C} / 0.25 \text{ h}$; crystal growth treatment: $600^\circ\text{C} / 50 \text{ min}$; mean crystal size: $85.6 \pm 14.8 \mu\text{m}$)

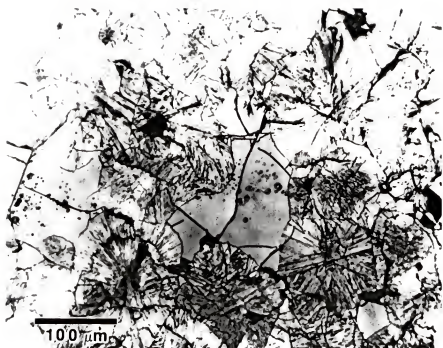


Figure 4.3. Optical micrograph of a lithia disilicate glass-ceramic with $V_f = 0.70$. (Nucleation treatment: 470°C / 0.25 h; crystal growth treatment: 600°C / 60 min; mean crystal size: $103.3 \pm 11.6 \mu\text{m}$)



Figure 4.4. Optical micrograph of a lithia disilicate glass-ceramic with $V_f \approx 0.98$. (Nucleation treatment: $470^\circ\text{C} / 0.25 \text{ h}$; crystal growth treatment: $600^\circ\text{C} / 70 \text{ min}$; mean crystal size: $142.6 \pm 26.8 \mu\text{m}$)

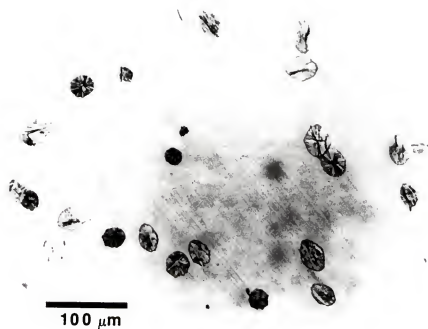


Figure 4.5. Optical micrograph of a lithia disilicate glass-ceramic with $V_f = 0.10$. (Nucleation treatment: 470°C / 1.5 h; crystal growth treatment: 600°C / 13 min; mean crystal size: $27.0 \pm 2.3 \mu\text{m}$)

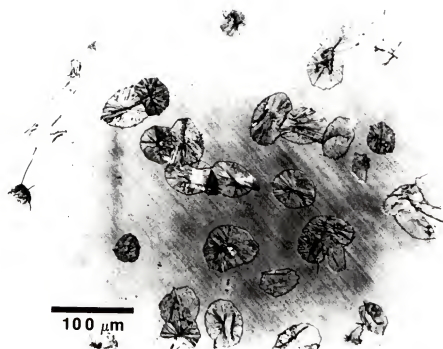


Figure 4.6. Optical micrograph of a lithia disilicate glass-ceramic with $V_f = 0.30$. (Nucleation treatment: $470^\circ\text{C} / 1.5 \text{ h}$; crystal growth treatment: $600^\circ\text{C} / 20 \text{ min}$; mean crystal size: $45.9 \pm 3.5 \mu\text{m}$)



Figure 4.7. Optical micrograph of a lithia disilicate glass-ceramic with $V_f = 0.70$. (Nucleation treatment: 470°C / 1.5 h; crystal growth treatment: 600°C / 26 min; mean crystal size: $58.5 \pm 5.2 \mu\text{m}$)

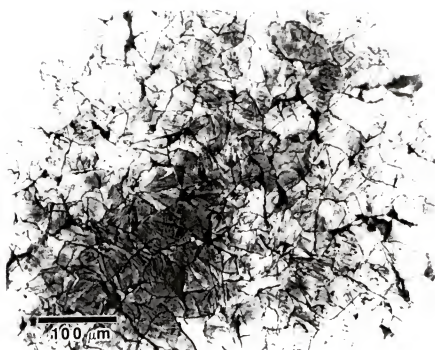


Figure 4.8. Optical micrograph of a lithia disilicate glass-ceramic with $V_f \approx 0.98$. (Nucleation treatment: 470°C / 1.5 h; crystal growth treatment: 600°C / 35 min; mean crystal size: $65.4 \pm 6.4 \mu\text{m}$)

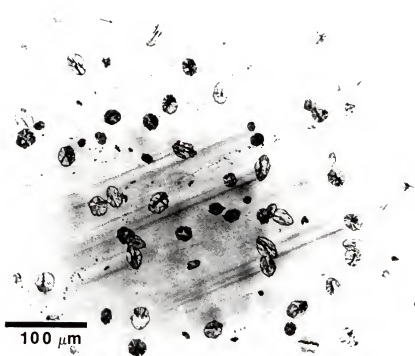


Figure 4.9. Optical micrograph of a lithia disilicate glass-ceramic with $V_f = 0.10$. (Nucleation treatment: $470^{\circ}\text{C} / 4 \text{ h}$; crystal growth treatment: $600^{\circ}\text{C} / 9 \text{ min}$; mean crystal size: $18.0 \pm 1.8 \mu\text{m}$)

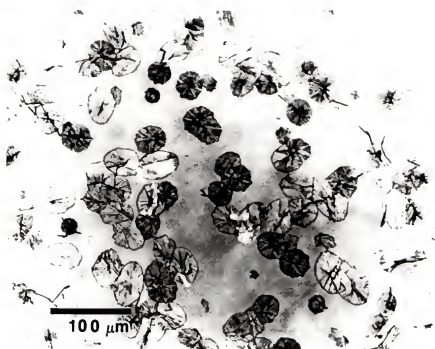


Figure 4.10. Optical micrograph of a lithia disilicate glass-ceramic with $V_f = 0.30$. (Nucleation treatment: $470^{\circ}\text{C} / 4 \text{ h}$; crystal growth treatment: $600^{\circ}\text{C} / 13 \text{ min}$; mean crystal size: 28.8 ± 2.2)

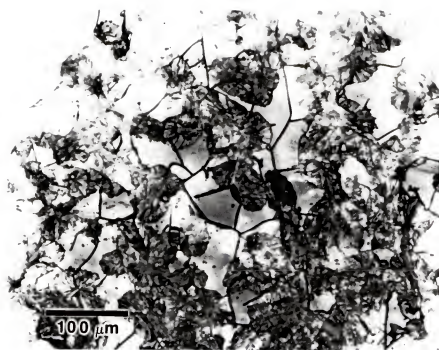


Figure 4.11. Optical micrograph of a lithia disilicate glass-ceramic with $V_f = 0.70$. (Nucleation treatment: $470^\circ\text{C} / 4 \text{ h}$; crystal growth treatment: $600^\circ\text{C} / 16 \text{ min}$; mean crystal size: $39.3 \pm 2.5 \mu\text{m}$)

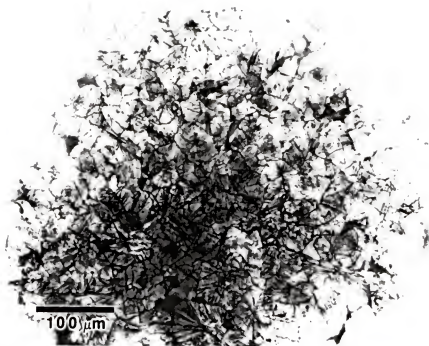


Figure 4.12. Optical micrograph of a lithia disilicate glass-ceramic with $V_f \approx 0.98$. (Nucleation treatment: 470°C / 4 h; crystal growth treatment: 600°C / 25 min; mean crystal size: $46.8 \pm 4.8 \mu\text{m}$)

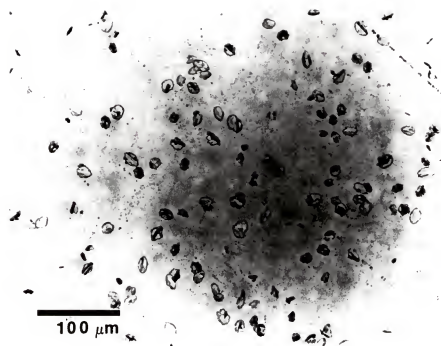


Figure 4.13. Optical micrograph of a lithia disilicate glass-ceramic with $V_f = 0.10$. (Nucleation treatment: $470^{\circ}\text{C} / 10 \text{ h}$; crystal growth treatment: $600^{\circ}\text{C} / 6 \text{ min}$; mean crystal size: $8.5 \pm 1.5 \mu\text{m}$)

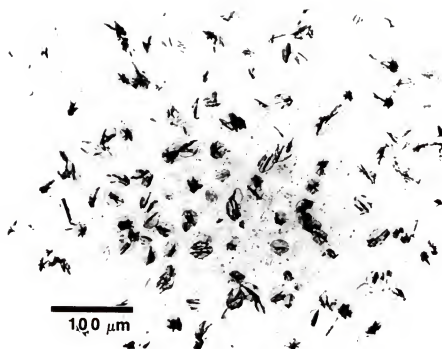


Figure 4.14. Optical micrograph of a lithia disilicate glass-ceramic with $V_f = 0.30$. (Nucleation treatment: 470°C / 10 h; crystal growth treatment: 600°C / 9.5 min; mean crystal size: $18.6 \pm 1.8 \mu\text{m}$)

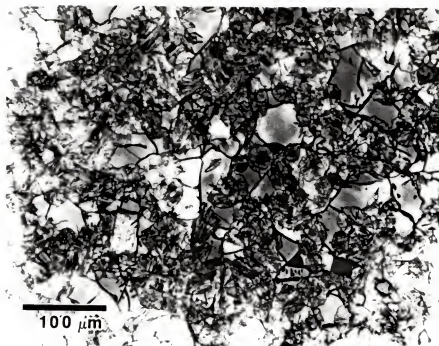


Figure 4.15. Optical micrograph of a lithia disilicate glass-ceramic with $V_f = 0.70$. (Nucleation treatment: 470°C / 10 h; crystal growth treatment: 600°C / 11 min; mean crystal size: $26.3 \pm 3.0 \mu\text{m}$)



Figure 4.16. Optical micrograph of a lithia disilicate glass-ceramic with $V_f \approx 0.98$. (Nucleation treatment: $470^\circ\text{C} / 10 \text{ h}$; crystal growth treatment: $600^\circ\text{C} / 15 \text{ min}$; mean crystal size: 27.3 ± 2.7)

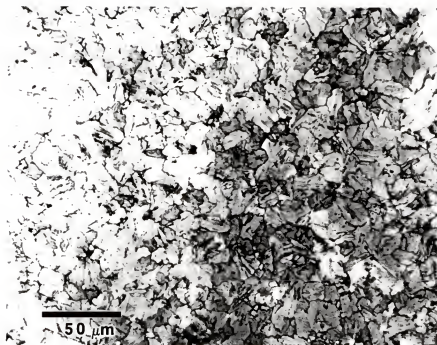


Figure 4.17. Optical micrograph of a lithia disilicate glass-ceramic with $V_f \approx 0.98$. (Nucleation treatment: 470°C / 100 h; crystal growth treatment: 600°C / 12 min; mean crystal size: $15.2 \pm 4.1 \mu\text{m}$)

Table 4.1
Mean Crystal Size and 95% Confidence Interval
for $\text{Li}_2\text{O} \cdot 2\text{SiO}_2$ Glass-Ceramics

Crystal Volume Fraction, V_f	Major Axis (μm)	Minor Axis (μm)	Average Size (μm)	Crystal Aspect Ratio
<u>$V_f = 0.10$</u>				
$t_n = 0.25 \text{ h}$	87.7 ± 7.2	63.0 ± 2.9	75.4 ± 4.1	1.39
$t_n = 1.5 \text{ h}$	30.5 ± 3.3	23.5 ± 1.6	27.0 ± 2.3	1.30
$t_n = 4 \text{ h}$	20.6 ± 2.3	15.4 ± 1.5	18.0 ± 1.8	1.34
$t_n = 10 \text{ h}$	10.1 ± 1.8	6.8 ± 1.3	8.5 ± 1.5	1.48
<u>$V_f = 0.30$</u>				
$t_n = 0.25 \text{ h}$	98.3 ± 18.3	72.8 ± 11.6	85.6 ± 14.8	1.35
$t_n = 1.5 \text{ h}$	50.5 ± 4.9	41.3 ± 2.9	45.9 ± 3.5	1.22
$t_n = 4 \text{ h}$	32.1 ± 3.0	25.5 ± 2.0	28.8 ± 2.2	1.26
$t_n = 10 \text{ h}$	20.3 ± 2.0	16.8 ± 1.6	18.6 ± 1.8	1.21
<u>$V_f = 0.70$</u>				
$t_n = 0.25 \text{ h}$	118.3 ± 17.3	88.3 ± 7.8	103.3 ± 11.6	1.34
$t_n = 1.5 \text{ h}$	65.8 ± 7.2	51.3 ± 4.6	58.5 ± 5.2	1.28
$t_n = 4 \text{ h}$	44.5 ± 3.6	34.2 ± 2.2	39.3 ± 2.5	1.30
$t_n = 10 \text{ h}$	28.7 ± 3.8	24.0 ± 2.5	26.3 ± 3.0	1.20
<u>$V_f = 0.98$</u>				
$t_n = 0.25 \text{ h}$	163.0 ± 31.9	123.0 ± 22.1	142.6 ± 26.8	1.33
$t_n = 1.5 \text{ h}$	73.8 ± 7.8	57.0 ± 5.4	65.4 ± 6.4	1.29
$t_n = 4 \text{ h}$	51.5 ± 6.1	42.0 ± 4.6	46.8 ± 4.8	1.22
$t_n = 10 \text{ h}$	30.2 ± 3.4	24.6 ± 2.0	27.3 ± 2.7	1.23
$t_n = 100 \text{ h}$	18.0 ± 4.2	12.5 ± 3.9	15.2 ± 4.1	1.44

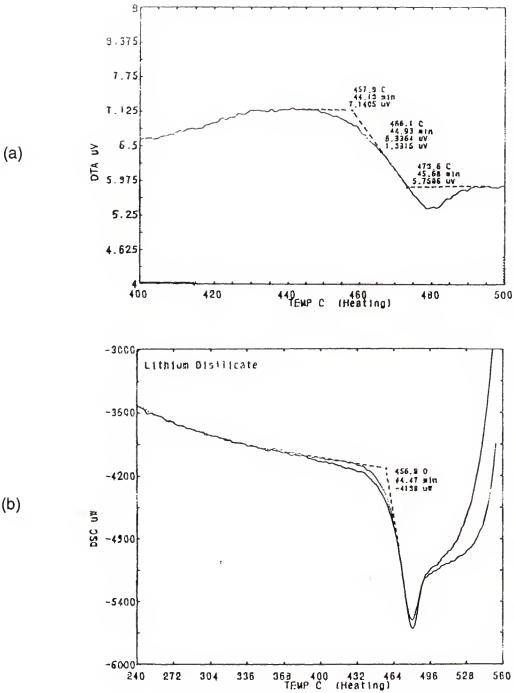


Figure 4.18. Thermal analysis results for lithia disilicate glass. (a) Exotherm profile from DTA indicates a glass transition temperature range from 452°C to 474°C. (b) The glass transition temperature range estimated from DSC profiles is 457°C to 480°C.

exotherm, μW versus T , indicates a glass transition temperature between 457°C and 480°C . A sample DSC measurement is shown in Figure 4.18b.

4.2.2 Thermal Expansion Coefficient

The coefficient of thermal expansion, α , measured from 25°C to 450°C , varied between $9.2 \times 10^{-6}/^\circ\text{C}$ for one type of fully crystalline glass-ceramic ($t_n = 0.25$ h, $V_f \approx 0.98$) and $12.8 \times 10^{-6}/^\circ\text{C}$ for glass specimens. The mean coefficient of thermal expansion values of specimens with crystal volume fractions of 0.10, 0.30 and 0.98 for nucleation times of 0.25 h and 10 h are shown in Table 4.2. The mean α values are also given for lithia disilicate glass and for fully crystalline lithia disilicate specimens that were nucleated for 100 h. In addition, mean α values are plotted as a function of crystal volume fraction in Figure 4.19. The upper curve ($t_n = 10$ h) and lower curve ($t_n = 0.25$ h) in Figure 4.19 represent glass-ceramics with different mean crystal sizes.

4.2.3 Density

The bulk density of monolithic samples ranged from 2.32 g/cc for lithia disilicate glass to 2.39 g/cc for fully crystalline lithia disilicate nucleated for 100 h. The true density of powder samples ranged from 2.32 g/cc for lithia disilicate glass to 2.44 g/cc for fully crystalline ($V_f \approx 0.98$) lithia disilicate specimens nucleated for 4 h, 10 h and 100 h. The mean bulk density and true density of each lithia disilicate microstructure analyzed in this study are listed in Table 4.3. In addition, bulk density values are also plotted as a function of crystal volume fraction in Figure 4.20.

Table 4.2
Coefficient of Thermal Expansion, α , for $\text{Li}_2\text{O} \cdot 2\text{SiO}_2$ Glass-Ceramics

Material	α ($\times 10^{-6}/^\circ\text{C}$)
Glass	12.8
Glass-Ceramic ($t_n = 0.25$ h, $V_f = 10\%$)	11.9
Glass-Ceramic ($t_n = 0.25$ h, $V_f = 30\%$)	10.5
Glass-Ceramic ($t_n = 0.25$ h, $V_f \approx 98\%$)	9.2
Glass-Ceramic ($t_n = 10$ h, $V_f = 10\%$)	12.4
Glass-Ceramic ($t_n = 10$ h, $V_f = 30\%$)	12.1
Glass-Ceramic ($t_n = 10$ h, $V_f \approx 98\%$)	10.2
Glass-Ceramic ($t_n = 100$ h, $V_f \approx 98\%$)	10.8

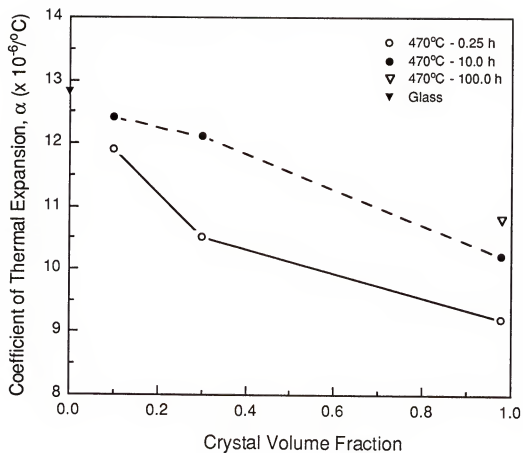


Figure 4.19. Effect of crystallization on the coefficient of thermal expansion of lithia disilicate glass-ceramics.

Table 4.3

Mean Bulk Density and True Density for $\text{Li}_2\text{O} \cdot 2\text{SiO}_2$ Glass-Ceramics

Crystal Volume Fraction, V_f	Bulk Density (g/cc)	True Density (g/cc)
Glass	2.32	2.32
<u>$V_f = 0.10$</u>		
$t_n = 0.25$ h	2.33	2.33
$t_n = 1.5$ h	2.33	2.33
$t_n = 4$ h	2.33	2.33
$t_n = 10$ h	2.33	2.33
<u>$V_f = 0.30$</u>		
$t_n = 0.25$ h	2.34	2.35
$t_n = 1.5$ h	2.34	2.36
$t_n = 4$ h	2.35	2.36
$t_n = 10$ h	2.35	2.36
<u>$V_f = 0.70$</u>		
$t_n = 0.25$ h	2.34	2.39
$t_n = 1.5$ h	2.35	2.39
$t_n = 4$ h	2.36	2.40
$t_n = 10$ h	2.36	2.39
<u>$V_f \approx 0.98$</u>		
$t_n = 0.25$ h	2.34	2.42
$t_n = 1.5$ h	2.36	2.43
$t_n = 4$ h	2.37	2.44
$t_n = 10$ h	2.38	2.44
$t_n = 100$ h	2.39	2.44

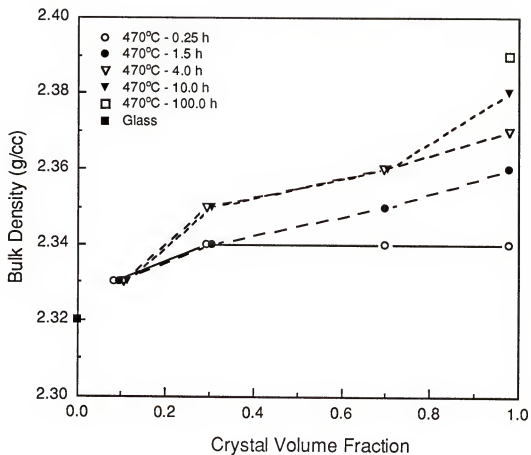


Figure 4.20. Effect of crystallization on the bulk density of lithia disilicate glass-ceramics.

4.2.4 Poisson's Ratio and Elastic Modulus

Poisson's ratio ranged from 0.19 for fully crystalline lithia disilicate specimens that were nucleated for 100 h to 0.30 for lithia disilicate glass-ceramics that were nucleated for either 1.5, 4 or 10 h ($V_f = 0.10$). The elastic modulus ranged from 68 GPa for the lithia disilicate glass-ceramic that was nucleated for 0.25 h ($V_f = 0.10$) to 137 GPa for the fully crystalline lithia disilicate ($V_f \approx 0.98$) nucleated for 100 h. Poisson's ratio and elastic modulus of lithia disilicate glass-ceramics are listed in Table 4.4. Elastic modulus values are also plotted as a function of crystal volume fraction in Figure 4.21.

4.3 Fracture Toughness

4.3.1 Fracture Toughness Determined by Quantitative Fractography

The mean fracture toughness, K_{IC} , determined by quantitative fractography ranged from 0.97 MPa·m^{1/2} for lithia disilicate glass to 3.14 MPa·m^{1/2} for lithia disilicate glass-ceramic ($V_f = 0.98$) that was nucleated for 100 h. The mean fracture toughness values and 95% confidence intervals of lithia disilicate glass-ceramics (determined by quantitative fractography using equation 3.18) are listed in Table 4.5. The mean critical flaw sizes and 95% confidence intervals are also listed in Table 4.5. The mean controlled-flaw flexure strength values and 95% confidence intervals are listed in Table 4.6 and are plotted as a function of crystal volume fraction in Figure 4.22. A plot of K_{IC} vs. V_f is shown in Figure 4.23. Scanning electron micrographs of typical lithia disilicate glass-ceramic fracture surfaces are shown in Figures 4.24, 4.25 and 4.26.

Table 4.4

Poisson's Ratio and Elastic Modulus for $\text{Li}_2\text{O} \cdot 2\text{SiO}_2$ Glass-Ceramics

Crystal Volume Fraction, V_f	Poisson's Ratio	Elastic Modulus (GPa)
Glass	0.27	70
<u>$V_f = 0.10$</u>		
$t_n = 0.25$ h	0.29	71
$t_n = 1.5$ h	0.30	71
$t_n = 4$ h	0.30	73
$t_n = 10$ h	0.30	74
<u>$V_f = 0.30$</u>		
$t_n = 0.25$ h	0.27	68
$t_n = 1.5$ h	0.26	80
$t_n = 4$ h	0.24	83
$t_n = 10$ h	0.25	88
<u>$V_f = 0.70$</u>		
$t_n = 0.25$ h	0.24	69
$t_n = 1.5$ h	0.23	88
$t_n = 4$ h	0.24	96
$t_n = 10$ h	0.23	104
<u>$V_f = 0.98$</u>		
$t_n = 0.25$ h	0.26	71
$t_n = 1.5$ h	0.24	92
$t_n = 4$ h	0.22	105
$t_n = 10$ h	0.20	115
$t_n = 100$ h	0.19	137

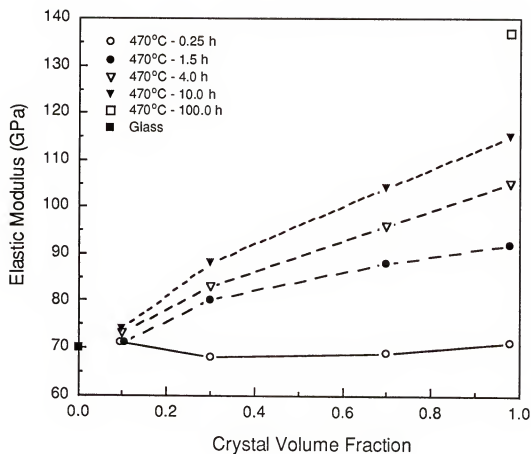


Figure 4.21. Effect of crystallization on the elastic modulus of lithia disilicate glass-ceramics.

Table 4.5

Mean Fracture Toughness (Determined by the Quantitative Fractography Method) and Mean Critical Flaw Size and 95% Confidence Intervals for $\text{Li}_2\text{O} \cdot 2\text{SiO}_2$ Glass-Ceramics

Crystal Volume Fraction, V_f	Critical Flaw Size, c (μm)	Fracture Toughness, K_{IC} ($\text{MPa} \cdot \text{m}^{1/2}$)
Glass	120 ± 11	0.97 ± 0.03
<u>$V_f = 0.10$</u>		
$t_n = 0.25 \text{ h}$	127 ± 13	1.27 ± 0.10
$t_n = 1.5 \text{ h}$	126 ± 15	1.24 ± 0.04
$t_n = 4 \text{ h}$	138 ± 20	1.29 ± 0.07
$t_n = 10 \text{ h}$	123 ± 21	1.32 ± 0.09
<u>$V_f = 0.30$</u>		
$t_n = 0.25 \text{ h}$	185 ± 18	1.64 ± 0.09
$t_n = 1.5 \text{ h}$	112 ± 11	1.71 ± 0.10
$t_n = 4 \text{ h}$	107 ± 11	1.71 ± 0.09
$t_n = 10 \text{ h}$	108 ± 20	1.80 ± 0.17
<u>$V_f = 0.70$</u>		
$t_n = 0.25 \text{ h}$	194 ± 14	1.68 ± 0.09
$t_n = 1.5 \text{ h}$	162 ± 19	2.15 ± 0.16
$t_n = 4 \text{ h}$	145 ± 14	2.35 ± 0.12
$t_n = 10 \text{ h}$	116 ± 16	2.62 ± 0.19
<u>$V_f \approx 0.98$</u>		
$t_n = 0.25 \text{ h}$	209 ± 21	1.72 ± 0.08
$t_n = 1.5 \text{ h}$	166 ± 16	2.18 ± 0.10
$t_n = 4 \text{ h}$	147 ± 18	2.49 ± 0.17
$t_n = 10 \text{ h}$	123 ± 15	2.73 ± 0.12
$t_n = 100 \text{ h}$	75 ± 8	3.27 ± 0.07

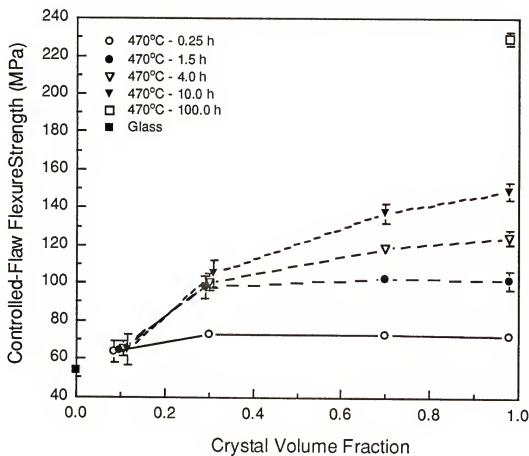


Figure 4.22. Effect of crystallization on the controlled-flaw flexure strength of lithia disilicate glass-ceramics. The indenter load was 14.7 N. The error bars represent 95% confidence intervals.

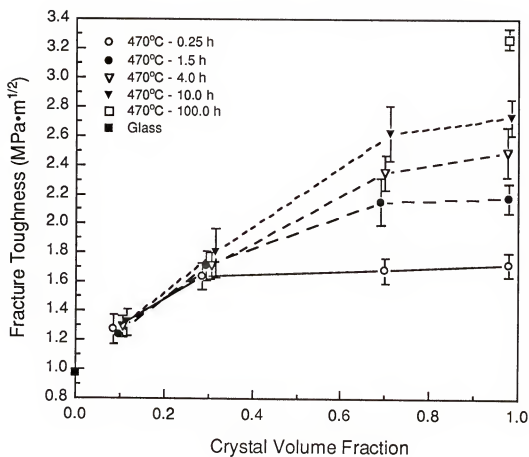


Figure 4.23. Effect of crystallization on fracture toughness, determined by quantitative fractography, for lithia disilicate glass-ceramics. The error bars represent 95% confidence intervals.

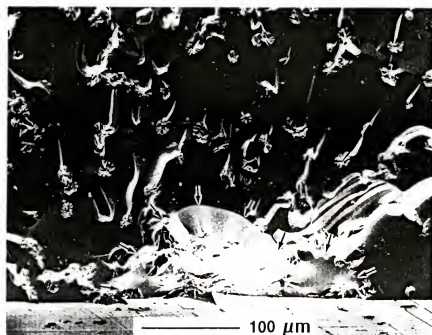


Figure 4.24. SEM micrograph of a lithia disilicate glass-ceramic fracture surface with $V_f = 0.10$. (Nucleation treatment: $470^{\circ}\text{C} / 10 \text{ h}$; crystal growth treatment: $600^{\circ}\text{C} / 6 \text{ min}$) The critical flaw is indicated by arrows. The critical flaw size of this specimen is $113 \mu\text{m}$.

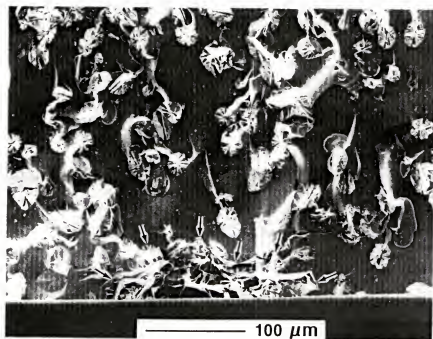


Figure 4.25. SEM micrograph of a lithia disilicate glass-ceramic fracture surface with $V_f = 0.30$. (Nucleation treatment: $470^{\circ}\text{C} / 10 \text{ h}$; crystal growth treatment: $600^{\circ}\text{C} / 9.5 \text{ min}$) The critical flaw is indicated by arrows. The critical flaw size of this specimen is $78 \mu\text{m}$

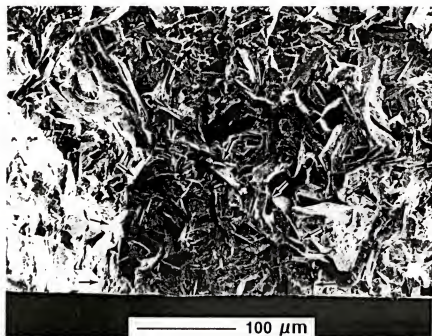


Figure 4.26. SEM micrograph of a lithia disilicate glass-ceramic fracture surface with $V_f \approx 0.98$. (Nucleation treatment: 470°C / 10 h; crystal growth treatment: 600°C / 6 min) The critical flaw is indicated by arrows. The critical flaw size of this specimen is 108 μm . The fracture surfaces of specimens with $V_f \approx 0.98$ are very similar in appearance to specimens with $V_f \approx 0.70$.

Analysis of the fracture toughness data (fractography method) by a Tukey's Studentized Range test showed a statistically significant difference ($P \leq 0.05$) in the mean toughness values of specimens with $V_f = 0.10$ and of specimens with $V_f = 0.30, 0.70$ and 0.98 for each of the four nucleation times. For a nucleation time of 0.25 h, there was no statistically significant difference ($P > 0.05$) between the mean toughness of specimens with $V_f = 0.30, 0.70$ or 0.98 . For each of the nucleation times, $1.5, 4$ and 10 h, there was a statistically significant difference ($P \leq 0.05$) between the mean toughness of specimens with $V_f = 0.30$ and the specimens with $V_f = 0.70$ and 0.98 . For the same nucleation times, there was no statistically significant difference ($P > 0.05$) between the mean toughness of specimens with $V_f = 0.70$ and $V_f \approx 0.98$. The mean fracture toughness of glass specimens and specimens with $V_f \approx 0.98$ that were nucleated for 100 h was significantly different ($P \leq 0.05$) from the mean toughness of all other specimen types. The results of the statistical analysis of the fracture toughness values, determined by the fractography method, is summarized in Table 4.6.

4.3.2 Fracture Toughness Determined by the Controlled-Flaw Flexure Strength Method

The mean fracture toughness determined by the controlled-flaw flexure strength method ranged from $1.01 \text{ MPa}\cdot\text{m}^{1/2}$ for lithia disilicate glass to $3.02 \text{ MPa}\cdot\text{m}^{1/2}$ for lithia disilicate glass-ceramic with $V_f = 0.98$ that was nucleated for 100 h. The mean fracture toughness values and 95% confidence intervals, determined by this technique, are listed in Table 4.7 and plotted as a function of crystal volume fraction in Figure 4.27. The differences in the fracture toughness values determined by each experimental technique are discussed in Chapter 5.

Table 4.6

Statistical Subsets of Mean Fracture Toughness Values (Determined by the Quantitative Fractography Method) for $\text{Li}_2\text{O} \cdot 2\text{SiO}_2$ Glass-Ceramics (Group means with the same letter are not significantly different.)

Crystal Volume Fraction, V_f	Fracture Toughness, K_{IC} ($\text{MPa} \cdot \text{m}^{1/2}$)	Tukey Grouping
Glass	0.97 ± 0.03	A
<u>$V_f = 0.10$</u>		
$t_n = 0.25$ h	1.27 ± 0.10	B
$t_n = 1.5$ h	1.24 ± 0.04	B
$t_n = 4$ h	1.29 ± 0.07	B
$t_n = 10$ h	1.32 ± 0.09	B
<u>$V_f = 0.30$</u>		
$t_n = 0.25$ h	1.64 ± 0.09	C
$t_n = 1.5$ h	1.71 ± 0.10	C
$t_n = 4$ h	1.71 ± 0.09	C
$t_n = 10$ h	1.80 ± 0.17	C
<u>$V_f = 0.70$</u>		
$t_n = 0.25$ h	1.68 ± 0.09	C
$t_n = 1.5$ h	2.15 ± 0.16	D
$t_n = 4$ h	2.35 ± 0.12	D E
$t_n = 10$ h	2.62 ± 0.19	E F
<u>$V_f = 0.98$</u>		
$t_n = 0.25$ h	1.72 ± 0.08	C
$t_n = 1.5$ h	2.18 ± 0.10	D
$t_n = 4$ h	2.49 ± 0.17	E F
$t_n = 10$ h	2.73 ± 0.12	F
$t_n = 100$ h	3.27 ± 0.07	G

Table 4.7

Mean Fracture Toughness (Determined by the Controlled-Flaw Flexure Strength Method) and Mean Controlled-Flaw Flexure Strength (Indentation Load of 14.7 N), and 95% Confidence Intervals for $\text{Li}_2\text{O} \cdot 2\text{SiO}_2$ Glass-Ceramics

Crystal Volume Fraction, V_f	Controlled-Flaw Strength, σ_f (MPa)	Fracture Toughness, K_{IC} (MPa·m ^{1/2})
Glass	53.7 ± 2.2	1.01 ± 0.03
<u>$V_f = 0.10$</u>		
$t_n = 0.25$ h	63.4 ± 5.8	1.18 ± 0.07
$t_n = 1.5$ h	64.2 ± 3.1	1.20 ± 0.02
$t_n = 4$ h	65.1 ± 3.9	1.21 ± 0.03
$t_n = 10$ h	64.5 ± 8.1	1.20 ± 0.09
<u>$V_f = 0.30$</u>		
$t_n = 0.25$ h	72.9 ± 2.9	1.30 ± 0.03
$t_n = 1.5$ h	97.8 ± 6.1	1.62 ± 0.07
$t_n = 4$ h	100.4 ± 4.4	1.65 ± 0.04
$t_n = 10$ h	104.8 ± 7.6	1.71 ± 0.08
<u>$V_f = 0.70$</u>		
$t_n = 0.25$ h	73.0 ± 2.8	1.30 ± 0.03
$t_n = 1.5$ h	102.4 ± 2.2	1.67 ± 0.03
$t_n = 4$ h	118.2 ± 2.6	1.87 ± 0.03
$t_n = 10$ h	137.2 ± 5.3	2.08 ± 0.06
<u>$V_f = 0.98$</u>		
$t_n = 0.25$ h	71.9 ± 1.3	1.30 ± 0.01
$t_n = 1.5$ h	102.7 ± 4.7	1.68 ± 0.05
$t_n = 4$ h	124.4 ± 4.0	1.96 ± 0.03
$t_n = 10$ h	149.0 ± 4.7	2.24 ± 0.05
$t_n = 100$ h	229.5 ± 3.5	3.02 ± 0.04

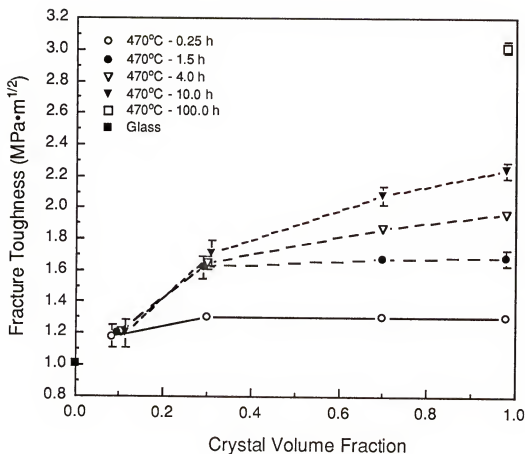


Figure 4.27. Effect of crystallization on fracture toughness, determined by the controlled-flaw flexure strength method, for lithia disilicate glass-ceramics. The error bars represent 95% confidence intervals.

Analysis of the fracture toughness data (determined by the controlled-flaw flexure strength method) by the Tukey's Studentized Range test showed a statistically significant difference ($P \leq 0.05$) between the mean toughness values of specimens with $V_f = 0.10$ and the mean toughness values for specimens with $V_f = 0.30, 0.70$ and 0.98 for each of the four nucleation times. For each of the two nucleation times, 0.25 and 1.5 h, there was no statistically significant difference ($P > 0.05$) between the mean toughness of specimens with $V_f = 0.30, 0.70$ or 0.98 . For each of the two nucleation times, 4 and 10 h, there was a statistically significant difference ($P \leq 0.05$) between the mean toughness of specimens with $V_f = 0.30$, the mean toughness of specimens with $V_f = 0.70$ and the mean toughness of specimens with $V_f \approx 0.98$. The mean fracture toughness of glass specimens and specimens with $V_f \approx 0.98$ that were nucleated for 100 h was significantly different ($P \leq 0.05$) from the mean toughness of all other specimen types. The results of statistical analysis of the fracture toughness values, determined by the controlled-flaw method, is summarized in Table 4.8.

4.4 Finite Element Stress Analysis

For lithia disilicate glass-ceramics, where $\alpha_m > \alpha_p$, where m and p indicate the matrix and particle phases, radial stresses in the matrix phase are compressive and tangential stresses are tensile. The maximum radial stresses estimated using finite element analysis ranged from 65 MPa adjacent to a single spherical particle to 141 MPa adjacent to a single elliptical particle with an aspect ratio of 2.0 . The maximum tangential tensile stress ranged from 32 MPa adjacent to a single spherical particle to 70 MPa for tangential stress adjacent to a single elliptical particle with an aspect ratio of 2.0 . The maximum

Table 4.8

Statistical Subsets of Mean Fracture Toughness Values (Determined by the Controlled-Flaw Flexure Strength Method) for $\text{Li}_2\text{O} \cdot 2\text{SiO}_2$ Glass-Ceramics (Group means with the same letter are not significantly different.)

Crystal Volume Fraction, V_f	Fracture Toughness, K_{IC} (MPa·m ^{1/2})	Tukey Grouping	
Glass	1.01 ± 0.03	A	
<u>$V_f = 0.10$</u>			
$t_n = 0.25$ h	1.18 ± 0.07	B	
$t_n = 1.5$ h	1.20 ± 0.02	B	
$t_n = 4$ h	1.21 ± 0.03	B	
$t_n = 10$ h	1.20 ± 0.09	B	
<u>$V_f = 0.30$</u>			
$t_n = 0.25$ h	1.30 ± 0.03	C	
$t_n = 1.5$ h	1.62 ± 0.07		D
$t_n = 4$ h	1.65 ± 0.04		D
$t_n = 10$ h	1.71 ± 0.08		D
<u>$V_f = 0.70$</u>			
$t_n = 0.25$ h	1.30 ± 0.03	C	
$t_n = 1.5$ h	1.67 ± 0.03		D
$t_n = 4$ h	1.87 ± 0.03		E
$t_n = 10$ h	2.08 ± 0.06		G
<u>$V_f = 0.98$</u>			
$t_n = 0.25$ h	1.30 ± 0.01	C	
$t_n = 1.5$ h	1.68 ± 0.05		D
$t_n = 4$ h	1.96 ± 0.03		F
$t_n = 10$ h	2.24 ± 0.05		H
$t_n = 100$ h	3.02 ± 0.04		I

radial and tangential stresses were located at the end of the major axis in all models. The maximum radial and tangential stresses for single crystal models are plotted as a function of the crystal aspect ratio (1.0 to 2.0) in Figure 4.28. The radial stresses computed for the two crystal models increased from 61 MPa adjacent to each spherical crystal when the distance between the crystals was set at $2R$, where R is the crystal radius, to 317 MPa adjacent to each spherical crystal when the distance between the particles was decreased to $0.002R$. The tangential stresses estimated in the two crystal models increased from 32 MPa adjacent to each spherical crystal when the distance between the crystals was set at $2R$, where R is the crystal radius, to 276 MPa adjacent to each spherical crystal when the distance between the particles was set at $0.002R$. The radial and tangential stresses are plotted as a function of crystal spacing ($0.002R$ to $2.0R$) in Figure 4.29.

4.5 Microcrack Density

Values of microcrack density, determined by quantitative stereology, ranged from $0 \text{ mm}^2/\text{mm}^3$ for lithia disilicate glass-ceramic that was nucleated for 10 h with $V_f = 0.10$ to $94.1 \text{ mm}^2/\text{mm}^3$ for lithia disilicate glass-ceramic that was nucleated for 0.25 h with $V_f = 0.98$. The mean microcrack density values and 95% confidence intervals of lithia disilicate glass-ceramics are listed in Table 4.9, and are plotted as a function of crystal volume fraction in Figure 4.30.

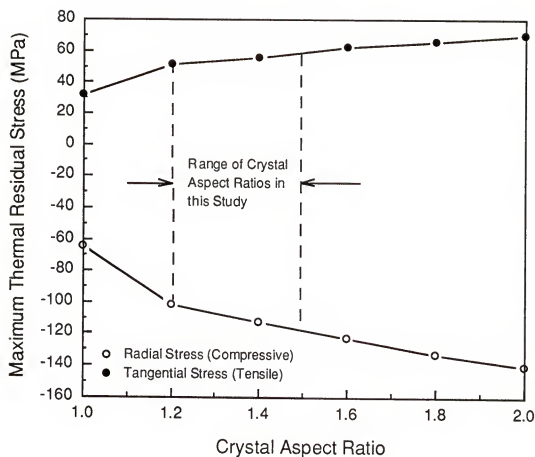


Figure 4.28. Calculated effect of crystal aspect ratio on radial and tangential stresses that are created by thermal expansion mismatch between the crystal and glass matrix phases. The range of crystal aspect ratios (Table 4.1) is indicated by the dashed lines.

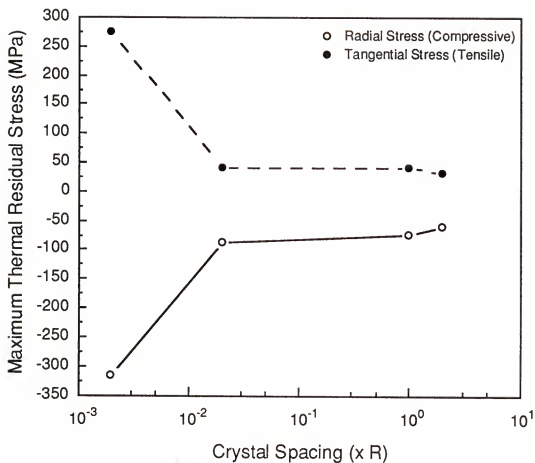


Figure 4.29. Calculated effect of crystal spacing on radial and tangential stresses that are created by thermal expansion mismatch between the crystal and glass matrix phases. Spacing is given in units of crystal radius (R). The two crystals have equal radii.

Table 4.9

Mean Microcrack Density with 95% Confidence Intervals
for $\text{Li}_2\text{O} \cdot 2\text{SiO}_2$ Glass-Ceramics

Crystal Volume Fraction, V_f	Microcrack Density, $(S_v)_{mc}$ (cm^2/cm^3)
<u>$V_f = 0.10$</u>	
$t_n = 0.25 \text{ h}$	3.5 ± 1.2
$t_n = 1.5 \text{ h}$	1.2 ± 0.7
$t_n = 4 \text{ h}$	0.2 ± 0.3
$t_n = 10 \text{ h}$	0.0 ± 0.0
<u>$V_f = 0.30$</u>	
$t_n = 0.25 \text{ h}$	29.2 ± 3.1
$t_n = 1.5 \text{ h}$	16.6 ± 2.2
$t_n = 4 \text{ h}$	10.9 ± 2.5
$t_n = 10 \text{ h}$	5.0 ± 1.1
<u>$V_f = 0.70$</u>	
$t_n = 0.25 \text{ h}$	67.7 ± 3.6
$t_n = 1.5 \text{ h}$	52.1 ± 4.7
$t_n = 4 \text{ h}$	40.0 ± 2.5
$t_n = 10 \text{ h}$	33.0 ± 2.6
<u>$V_f = 0.98$</u>	
$t_n = 0.25 \text{ h}$	94.1 ± 4.3
$t_n = 1.5 \text{ h}$	67.5 ± 3.4
$t_n = 4 \text{ h}$	56.4 ± 5.8
$t_n = 10 \text{ h}$	44.0 ± 5.4
$t_n = 100 \text{ h}$	4.3 ± 2.4

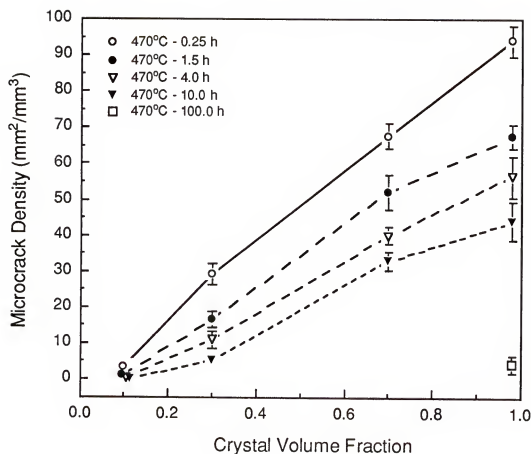


Figure 4.30. Effect of crystallization on the microcrack density of lithia disilicate glass-ceramics. The error bars represent 95% confidence intervals.

4.6 Fractal Dimension

4.6.1 Fractal Dimension Determined by the Slit Island Technique

The fractal dimensional increment values determined by the modified slit island method, $D^*(MSI)$, ranged from 0.10 for lithia disilicate glass to 0.24 for lithia disilicate glass-ceramic that was nucleated for 100 h ($V_f = 0.98$). Listed in Table 4.10 are the mean fractal dimensional increment values and 95% confidence intervals for lithia disilicate glass and lithia disilicate glass-ceramics that were nucleated for 0.25 h and 10 h ($V_f = 0.10, 0.30, 0.70$ and 0.98), and nucleated for 100 h ($V_f \approx 0.98$). $D^*(MSI)$ values are also plotted as a function of crystal volume fraction in Figure 4.31.

4.6.2 Fractal Dimension Determined by the Atomic Force Microscopy Box Counting Technique

The fractal dimensional increment values, $D^*(AFM)$, of lithia disilicate glass-ceramics, determined using the atomic force microscopy method ranged from 0.09 for lithia disilicate glass to 0.23 for lithia disilicate glass-ceramic with $V_f \approx 0.98$ that was nucleated for 100 h. The mean fractal dimensional increment values and 95% confidence intervals of lithia disilicate glass and lithia disilicate glass-ceramics are listed in Table 4.10, and are plotted as a function of crystal volume fraction in Figure 4.32. A statistically significant difference ($P \leq 0.05$) in the fractal dimensional increment for the glass and crystal phases in specimens with $V_f = 0.10$ and 0.30 was also observed using the AFM method. The mean fractal dimensional increments and 95% confidence intervals for the glass and crystal phases were 0.09 ± 0.01 and 0.23 ± 0.01 , respectively. Analysis of this data by ANOVA showed a statistically significant difference ($P \leq 0.05$) between

the mean fractal dimensional increments of the two phases. Statistical analysis of the glass-ceramic fractal dimensional increment data (determined by the AFM method) by a Tukey's Studentized Range test is summarized in Table 4.11

Table 4.10

Mean Fractal Dimensional Increment and 95% Confidence Interval
for $\text{Li}_2\text{O} \cdot 2\text{SiO}_2$ Glass-Ceramics

Crystal Volume Fraction, V_f	$D^*(\text{MSI})$	$D^*(\text{AFM})$
Glass	0.10 ± 0.00	0.09 ± 0.01
<u>$V_f = 0.10$</u>		
$t_n = 0.25 \text{ h}$	0.11 ± 0.00	0.11 ± 0.02
$t_n = 1.5 \text{ h}$	-	0.12 ± 0.01
$t_n = 4 \text{ h}$	-	0.12 ± 0.02
$t_n = 10 \text{ h}$	0.13 ± 0.01	0.12 ± 0.02
<u>$V_f = 0.30$</u>		
$t_n = 0.25 \text{ h}$	0.14 ± 0.00	0.14 ± 0.01
$t_n = 1.5 \text{ h}$	-	0.14 ± 0.02
$t_n = 4 \text{ h}$	-	0.14 ± 0.01
$t_n = 10 \text{ h}$	0.14 ± 0.00	0.14 ± 0.01
<u>$V_f = 0.70$</u>		
$t_n = 0.25 \text{ h}$	0.17 ± 0.00	0.17 ± 0.01
$t_n = 1.5 \text{ h}$	-	0.17 ± 0.02
$t_n = 4 \text{ h}$	-	0.18 ± 0.01
$t_n = 10 \text{ h}$	0.18 ± 0.00	0.18 ± 0.01
<u>$V_f = 0.98$</u>		
$t_n = 0.25 \text{ h}$	0.19 ± 0.00	0.19 ± 0.01
$t_n = 1.5 \text{ h}$	-	0.20 ± 0.01
$t_n = 4 \text{ h}$	-	0.22 ± 0.01
$t_n = 10 \text{ h}$	0.23 ± 0.00	0.23 ± 0.01
$t_n = 100 \text{ h}$	0.24 ± 0.01	0.23 ± 0.01

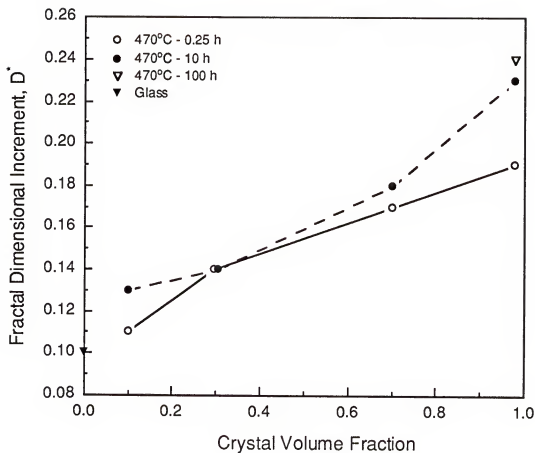


Figure 4.31. Effect of crystallization on the fractal dimensional increment of lithia disilicate glass-ceramics. The modified slit island technique was used for measurement of D^* . The 95% confidence intervals are smaller than the symbols and are not shown.

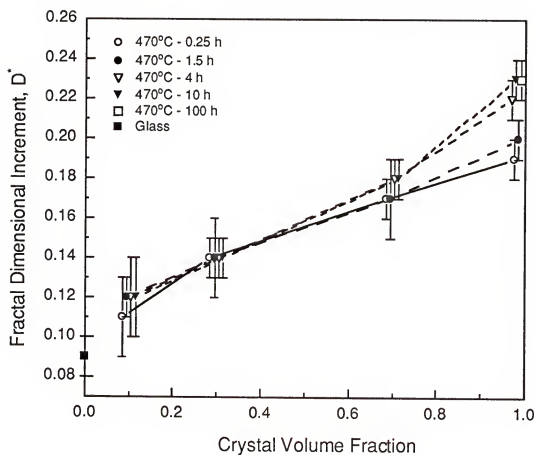


Figure 4.32. Effect of crystallization on the fractal dimensional increment of lithia disilicate glass-ceramics. The atomic force microscopy box counting method was used for measurement of D^* . The error bars represent 95% confidence intervals.

Table 4.11
Statistical Subsets of Mean Fractal Dimensional Increment Values
(Determined by the AFM Method) for $\text{Li}_2\text{O} \cdot 2\text{SiO}_2$ Glass-Ceramics
(Group means with the same letter are not significantly different.)

Crystal Volume Fraction, V_f	D^* (AFM)	Tukey Grouping
Glass	0.09 ± 0.01	A
<u>$V_f = 0.10$</u>		
$t_n = 0.25$ h	0.11 ± 0.02	A B
$t_n = 1.5$ h	0.12 ± 0.01	B C
$t_n = 4$ h	0.12 ± 0.02	B C D
$t_n = 10$ h	0.12 ± 0.02	B C D E
<u>$V_f = 0.30$</u>		
$t_n = 0.25$ h	0.14 ± 0.01	C D E
$t_n = 1.5$ h	0.14 ± 0.02	D E
$t_n = 4$ h	0.14 ± 0.01	D E
$t_n = 10$ h	0.14 ± 0.01	E
<u>$V_f = 0.70$</u>		
$t_n = 0.25$ h	0.17 ± 0.01	F
$t_n = 1.5$ h	0.17 ± 0.02	F
$t_n = 4$ h	0.18 ± 0.01	F G
$t_n = 10$ h	0.18 ± 0.01	F G
<u>$V_f = 0.98$</u>		
$t_n = 0.25$ h	0.19 ± 0.01	F G
$t_n = 1.5$ h	0.20 ± 0.01	G H
$t_n = 4$ h	0.22 ± 0.01	H I
$t_n = 10$ h	0.23 ± 0.01	I
$t_n = 100$ h	0.23 ± 0.01	I

CHAPTER 5 DISCUSSION

5.1 Microstructure

The spherulitic crystal morphology of lithia disilicate glass-ceramics produced in this study is consistent with the previous findings of Freiman (1968), Freiman and Hench (1968; 1972), Parsell (1993), and Naman (1994). Spherulites are composed of fibrous crystals radiating from a common center, and in general have a spherical geometry. The occurrence of spherulite formation in glass-ceramic materials is not uncommon and is generally associated with glass-ceramics having relatively poor fracture resistance ($K_{IC} \leq 1.5 \text{ MPa}\cdot\text{m}^{1/2}$) (Strnad, 1986). Lithia silicate, baria silicate and sodium phosphate glasses, among others, can display spherulitic structures when crystallized. Investigations have shown that crystallographic orientation is not maintained in the fibrous structure of spherulites (McMillan, 1979). The microstructure can therefore be treated as isotropic relative to physical properties.

The average crystal size of the lithia disilicate glass-ceramic specimens increased with decreasing nucleation time for each crystal volume fraction studied (Figure 5.1). In general, the spherulitic crystals of specimens were elliptical in shape. The mean crystal aspect ratio (major axis/minor axis) of specimens analyzed in this study ranged from 1.20 ($t_n = 10 \text{ h}$, $V_f = 0.70$) to 1.48

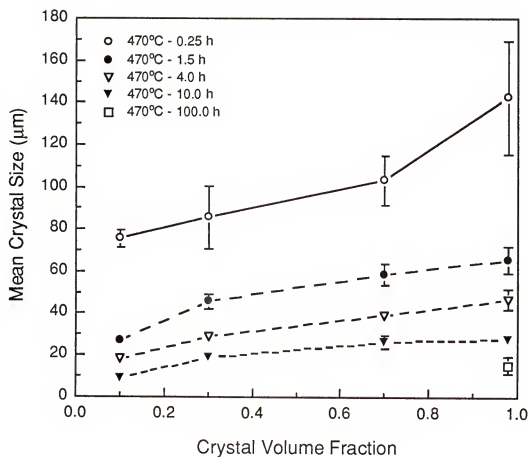


Figure 5.1. Effect of crystallization on the mean crystal size of lithia disilicate glass-ceramics. Temperature and time indicate the nucleation temperature and nucleation time. Each line represents a constant nuclei density for glass-ceramics at each crystal volume fraction. The error bars represent 95% confidence intervals.

($t_n = 10$ h, $V_f = 0.10$). There was no apparent relationship between nucleation time and crystal aspect ratio.

An interesting phenomenon observed in the specimens with $V_f \approx 0.98$ is the presence of internal porosity. This porosity can be seen in the scanning electron micrograph of a lithia disilicate glass-ceramic specimen ($t_n = 100$ h, $V_f \approx 0.98$) shown in Figure 5.2. Void formation during crystallization has been reported previously for lithia disilicate glass-ceramics (Naman, 1994) and for calcium phosphate glass-ceramics (Watanabe *et al.*, 1986; Watanabe *et al.*, 1989). Watanabe *et al.* (1986) attributed the formation of voids to the difference in density between the parent glass and the resulting glass-ceramic. If the apparent volume of the glass does not change during crystallization, the void volume should correspond to this density difference. There is a difference of approximately 5% between the density of lithia disilicate glass ($\rho = 2.32$ g/cc) and the density of crystalline lithia disilicate ($\rho = 2.44$ g/cc). The volume fraction of voids present in the lithia disilicate glass-ceramics of this study varied between approximately 0.02 ($t_n = 100$ h, $V_f \approx 0.98$; $t_n = 10$ h, $V_f \approx 0.98$) and 0.04 ($t_n = 0.25$ h, $V_f \approx 0.98$). The fractional difference between the density of lithia disilicate glass and the density of crystalline lithia disilicate, 0.05, is similar to the volume fraction of voids measured for lithia disilicate glass-ceramics with $V_f \approx 0.98$.

5.2 Physical Properties

5.2.1 Glass transition Temperature of Lithia Disilicate Glass

Thermal analysis of the lithia disilicate glass used in this study indicated a glass transition temperature in the range between approximately 450°C and

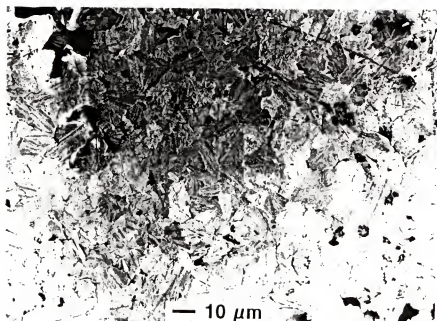


Figure 5.2. SEM micrograph showing void formation in a lithia disilicate glass-ceramic with $V_f \approx 0.98$. (Nucleation treatment: 470°C / 100 h; crystallization treatment: 600°C / 12 min)

480°C. This temperature range is consistent with the glass transition temperatures reported previously for lithia disilicate glass. Freiman (1968) and Freiman and Hench (1968) reported that the optimal nucleation temperature, that corresponds to the glass transition temperature, for lithia disilicate glass was 475°C. Marotta *et al.* (1982) and Ray and Day (1990) reported glass transition temperatures of 455°C and 453°C, respectively. Parsell (1993) and Naman (1994) reported glass transition temperature ranges of 450°C to 480°C. The glass transition temperature range measured for the lithia disilicate glass in this study suggests that the temperature and time used to anneal specimens after polishing (450°C, 2 h) was adequate to relieve polishing induced residual stresses.

5.2.2 Thermal Expansion of Lithia Disilicate Glass-Ceramics

The mean coefficient of thermal expansion (CTE) of lithia disilicate glass-ceramics decreased with increasing crystal volume fraction. The CTE decreased from $12.8 \times 10^{-6}/^{\circ}\text{C}$ for lithia disilicate glass to $9.2 \times 10^{-6}/^{\circ}\text{C}$ for lithia disilicate glass-ceramic with $V_f \approx 0.98$ ($t_n = 0.25$ h). These values are similar to the values reported previously by Freiman (1968) and Naman (1994). Freiman reported a CTE of $12.5 \times 10^{-6}/^{\circ}\text{C}$ for lithia disilicate glass and a CTE of $10.0 \times 10^{-6}/^{\circ}\text{C}$ for lithia disilicate with $V_f \approx 0.98$. Naman reported a CTE of $12.2 \times 10^{-6}/^{\circ}\text{C}$ for lithia disilicate glass and a CTE of $10.9 \times 10^{-6}/^{\circ}\text{C}$ for lithia disilicate with $V_f \approx 0.98$. The CTE data from this study, along with the data of Freiman and Naman, are plotted as a function of crystal volume fraction in Figure 5.3. Variation of the CTE data from a simple rule of mixtures relationship ($\alpha_{\text{glass-ceramic}} = V_{\text{fglass}} \cdot \alpha_{\text{glass}} + V_{\text{fcrystal}} \cdot \alpha_{\text{crystal}}$) for specimens with $t_n = 0.25$ h and $t_n = 10$ h is attributed to the presence of microcracks. In general, glass-ceramics free of

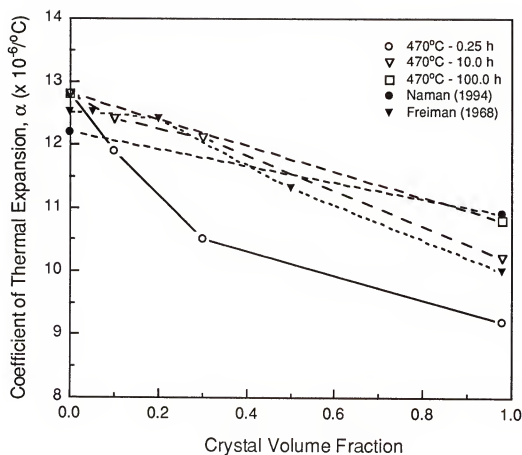


Figure 5.3. Effect of crystallization on the coefficient of thermal expansion (CTE) of lithia disilicate glass-ceramics. The CTE data of Freiman (1968) and Naman (1994) for lithia disilicate glass-ceramics are also plotted. The CTE data of the current study is consistent with the findings of the other studies.

microstructural defects, *i.e.*, voids, microcracks, etc., are expected to follow a rule of mixtures relationship for CTE (McMillan, 1979).

In addition to the variation of CTE with V_f , the CTE of lithia disilicate glass-ceramics with $V_f \approx 0.98$ decreased with decreasing nucleation time and the corresponding increase in average crystal size. The CTE ($V_f \approx 0.98$) decreased from $10.8 \times 10^{-6}/^{\circ}\text{C}$ for $t_n = 100$ h to $9.2 \times 10^{-6}/^{\circ}\text{C}$ for $t_n = 0.25$ h. The only observed microstructural difference other than crystal size between these specimens is the presence of microcracks in the specimens with $t_n = 0.25$ h. Therefore, the decrease in CTE ($V_f \approx 0.98$) is attributed to the presence of microcracks. The CTE of lithia disilicate glass-ceramics with $V_f \approx 0.98$ is plotted as a function of average crystal size in Figure 5.4.

5.2.3 Density of Lithia Disilicate Glass-Ceramics

The bulk density of lithia disilicate specimens ranged from 2.32 g/cc for glass to 2.39 g/cc for specimens with $V_f \approx 0.98$ ($t_n = 100$ h). The true density, of the same specimens ground into powder, ranged from 2.32 g/cc for glass to 2.44 g/cc for specimens with $V_f \approx 0.98$ ($t_n = 10$ h; $t_n = 100$ h). The difference in the true density of lithia disilicate glass and fully crystalline lithia disilicate ($V_f \approx 0.98$) is approximately 4%. This difference is believed to be responsible for the formation of closed, bulk porosity during crystallization that was described earlier. Deviation from a rule of mixtures relationship between the density of glass-ceramic specimens and crystal volume fraction is attributed to the presence of this closed, bulk porosity. The densities of lithia disilicate specimens in this study were consistent with values reported by other investigators. Freiman and Hench (1972) reported a density of 2.33 g/cc for lithia disilicate glass and 2.40 for lithia disilicate glass-ceramic with $V_f = 0.65$.

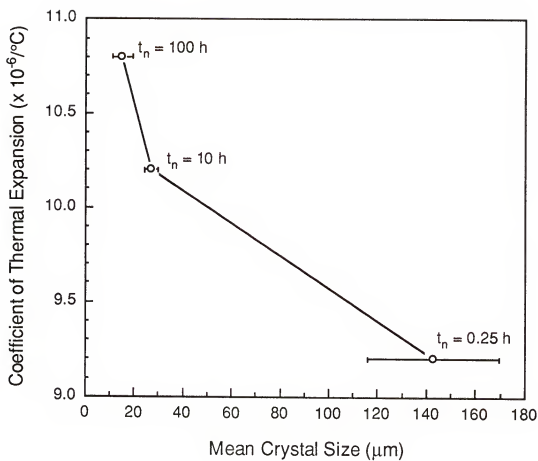


Figure 5.4. Effect of crystal size on the coefficient of thermal expansion of lithia disilicate glass-ceramics with $V_f \approx 0.98$. The error bars represent 95% confidence intervals.

Naman reported a density of 2.32 g/cc for lithia disilicate glass and 2.42 g/cc for lithia disilicate glass-ceramic with $V_f = 0.98$.

The difference in the bulk density and true density values reported in this study can be explained by the internal porosity present in the specimens with $V_f \geq 0.70$. If the true densities of specimens with $V_f \approx 0.98$ are corrected to account for the measured volume fraction of porosity, they are approximately equal to the measured bulk densities. This correction is shown graphically in Figure 5.5. The slight difference in the true density of the lithia disilicate specimens ($V_f \approx 0.98$) produced with different heat-treatment schedules could be a result of greater volume fractions of residual glass in the specimens heat-treated with shorter nucleation times. The smaller nuclei densities that result from the shorter nucleation times, 0.25 and 1.5 h, could be responsible for less efficient overall crystallization in these specimens. This behavior was observed by Parsell (1993) who analyzed the effect of initial nuclei density on the bulk crystallization of lithia disilicate glass-ceramics.

5.2.4 Elastic Modulus of Lithia Disilicate Glass-Ceramics

The elastic modulus (E) of lithia disilicate glass-ceramics was found to increase with increasing crystal volume fraction except for the specimens that were nucleated for 0.25 h. These specimens ($t_n = 0.25$ h, $V_f = 0.10, 0.30, 0.70$, and ≈ 0.98) displayed no measurable increase in E with increasing V_f . The E values measured in this study varied slightly from values previously reported by Freiman (1968) and Naman (1994). For lithia disilicate glass, an E value of 70 GPa was measured in this study. Freiman reported a value of 52 GPa for lithia disilicate glass, and Naman reported a value of 80 GPa. For lithia disilicate glass-ceramic with $V_f \approx 0.98$, values ranging from 71 GPa ($t_n = 0.25$ h) to 137

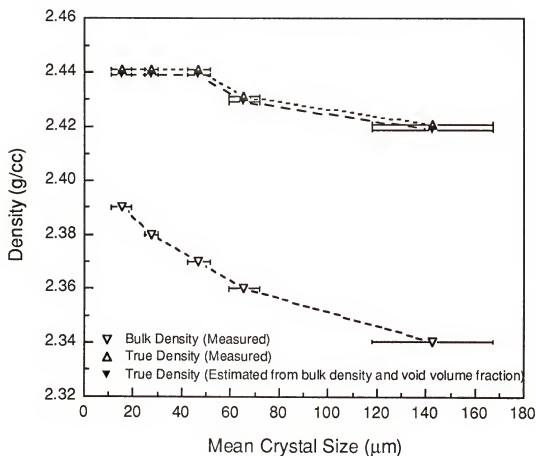


Figure 5.5. Graphical comparison of bulk and true densities of lithia disilicate glass-ceramics with $V_f \approx 0.98$. The true density, estimated from the bulk density corrected to account for the measured volume fraction of internal porosity, is also shown. The error bars represent 95% confidence intervals.

GPa ($t_n = 100$ h) were measured for specimens in this study. Freiman reported a value of 90 GPa for glass-ceramic with $V_f \geq 0.90$, and Naman reported a value of 88 GPa for glass-ceramic with $V_f \approx 0.98$.

Differences between the E values measured in this study and those reported previously could be a result of measurement error resulting from different measurement techniques. Freiman used a resonant frequency technique and Naman used an ultrasonic technique different from the one used in this study. However, each technique should produce the same result. Therefore, this explanation is discounted. The differences in the E values are more likely a result of microstructural variations produced during fabrication, *i.e.*, pores, impurities, etc., between specimens analyzed in the different studies. Although specimen preparation in each study is very similar, the microstructures of lithia disilicate glass-ceramics are very sensitive to composition and heat treatment time and temperature. As a result, even slight deviations in composition and/or heat treatment can cause microstructural changes that could affect properties such as elastic modulus. The E values measured in this study, along with the E values reported by Freiman and Naman, are plotted as a function of crystal volume fraction in Figure 5.6.

Another explanation for the differences in E values measured in this study and those reported previously is the presence and severity of microcracks in specimens. Both Freiman and Naman reported the presence of microcracks in lithia disilicate glass-ceramic specimens, although neither investigator quantitatively measured the microcrack density. Several previous investigators (Hasselman and Fulrath, 1965; Budiansky and O'Connell, 1976; Case *et al.*, 1983; Case 1984; Käse *et al.*, 1985; Venkateswaran *et al.*, 1988) have reported the large decrease in E, relative to a nonmicrocracked material, produced by the presence of microcracks. Decreases of up to 90% have been reported

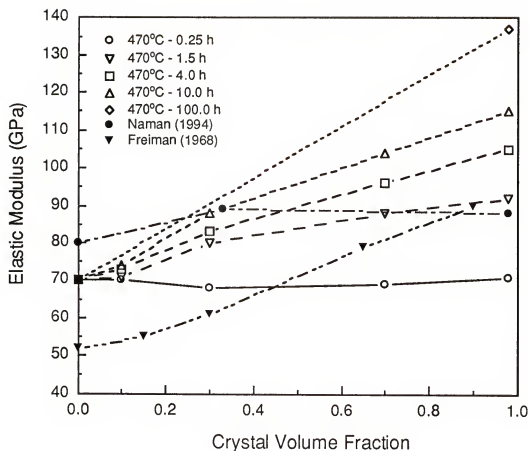


Figure 5.6. Effect of crystallization on the elastic modulus (E) of lithia disilicate glass-ceramics. The E data of Freiman (1968) and Naman (1994) for lithia disilicate glass-ceramics are also plotted. Differences in E values reported by the different investigators are attributed to different measurement techniques and to the presence and magnitude of microcracks in the specimens used in the different studies.

(Case, 1984). The large differences in the E values measured in this study for lithia disilicate specimens with $V_f \geq 0.70$ can be attributed to microcracking. The microcrack density increased with increasing crystal size for specimens analyzed in this study. The relationship between crystal size and microcrack density will be discussed in detail in a subsequent section. It should also be noted that deviation from a rule of mixtures relationship between the elastic modulus of glass-ceramic specimens and crystal volume fraction is attributed to the presence of microcracks.

The relationship between elastic modulus and mean crystal size is shown in Figure 5.7. At crystal volume fractions of 0.30, 0.70, and 0.98, E decreases substantially with increasing mean crystal size. For $V_f = 0.30$, E decreases from 88 GPa (mean crystal size = 18.6 μm , $t_n = 10$ h) to 68 GPa (mean crystal size = 85.6 ± 14.8 μm , $t_n = 0.25$ h). For $V_f = 0.70$, E decreases from 104 GPa (mean crystal size = 26.3 ± 3.0 μm , $t_n = 10$ h) to 69 GPa (mean crystal size = 103.3 ± 11.6 μm , $t_n = 0.25$ h). For $V_f \approx 0.98$, E decreases from 137 GPa (mean crystal size = 15.2 μm , $t_n = 100$ h) to 71 GPa (mean crystal size = 142.6 μm , $t_n = 0.25$ h). This corresponds to a decrease of 29% for $V_f = 0.30$, 51% for $V_f = 0.70$, and 93% for $V_f \approx 0.98$. The observed decreases in E , that are attributed to microcracking in the specimens of this study, are reasonable when compared to other previously mentioned experimental results for nonmicrocracked and microcracked brittle materials.

A remaining factor that could have an effect on the elastic modulus of lithia disilicate glass-ceramics is the presence of closed porosity. As noted previously, the specimens with $V_f \approx 0.98$ contained internal porosity. The volume fraction of porosity ranged from 0.02 ($t_n = 4$ h, 10 h, 100 h) to 0.04 ($t_n = 0.25$ h, 1.5 h). The effect of porosity on E can be estimated using the following expression developed by J.K. MacKenzie (Kingery *et al.*, 1976):

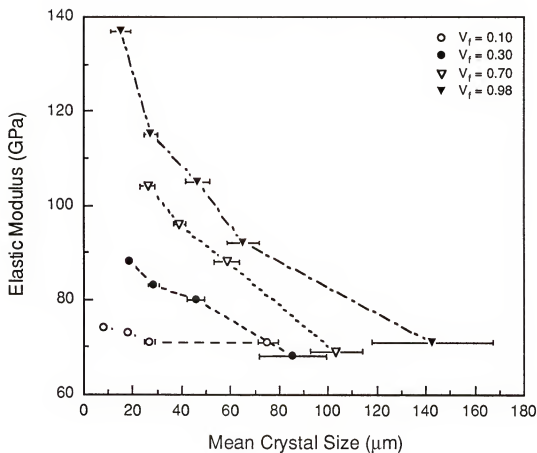


Figure 5.7. Effect of crystal size on the elastic modulus of lithia disilicate glass-ceramics. The error bars represent 95% confidence intervals.

$$E = E_0 (1 - 1.9P + 0.9P^2) \quad (5.1)$$

where E_0 is the elastic modulus of the material free of porosity and P is the volume fraction of porosity. Using this equation, the reduction in elastic modulus resulting from internal porosity would be between 4% ($P = 0.02$) and 7% ($P = 0.04$). The decrease in E observed experimentally greatly exceeds that estimated using equation (5.1). Thus, it is concluded that the closed porosity present in lithia disilicate glass-ceramics has a minimal effect on their elastic properties.

5.3 Relationship Between Fracture Toughness and Microstructure

5.3.1 Fracture Toughness of Lithia Disilicate Glass-Ceramics

Two techniques were used to determine the fracture toughness of specimens in this study: 1) the quantitative fractography method and 2) the controlled-flaw strength method. Each technique should yield the same value for fracture toughness. Statistical analysis showed that the fracture toughness, determined by the quantitative fractography method, of lithia disilicate glass-ceramics increased significantly with increasing crystal volume fraction, from $V_f = 0.10$ to $V_f = 0.70$, for specimens with nucleation times of 1.5 h, 4 h and 10 h, but did not increase from $V_f = 0.70$ to $V_f \approx 0.98$. For lithia disilicate glass-ceramics with a nucleation time of 0.25 h, the fracture toughness increased significantly from $V_f = 0.10$ to $V_f = 0.30$, but did not significantly increase between $V_f = 0.30$ and $V_f \approx 0.98$. The statistical analysis of mean fracture toughness, determined by the quantitative fractography method (Equation 3.18), that will be referred to as K_{IC} (fractography method), is summarized in Table 4.6

(p. 110). The mean values of K_{IC} (fractography method) are plotted as a function of crystal volume fraction in Figure 4.23 (p. 105).

Statistical analysis of the mean fracture toughness values, determined by the controlled-flaw flexure strength method, of lithia disilicate glass-ceramics indicated a significant increase in K_{IC} (controlled-flaw/strength method) with increasing crystal volume fraction, from $V_f = 0.10$ to $V_f \approx 0.98$, for specimens with nucleation times of 4 h and 10 h. For lithia disilicate glass-ceramics with nucleation times of 0.25 h and 1.5 h, the fracture toughness increased significantly from $V_f = 0.10$ to $V_f = 0.30$, but did not significantly increase between $V_f = 0.30$ and $V_f \approx 0.98$. The statistical analysis of mean K_{IC} (controlled-flaw/strength method) values is summarized in Table 4.8 (p. 114). Toughness values are plotted as a function of crystal volume fraction in Figure 4.27 (p. 112).

There are differences between the fracture toughness values, measured by the two methods, of specimens with $V_f \geq 0.70$ for $t_n = 1.5$ h, 4 h and 10 h, and for specimens with $V_f \geq 0.30$ for $t_n = 0.25$ h. These differences can be explained by the form of the fracture toughness relationship used to calculate K_{IC} (fractography method). An initial assumption was that residual stress would be present in the vicinity of the controlled flaw, *i.e.*, under the indentation site, in all specimens. Therefore, the relationship used to calculate K_{IC} , using the quantitative fractography method, was equation (3.18):

$$K_{IC} = 1.65\sigma_f(c)^{1/2}$$

where the 1.65 is the crack-geometry parameter, Y , derived by Cook and Lawn (1983) to account for residual stress in indented specimens. It is likely that this relationship yielded an overestimation of K_{IC} for many of the lithia disilicate

specimens in this study. The measurement discrepancies can be explained by the presence of microcracks in the specimens.

The formation of microcracks in a material can relieve residual stress (Ito *et al.*, 1981). If the microcracks present in the specimens that yielded the measurement differences relieved the residual stress in the vicinity of their controlled-flaws, equation (3.18) would not produce accurate calculations of fracture toughness. For specimens with negligible levels of residual stress, the proper relationship between fracture toughness and flaw size is given by equation (3.13):

$$K_{IC} = 1.24 \sigma_f (c)^{1/2}$$

where 1.24 is the crack-geometry parameter (Randall, 1967). If K_{IC} (fractography method) values of microcracked specimens are recalculated using equation (3.13), the K_{IC} (fractography method) values become very similar to the K_{IC} (controlled-flaw/strength method) values for the same specimens. This is shown graphically in Figures 5.8 through 5.11. The line in these plots represents K_{IC} (fractography method) = K_{IC} (controlled-flaw/strength method). From this point, all toughness values discussed will be K_{IC} (controlled-flaw/strength method) values. These will now be referred to simply as K_{IC} .

The fracture toughness values of lithia disilicate glass-ceramics generally decrease with increasing crystal size. The relationship between K_{IC} and mean crystal size is shown in Figure 5.12. For crystal volume fractions of 0.70 and 0.98, K_{IC} decreases significantly with increasing mean crystal size. For $V_f = 0.70$, K_{IC} decreases from $2.08 \pm 0.06 \text{ MPa}\cdot\text{m}^{1/2}$ (mean crystal size = $26.3 \pm 3.0 \text{ }\mu\text{m}$, $t_n = 10 \text{ h}$) to $1.30 \pm 0.03 \text{ MPa}\cdot\text{m}^{1/2}$ (mean crystal size = $103.3 \pm 11.6 \text{ }\mu\text{m}$, $t_n = 0.25 \text{ h}$). For $V_f = 0.98$, K_{IC} decreases from $3.02 \pm 0.04 \text{ MPa}\cdot\text{m}^{1/2}$ (mean crystal size = $15.2 \text{ }\mu\text{m}$, $t_n = 100 \text{ h}$) to $1.30 \pm 0.01 \text{ MPa}\cdot\text{m}^{1/2}$ (mean crystal size = 142.6

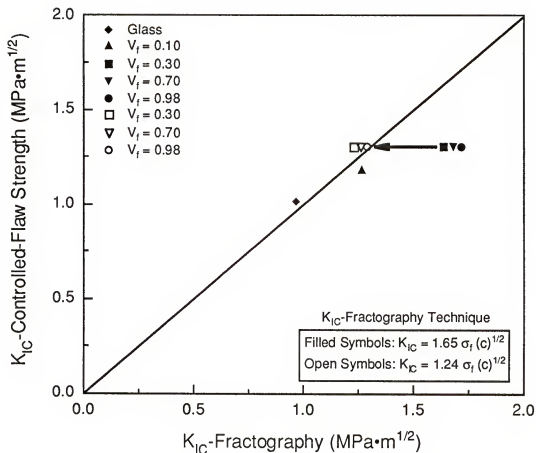


Figure 5.8. Relationship between mean fracture toughness values, calculated using the quantitative fractography method and the controlled-flaw strength method, of lithia disilicate glass-ceramics with $t_h = 0.25$ h. The line represents $K_{IC}\text{-Fractography} = K_{IC}\text{-Controlled-Flaw Strength}$. The arrow shows the residual stress correction in K_{IC} -Fractography resulting from the formation of microcracks.

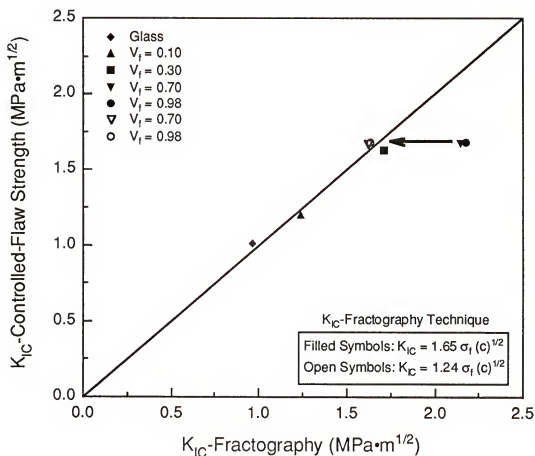


Figure 5.9. Relationship between mean fracture toughness values, calculated using the quantitative fractography method and the controlled-flaw strength method, of lithia disilicate glass-ceramics with $t_n = 1.5$ h. The line represents $K_{IC}\text{-Fractography} = K_{IC}\text{-Controlled-Flaw Strength}$. The arrow shows the residual stress correction in K_{IC} -Fractography resulting from the formation of microcracks.

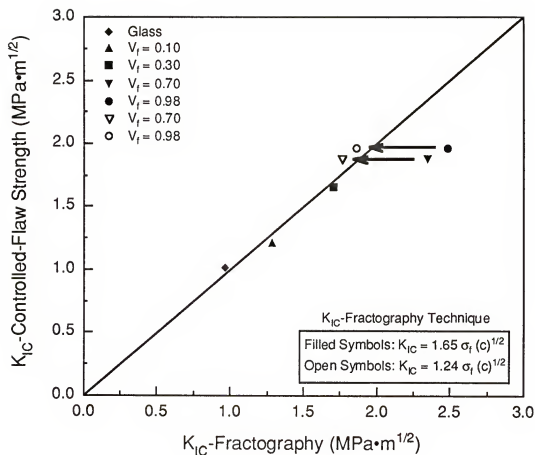


Figure 5.10. Relationship between mean fracture toughness values, calculated using the quantitative fractography method and the controlled-flaw strength method, of lithia disilicate glass-ceramics with $t_n = 4$ h. The line represents $K_{IC}\text{-Fractography} = K_{IC}\text{-Controlled-Flaw Strength}$. The arrows show the residual stress correction in K_{IC} -Fractography resulting from the formation of microcracks.

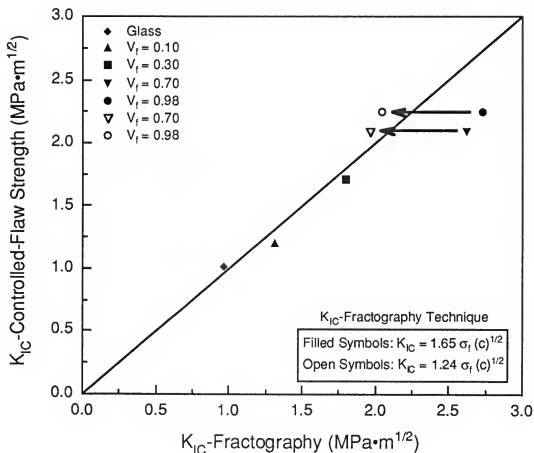


Figure 5.11. Relationship between mean fracture toughness values, calculated using the quantitative fractography method and the controlled-flaw strength method, of lithia disilicate glass-ceramics with $t_n = 10$ h. The line represents $K_{IC}\text{-Fractography} = K_{IC}\text{-Controlled-Flaw Strength}$. The arrows show the residual stress correction in K_{IC} -Fractography resulting from the formation of microcracks.

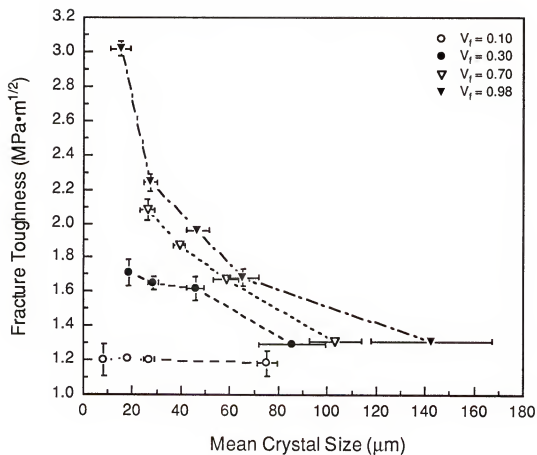


Figure 5.12. Effect of crystal size on the fracture toughness of lithia disilicate glass-ceramics. The error bars represent 95% confidence intervals.

μm , $t_n = 0.25$ h). This corresponds to a decrease of 38% for $V_f = 0.70$ and 57% for $V_f \approx 0.98$. The observed decreases are reasonable when compared to the analytical and experimental results of other investigators (Rose, 1986; Ortiz, 1988; Sung and Nicholson, 1990a and 1990b; Curtain and Futamura, 1990; Cai *et al.*, 1991; Han *et al.*, 1992). Studies by Ortiz, Curtain and Futamura, and Han *et al.* each stated that toughness enhancement derived from crack-tip shielding, *i.e.*, reduction of the effect of applied loading at the crack tip associated with stress-induced microcracking, is counterbalanced by the reduction of toughness in the microcracked material. Han *et al.* also state that significant increases in the microcrack density could result in a significant decrease in material toughness.

5.3.2 Effect of Microcracking on the Mechanical Properties of Lithia Disilicate Glass-Ceramics

It is readily apparent from the experimental results of this study that microcracking plays a vital role in controlling the mechanical behavior of lithia disilicate glass-ceramics. Freiman (1968), Freiman and Hench (1972) and Naman (1994) each noted that microcracks were present in lithia disilicate glass-ceramics with $V_f \geq 0.90$, although none of these investigators attempted to quantify the amount of microcracking, or determine the effect of microcracking on mechanical and physical properties. The microcrack densities of lithia disilicate glass-ceramics analyzed in this study are summarized in Table 4.9 (p. 118) and plotted as a function of crystal volume fraction in Figure 4.30 (p. 119). For each volume fraction the microcrack density increases with decreasing nucleation time. This indicates that the microcrack density is related to crystal size, *i.e.*, a longer nucleation time produces a larger nuclei density and subsequently, a smaller mean crystal size at any given crystal volume fraction.

This finding is in agreement with previous experimental results that were discussed in detail in Chapter 2. Microcrack density is plotted as a function of crystal size in Figure 5.13.

The effect of microcracking on the physical and mechanical behavior of lithia disilicate glass-ceramics is evident in studying the relationship between microcrack density and several properties. The effect of microcrack density on bulk density, elastic modulus and fracture toughness is shown in Figures 5.14 through 5.16. In each relationship, there is a decrease in the material property with increasing microcrack density. These relationships are similar to the relationships between the same material properties and mean crystal size that are plotted in Figures 5.5, 5.7 and 5.12. Again, experimental results indicate a strong relationship between microcracking and crystal size in lithia disilicate glass-ceramics.

The effect of microcracking on the elastic modulus of brittle materials was discussed in a previous section (Section 5.2.4). As mentioned previously, the production of microcracks has been shown to dramatically decrease the elastic modulus of brittle materials. Assuming plane stress conditions, the effect of elastic modulus decrease on K_{IC} can be estimated. For plane stress, the relationship between K_{IC} and E is given by equation (2.31):

$$K_{IC} = \sqrt{2\gamma E}$$

where γ is the fracture surface energy. If γ is assumed to remain constant, then the toughness of a microcracked material ($K_{IC\mu}$) relative to the toughness of a nonmicrocracked material (K_{ICo}) is given by

$$K_{IC\mu} = \left(\frac{E_{\mu}}{E_o} \right)^{1/2} K_{ICo} \quad (5.2)$$

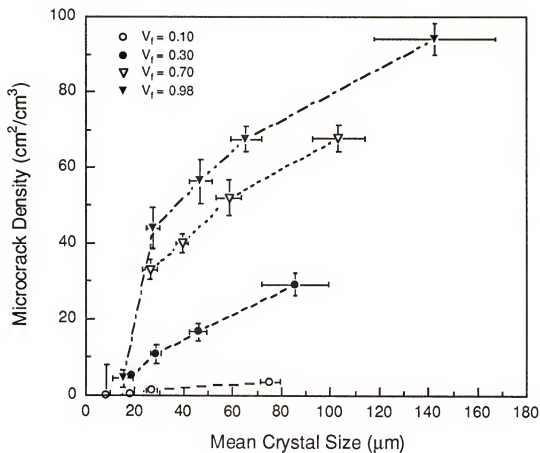


Figure 5.13. Effect of crystal size on the microcrack density of lithia disilicate glass-ceramics. The error bars represent 95% confidence intervals.

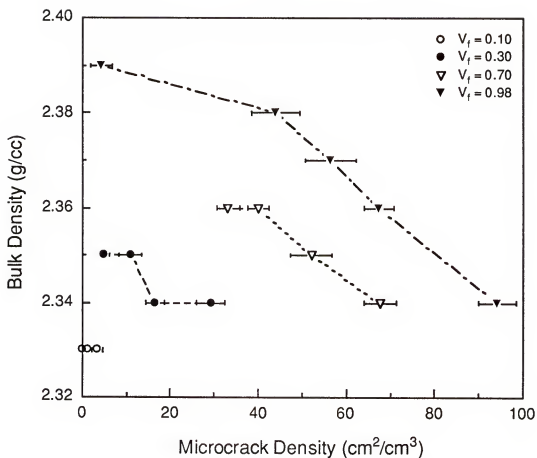


Figure 5.14. Effect of microcrack density on the bulk density of lithia disilicate glass-ceramics. The error bars represent 95% confidence intervals. It is likely that microcracking plays a secondary role to internal porosity in controlling bulk density.

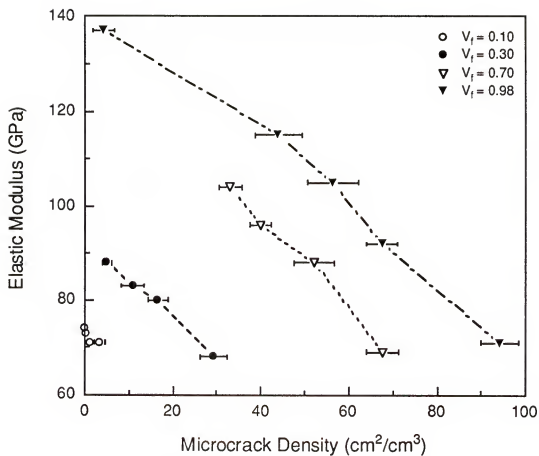


Figure 5.15. Effect of microcrack density on the elastic modulus of lithia disilicate glass-ceramics. The error bars represent 95% confidence intervals.

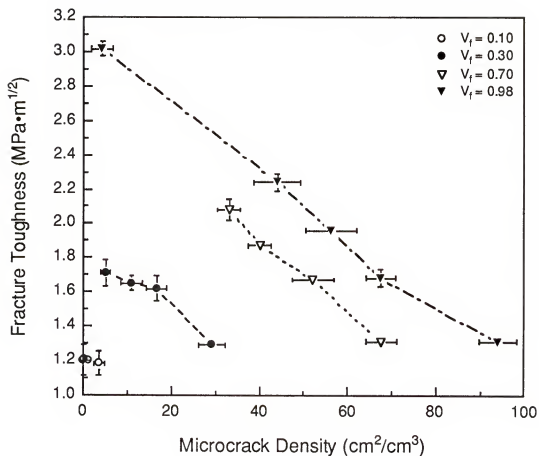


Figure 5.16. Effect of microcracking on the fracture toughness of lithia disilicate glass-ceramics. The error bars represent 95% confidence intervals.

where E_μ is the elastic modulus of the microcracked material and E_0 is the elastic modulus of the nonmicrocracked material. The fracture toughness, based on equation (5.2), of microcracked lithia disilicate glass-ceramics for $V_f \approx 0.98$, along with the experimentally determined fracture toughness, is plotted as a function of microcrack density in Figure 5.17. The decrease in toughness associated only with modulus reduction is not sufficient to explain the fracture toughness values determined experimentally. This implies that the fracture surface energy of lithia disilicate glass-ceramics is also affected by the presence and severity of microcracks.

Stress-induced microcracks were not observed in the lithia disilicate specimens in this study. Although this proposed toughening mechanism is well accepted in the fracture mechanics community, there is very little experimental evidence of its occurrence. In one recent study, Gu *et al.* (1992) documented the presence of microcracks in the vicinity of a crack tip using transmission electron microscopy (TEM) techniques on thin foils cut from double cantilever beam specimens of SiC reinforced with TiB_2 . They discussed the difficulty in preparing specimens for TEM analysis, and in using other microscopy techniques to detect microcracks near a macrocrack tip. Because of the nature of the spherulitic microstructure of lithia disilicate glass-ceramics, it would be extremely difficult to section and prepare thin foils without cracks from preparation for TEM analysis from a specimen containing an arrested macrocrack. In addition the presence of open porosity in the surface of lithia disilicate glass-ceramics with $V_f \geq 0.70$ makes it impossible to use optical or scanning electron microscope techniques to detect the formation of microcracks during slow crack growth or near the tips of indentation cracks. Both of these procedures were attempted with no positive results.

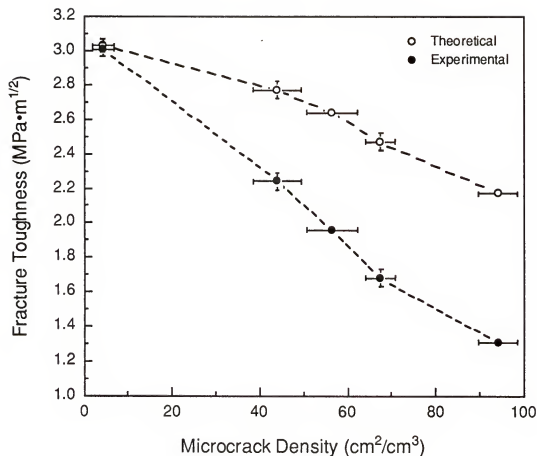


Figure 5.17. Comparison of the fracture toughness of lithia disilicate glass-ceramics with $V_f \approx 0.98$ determined experimentally and determined theoretically using equation (5.2). The theoretical values of K_{IC} are based on modulus reduction associated with microcracking, and do not consider associated changes in fracture surface energy.

Although no evidence of applied stress-induced microcracking was obtained in this study, thin sections, *i.e.*, approximately 50 to 75 μm , of lithia disilicate glass-ceramics with $V_f = 0.10$ and 0.30 revealed the presence of residual stress adjacent to crystals with no collateral damage, *i.e.*, no local microcracking, when observed under polarized light. Observation of the same specimens indicated that residual stress was absent from the area adjacent to crystals possessing radial microcracks. These observations lead to the conclusion that applied stress-induced microcracking is possible in the lithia disilicate system, *i.e.*, the combination of residual and applied stress is sufficient to induce microcracking adjacent to crystals with no collateral damage, or in the vicinity of a propagating macrocrack. Applied stress-induced microcracking likely occurs when the crystal size is just smaller than that necessary to yield spontaneous microcracking during cooling from heat treatment. However, the experimental results of the current study indicate that spontaneous microcracking is the dominant mechanism in the fracture behavior of lithia disilicate glass-ceramics.

5.4 Spontaneous Microcracking

The experimental results of this study support previous results (Cleveland and Bradt, 1978; Singh *et al.*, 1979; Rice *et al.*, 1981; Rice and Freiman, 1981; Krstic, 1984 and 1988; Rose, 1986; Ortiz, 1988; Sung and Nicholson, 1990a and 1990b; Curtin and Futamura, 1990; Cai *et al.*, 1991; Han *et al.*, 1992; Bower and Ortiz, 1993) that concluded that: 1) the formation of spontaneous microcracks is extremely detrimental to the fracture behavior of brittle materials, and 2) the magnitude of spontaneous microcracking is closely related to the grain size. For lithia disilicate glass-ceramics with $V_f \approx 0.98$,

fracture toughness decreases by 57% from $3.02 \text{ MPa}\cdot\text{m}^{1/2}$ to $1.30 \text{ MPa}\cdot\text{m}^{1/2}$ over the range of crystal sizes examined (Figure 5.12). For these same specimens, the microcrack density increases sharply, from $4.3 \pm 2.4 \text{ cm}^2/\text{cm}^3$ to $94.1 \pm 4.3 \text{ cm}^2/\text{cm}^3$, as the crystal size is increased from $15.2 \pm 4.1 \text{ }\mu\text{m}$ to $143 \pm 26.8 \text{ }\mu\text{m}$ (Figure 5.13). The fracture toughness of lithia disilicate glass-ceramics with $V_f \geq 0.30$ decreases in a linear manner as the crystal size is increased (Figure 5.16). These results indicate that the microcrack density is determined by both the crystal size and the crystal volume fraction.

The critical crystal size that will induce spontaneous microcracking in lithia disilicate glass-ceramics can be estimated using the models of Davidge and Green (1968) and Lange (1974). These models are described in detail in Section 2.2.2. In order to use the energy balance criterion derived by Davidge and Green, it must be modified for the microcrack geometry present in lithia disilicate glass-ceramics. The Davidge and Green model was originally derived for a system where the particle is under hydrostatic tension, *i.e.*, $\alpha_p > \alpha_m$, where p and m define the particle and matrix, respectively. This type of thermal mismatch produces radial tensile stress that leads to the formation of circumferential microcracks adjacent to the particle/matrix interface. In lithia disilicate, the crystals are under hydrostatic compression ($\alpha_p < \alpha_m$). This is associated with tangential tensile stress and the formation of radial microcracks in the glass phase.

According to the energy balance model of Davidge and Green, the condition for spontaneous microcracking is given by equation (2.14)

$$U_{SE}f(\phi_f) \geq U_S$$

where U_{SE} is the residual elastic strain energy created by thermal mismatch stress, U_S is the energy required to create fracture surface area, $f(\phi_f)$ is the

fraction of residual strain energy required for crack formation, and ϕ_f is the final normalized crack length ($\phi_f = a/R$). The residual elastic energy is given by equation (2.15):

$$U_{SE} = 2\pi k \sigma_T^2 R^3$$

where σ_T is the thermal stress defined by equation (2.13), R is the crystal radius, and k is a constant defined by equation (2.16). The energy that is required to create fracture surface area, U_S , is given by

$$U_S = \gamma_m A \quad (5.3)$$

where γ_m is the fracture surface energy of the matrix and A is the fracture surface area created by the microcrack. If it is assumed that the residual stress produces an annular crack extending radially around the perimeter of the crystal (Figure 5.18), then the energy necessary to create the fracture surface is

$$U_S = \gamma_m A = 2\gamma_m \pi R^2 (2\phi_f + \phi_f^2) \quad (5.4)$$

If the expressions in equations (2.15) and (5.4) are substituted into equation 2.14, the critical crystal size for spontaneous microcracking to occur is given by

$$R_c = \frac{\gamma_m (2\phi_f + \phi_f^2)}{\sigma_T^2 k f(\phi_f)} \quad (5.5)$$

where R_c is the critical crystal radius for spontaneous microcracking. If the properties of the crystal and matrix and the fabrication temperature, *i.e.*, the annealing temperature, are fixed, then R_c becomes a function of $f(\phi_f)$ and ϕ_f . Using the experimentally determined properties of lithia disilicate glass and fully crystallized lithia disilicate with nominal microcrack density ($t_n = 100$ h, $V_f \approx$

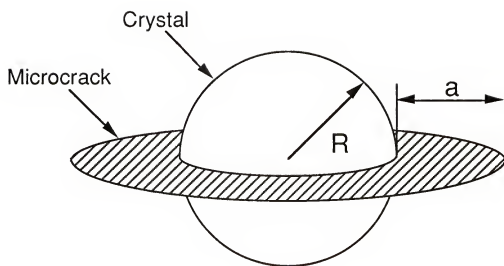


Figure 5.18. Schematic of an annular radial microcrack produced by tangential tensile thermomechanical stress ($\alpha_p < \alpha_m$).

0.98), R_c can be estimated. The critical crystal radius is plotted as a function of the normalized crack length in Figure 5.19.

If the assumption is made that all of the residual strain energy is used in the creation of a microcrack, the critical crystal radius calculated using equation (5.5) increases from 29 μm ($\phi_f = 0.1$) to 412 μm ($\phi_f = 1$). The estimated R_c for $\phi_f = 0.1$ is similar to the mean crystal radius (38 μm) for specimens that were nucleated for 0.25 h with $V_f = 0.10$. These were the only specimens with $V_f = 0.10$ that consistently displayed small densities of microcracks. However, the microcracks observed in these specimens were generally larger than one-tenth the radius of the crystals. As can be seen in Figure 5.19, the critical crystal radius increases rapidly with increasing normalized crack length. In addition, at higher crystal volume fractions ($V_f \geq 0.30$), spontaneous microcrack formation occurred at crystal sizes smaller than that predicted by equation (5.5). The experimental results indicate that this model overestimates the value of R_c . There are several possible explanations for this discrepancy.

One explanation is found in the model geometry. The model assumes a spherical geometry for the crystal. The crystals in the lithia disilicate glass-ceramics were more elliptical in nature. The mean aspect ratio ranged from 1.21 ($t_n = 10$ h, $V_f = 0.30$) to 1.44 ($t_n = 100$ h, $V_f = 0.98$). Results from finite element analysis indicate that the tangential stress adjacent to a crystal that is responsible for microcrack formation, increases with increasing crystal aspect ratio (Figure 4.28). According to equation (5.5), a two-fold increase in the thermal residual stress will decrease the estimated critical particle radius for microcracking by 75%. This would bring the estimated values closer to those observed experimentally. The smallest mean crystal radii that consistently yielded small densities of microcracks in each specimen were: 38 μm ($t_n = 0.25$

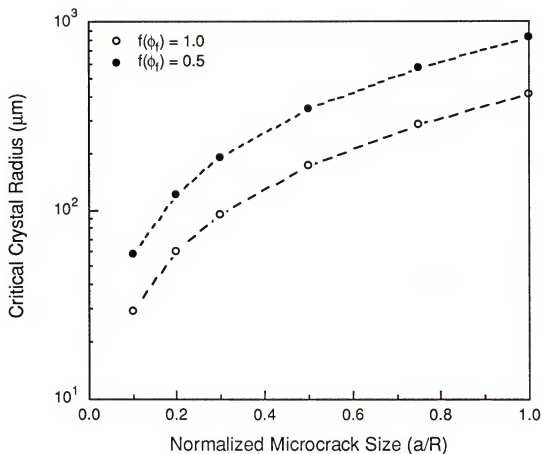


Figure 5.19. Relationship between the theoretical critical crystal radius (R_c) (Davidge and Green, 1968) and normalized microcrack size. Critical crystal radius values were calculated using equation (5.5).

h) for $V_f = 0.10$, $23 \mu\text{m}$ ($t_n = 1.5 \text{ h}$) for $V_f = 0.30$, $13 \mu\text{m}$ ($t_n = 10 \text{ h}$) for $V_f = 0.70$, and $8 \mu\text{m}$ ($t_n = 100 \text{ h}$) for $V_f \approx 0.98$.

A second problem associated with the energetics model of Davidge and Green is that it does not consider the effects of residual stress interaction with adjacent crystals. Finite element analysis revealed a marked increase in thermal residual stress adjacent to a crystal as it was moved closer to a neighboring crystal. For the FEA model used in this study, a maximum tangential stress of 276 MPa was calculated for a crystal spacing of $0.002R$. Closed form solutions using elasticity theory on a simple spherical geometry confirmed the thermal stress values calculated by the FEA model. The large tangential stress values estimated using FEA modeling correspond to very small values of R_c using equation (5.5).

Another model for predicting the critical particle size for spontaneous microcracking is based on a stress intensity approach (Lange, 1974). Using this approach, the condition for crack extension is given by equation (2.20):

$$K_{Rp} \geq K_{ICm}$$

where K_{Rp} is the stress intensity associated with the thermal residual stress and K_{ICm} is the fracture toughness of the matrix phase. For the case of a spherical particle under hydrostatic compression, *i.e.*, $\alpha_p < \alpha_m$, the critical particle size for spontaneous crack extension is given by a rearranged form of equation (2.24):

$$D = \left(\frac{30K_{ICm}^2}{\sigma_{\theta\theta\max}^2} \right)^2 \quad (5.6)$$

where D is the critical particle diameter and $\sigma_{\theta\theta\max}$ is the maximum tangential stress. Estimation of D using the maximum tangential stress computed from finite element analysis and the experimental toughness of lithia disilicate glass

lead to an estimated critical crystal diameter of $0.2\text{ }\mu\text{m}$. This value is much smaller than the observed minimum mean crystal diameter that caused the formation of microcracks in lithia disilicate glass-ceramic specimens with $V_f \approx 0.98$. This model also predicts a critical crystal diameter of $976\text{ }\mu\text{m}$ for a tangential stress of 32 MPa , which is the tangential stress calculated for a lone spherical crystal in a lithia disilicate glass matrix. This value is much larger than the observed minimum mean crystal diameter that caused the formation of microcracks in lithia disilicate glass-ceramics with $V_f = 0.10$. Experimental results suggest that this model overestimates the critical crystal size for spontaneous microcracking in lithia disilicate glass-ceramics with low crystal volume fractions, and underestimates D for high V_f . Again, there are several possible explanations for these discrepancies.

One shortcoming of the stress intensity model is that it is based on an assumption that there is a pre-existing sharp flaw (or flaws) from which a microcrack can propagate. The existence of small flaws in the vicinity of the crystal/matrix interface is a reasonable assumption. However, the model is limited by the requirement that the thermal stresses are unaffected by the existence of these flaws, or that the stresses are unaffected by microcrack propagation. Since the estimated value of critical crystal size, from equation (5.6), is inversely proportional to $\sigma_{\theta\theta\text{max}}^4$, small changes in $\sigma_{\theta\theta\text{max}}$ will cause large changes in the value of D . Another potential problem with this model is that it makes no allowance for local changes in fracture surface energy or elastic modulus. Localized changes, as a result of microcrack formation, in the value of either of these material properties will cause changes in the value of K_{ICm} . As with $\sigma_{\theta\theta\text{max}}$, D is proportional to the fourth power of K_{ICm} . Therefore, small changes in K_{ICm} can cause large changes in the value of D estimated by equation (5.6).

The experimental results of this study indicate that the critical crystal size for spontaneous microcracking is a function of crystal volume fraction and crystal morphology. The finite element results (section 4.4, p. 113) show that thermal stress is affected by both the shape of the crystal and an overlap of stress fields with neighboring crystals. More accurate models should be based on both the volume fraction and morphology of the dispersed phase. As a first order approximation of the effect of volume fraction, V_f , on the critical crystal size, equation (5.5) can be modified in the following manner:

$$R_c = \frac{\gamma_m (2\phi_f + \phi_f^2)}{\sigma_T^2 k_f (\phi_f)} (1 - V_f) \quad (5.7)$$

The critical crystal size estimated by equation (5.7), along with the experimentally observed minimum crystal sizes that yield spontaneous microcracking, is plotted as a function of V_f in Figure 5.20. The values of R_c estimated using equation (5.7) follow a behavior similar to that observed experimentally. The values estimated for $\phi_f = 0.1$ are very close to the experimental results. Equation (5.7) does however underestimate the value of R_c for $V_f \approx 0.98$. However, spontaneous microcracking, although barely measurable, was observed in the fully crystalline ($V_f \approx 0.98$) glass-ceramic specimens with the smallest mean crystal size. It is possible that spontaneous microcracking would be observed in fully crystalline specimens with smaller crystal sizes if these microstructures had been produced. When the large thermal stress values estimated by FEA for multiple crystal geometries are considered, it could be argued that a negligible density of spontaneous microcracks will always be formed at high crystal volume fractions in systems with the degree of thermal mismatch present in the lithia disilicate system. It is concluded from these analyses that modifications to existing models, such as

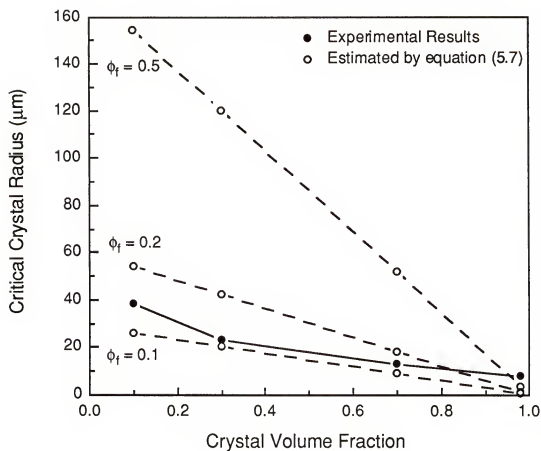


Figure 5.20. Effect of crystal volume fraction on the critical crystal radius necessary for spontaneous microcracking. The theoretical estimates for a normalized microcrack size (ϕ_f) of 0.1 are similar to the values observed experimentally.

that shown in equation (5.7), will give more accurate estimates of the critical particle size for spontaneous microcracking.

5.5 Fractal Analysis

5.5.1 Fractal Analysis of Lithia Disilicate Glass-Ceramics

Statistical analysis showed that the fractal dimensional increment, determined by the atomic force microscopy method, $D^*(AFM)$, of lithia disilicate glass-ceramics increased significantly ($P \leq 0.05$) with increasing crystal volume fraction, from $V_f = 0.10$ to $V_f = 0.70$, for specimens with a nucleation time of 0.25 h, but did not increase significantly ($P > 0.05$) from $V_f = 0.70$ to $V_f \approx 0.98$. For lithia disilicate glass-ceramics with a nucleation time of 1.5 h, $D^*(AFM)$ increased significantly ($P \leq 0.05$) from $V_f = 0.10$ to $V_f \approx 0.98$. For lithia disilicate glass-ceramics with nucleation times of 4 h and 10 h, $D^*(AFM)$ increased significantly ($P \leq 0.05$) from $V_f = 0.30$ to $V_f \approx 0.98$, but did not increase significantly ($P > 0.05$) from $V_f = 0.10$ to $V_f = 0.30$. The $D^*(AFM)$ value for lithia disilicate glass, $D^*(AFM) = 0.09$, was significantly different ($P \leq 0.05$) from the $D^*(AFM)$ values of all lithia disilicate glass-ceramics, except for $V_f = 0.10$ ($t_n = 0.25$ h). There was no statistical difference ($P > 0.05$) between the mean $D^*(AFM)$ values of specimens with different nucleation times ($t_n = 0.25, 1.5, 4$ and 10 h) for crystal volume fractions of 0.10, 0.30 and 0.70, respectively. Statistical differences ($P \leq 0.05$) were determined among the $D^*(AFM)$ values for $V_f \approx 0.98$. The statistical analysis of mean $D^*(AFM)$ values is summarized in Table 4.11. The mean values of $D^*(AFM)$ are plotted as a function of crystal volume fraction in Figure 4.31.

There was no statistical difference ($P > 0.05$) between the fractal dimensional increment values determined by the modified slit island technique, D^* (MSI), and the D^* (AFM) values for lithia disilicate glass-ceramics with the same crystal volume fractions ($t_n = 0.25$, $V_f = 0.10, 0.30, 0.70, 0.98$ and $t_n = 10$ h, $V_f = 0.10, 0.30, 0.70, 0.98$). This result is significant for two reasons. First, the two techniques are quite different. The modified slit island technique (Richardson technique) is based on linear measurement, while the atomic force microscopy technique is based on area measurement. Second, the measurement scales differ by over two orders of magnitude. The AFM technique consists of measurements on the scale of micrometers, while the MSI technique consist of measurements on the scale of hundreds of micrometers. The finding that the D^* values are identical over such a large range of measurement scale provides convincing evidence of the fractal nature of the fracture surfaces of these glass-ceramic materials.

The mean D^* values of specimens analyzed in this study are greater than the values reported previously for mirror region measurements of lithia disilicate glass-ceramics (Naman, 1994), and less than the values reported previously for hackle region measurements of lithia disilicate glass-ceramics (Naman, 1994). The reason for these differences is unclear, although it is possible that measurement error associated with the modified slit island technique could be responsible. Naman suggested that the mirror region analysis he performed involved ruler lengths that were too coarse to provide accurate measurement of the fractal dimension. Therefore, he used the highest measured value of D^* in comparisons of mechanical properties and fractal dimensional increments. The current study employed a minimum of seven ruler sizes to construct the Richardson plots used to determine D^* . The correlation coefficient (r^2), which is a measure of the fit of the data to the first order regression used to calculate D^*

from each of the Richardson plots in this study, was greater than 0.98. This indicates good agreement between the D^* values and the measurements that were used in their calculation. In addition, the MSI data was verified by the AFM data. The accuracy of the Naman data is unknown. These factors lead to the conclusion that the differences between the data of the current study and the Naman study are attributed to potential measurement error in the Naman study. The $D^*(\text{MSI})$ data of the current study and the D^* data of the Naman study are plotted as a function of crystal volume fraction Figure 5.21.

In the current study, no variations in D^* were observed in different mirror, mist and hackle regions of individual specimens analyzed using the atomic force microscopy technique. In a recent study, Kulawansa *et al.* (1993), using AFM analysis of the fracture surface of a silicate glass, concluded that D^* has a maximum value in the mirror region. However, in another recent study, Chen *et al.* (In press) found that D^* is approximately the same in the mirror, mist, and hackle regions, based on AFM fractal analysis on silicon nitride. The results of the current study support the findings of Chen *et al.*

The fact that each group of specimens, *i.e.*, specimens with the same t_n and V_f , analyzed in this study was shown to be fractal and had the same fractal dimension in different regions and on different planes of the fracture surface suggests a self-similar, as opposed to self-affine, fracture behavior for the lithia disilicate system. As discussed in Section 2.3.3, Mecholsky *et al.* (1988) derived an expression for the characteristic length involved in the fracture process. The characteristic length, a_0 , is defined by equation (2.32):

$$a_0 = \frac{2\gamma}{E D^*}$$

where γ and E are the fracture surface energy and elastic modulus of the material, respectively. The characteristic length estimated for the lithia disilicate

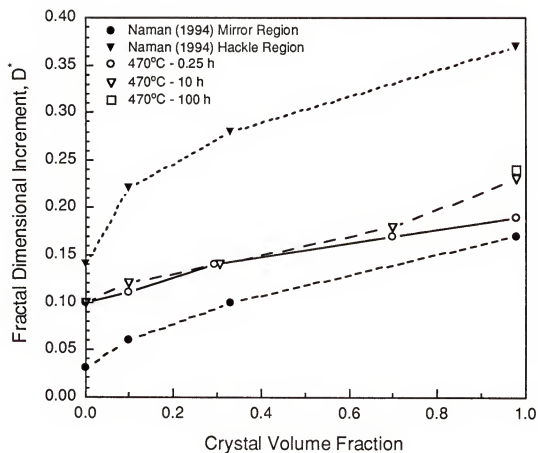


Figure 5.21. Effect of crystallization on the fractal dimensional increment, D^* (MSI), of lithia disilicate glass-ceramics. The D^* (MSI) data of Naman (1994) for mirror and hackle region measurements is also plotted.

specimens in this study ranged from 15.8 Å ($t_n = 4$ h, $V_f \approx 0.98$) to 29.3 Å ($t_n = 1.5$ h, $V_f = 0.30$). Differences in the a_0 values are thought to be a result of the macroscopic measurement of K_{IC} from which γ is obtained. Macroscopic measurement will not necessarily detect events occurring at the atomic level. For example, in lithia disilicate glass-ceramics, the presence of microcracks will cause the fracture toughness and elastic modulus to decrease. The reduced values of these properties can change the calculated value of γ , although atomic processes involved in the fracture process probably remain the same.

If the assumption is made that all the specimens have approximately the same characteristic length, then the characteristic length can be determined by plotting γ as a function of ED^* (equation 2.32). The slope of the line produced by a first order regression is equal to $a_0/2$. A graphical representation of equation (2.32) is shown in Figure 5.22. The value of a_0 determined from regression analysis is 21 Å. The reasonably good fit of the data to the first order regression indicates that fracture is controlled by a similar process at the atomic level in each group of specimens. Unfortunately, atomic resolution could not be achieved with the AFM on the specimens analyzed in this study to verify this finding by an independent technique.

The value of a_0 calculated in this study is larger than the value reported by Naman for lithia disilicate glass-ceramics. Naman reported a value of a_0 of 4.5 Å for lithia disilicate glass-ceramics with volume fractions ranging from 0 to 0.33. The small value of a_0 calculated by Naman is a result of the high values of D^* he reported. If the data for the Naman specimens with $V_f \approx 0.98$ is used in the estimation of a_0 , a value of approximately 11 Å is obtained from a first order regression analysis. This value is closer to the value calculated in this study. The a_0 value reported in this study is also larger than the a_0 values reported previously for various glasses, that ranged from 10 to 14 Å (Mecholsky and

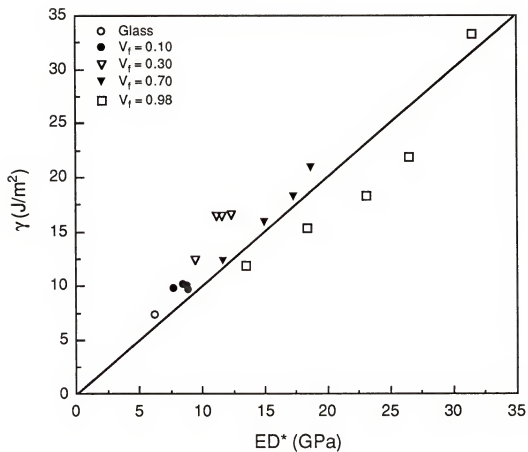


Figure 5.22. Fracture surface energy as a function of ED^* for lithia disilicate glass-ceramics. The value of a_0 obtained from the slope of the first order regression is 21 Å.

Plaia, 1992), and smaller than the characteristic lengths (50 to 70 Å) that have been reported previously for fully crystallized glass-ceramics (Mackin *et al.*, 1987). Although slightly larger, the a_0 value of the specimens in this study is similar to the reported values for glasses. Mecholsky and Plaia hypothesized that the characteristic length of glass implies that its fracture is controlled by the rupture of clusters of open areas in the glass structure. This hypothesis agrees with the molecular dynamics predictions of Swiller *et al.* (In press) that indicate that the fracture follows the path of open structure, approximately 12 to 15 Å, in silica glasses. These previous results, and the results of this study, suggest that the fracture process of lithia disilicate glass-ceramics may be controlled on the atomic level by the rupture of clusters of open structure in the glass phase.

The relationship between fracture toughness and fractal dimensional increment for lithia disilicate glass-ceramics, along with the results reported previously for several brittle materials (Mecholsky *et al.*, 1988; Mecholsky and Mackin, 1988; Mecholsky *et al.*, 1989; Fahmy *et al.*, 1991; Baran *et al.*, 1992), is shown in Figure 5.23. Each line in the K_{IC} vs. D^* plane represents a "family" of materials (equation 2.28). This concept is discussed in more detail in Section 2.3.3. The relationship between fracture toughness and the fractal dimensional increment for the majority of lithia disilicate glass-ceramics analyzed in this study did not correspond to values of K_{IC} and D^* previously reported for fine grained ceramics, such as various aluminas, with grain sizes $\leq 5 \mu\text{m}$ (Mecholsky *et al.*, 1989), for coarse-grained ceramics, such as ZnSe, with average grain sizes $\geq 30 \mu\text{m}$ (Mecholsky *et al.*, 1988), or for glass matrix materials, such as dental porcelains (Baran *et al.*, 1992). However, the fully crystalline lithia disilicate specimens, average crystal size $15.2 \pm 4.1 \mu\text{m}$, that were essentially microcrack free ($t_n = 100 \text{ h}$, $V_f \approx 0.98$) appear to belong to the family that includes fine-grained ceramics. Based on the K_{IC} vs. D^* data, the

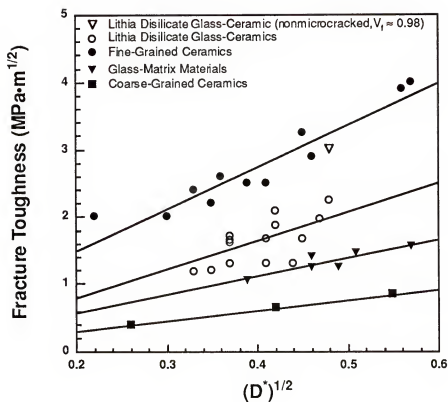


Figure 5.23. Fracture toughness as a function of the fractal dimensional increment, D^* . Each straight line represents a “family” of materials. Please note that the nonmicrocracked lithia disilicate glass-ceramic with $V_f \approx 0.98$ has a K_{IC} vs. D^* relationship similar to relationship observed for fine-grained ceramics.

lithia disilicate glass-ceramics, with the exception of the fully crystalline specimens belonging to the fine-grained ceramics family, appear to represent an independent family of materials. The implication of this result is that the toughening mechanism(s), *i.e.*, primary macroscopic fracture mechanism(s), that control the fracture process of the microcracked lithia disilicate glass-ceramics and the lithia disilicate glass-ceramics with $V_f \leq 0.30$ are different than the mechanism(s) that dominate the non-microcracked lithia disilicate glass-ceramic specimens.

The results for the lithia disilicate materials analyzed in the current study provide new insight into the relationship between fracture toughness and fractal dimension. The a_0 values imply that the majority of the lithia disilicate glass-ceramics and the fully crystalline non-microcracked glass-ceramic have identical fracture behavior on the atomic scale. This further suggests that these materials should have identical fractal dimensions if fractal analysis were performed at the atomic level. Since each glass-ceramic specimen is of the same chemical composition and crystalline structure, the a_0 results appear obvious. The differences in the K_{IC} vs. D^* data for the majority of the lithia disilicate glass-ceramics and the fully crystalline non-microcracked glass-ceramic suggests that these materials are dissimilar. This result can be attributed to the microstructural differences of the two types of materials. The fracture behavior of the microcracked glass-ceramics and the glass-ceramics with $V_f \leq 0.30$ is controlled by crack formation and propagation, such as spontaneous microcracking, within the glass matrix phase, whereas, the fracture behavior of the non-microcracked material appears to be controlled by a transgranular fracture mechanism, such as crack pinning coupled with crack deflection, similar to the fracture behavior observed in many fine-grained ceramic materials.

The current data, as well as previously reported data (Mecholsky *et al.*, 1988; Mecholsky and Mackin, 1988; Mecholsky *et al.*, 1989; Fahmy *et al.*, 1991; Baran *et al.*, 1992), were obtained at the microstructural level, not at the atomic level. This indicates that the relationships given by equations (2.28) and (2.32) are valid for relating the effects of microstructure to the toughness of the material. The fracture toughness data of each of the materials displayed in Figure 5.23 were determined from monolithic specimens dominated by microstructural effects. The relationship between the atomic structure and toughness remains somewhat unclear. The fracture toughness of a material at the atomic level may be different than the fracture toughness measured at the microstructural level. Future studies on this topic should concentrate on measurement of D^* at the atomic level using the atomic force or scanning tunneling microscopes. This type of information should clarify the interrelationship between atomic structure, microstructure, and fracture toughness of brittle materials.

5.5.2 Fractal Analysis of Crystal and Glass Phases in Lithia Disilicate Glass-Ceramics

Statistical analysis showed that the fractal dimensional increment, determined using the atomic force microscopy box counting technique, $D^*(AFM)$, of the crystal phase was significantly greater than that of the glass phase in lithia disilicate glass-ceramics with $V_f \leq 0.30$. The mean $D^*(AFM)$ values measured for the glass phase and crystal phase were 0.09 ± 0.01 and 0.23 ± 0.01 , respectively. The low crystal volume fractions of these specimens allowed for the isolation and analysis of areas on the fracture surface that were composed entirely of one phase. Examples of AFM images of crystal and glass regions on a lithia disilicate glass-ceramic fracture surface are shown in Figures

5.24 and 5.25. An AFM image of a larger portion of the fracture surface from which the images in Figure 5.24 and 5.25 were taken is shown in Figure 5.26. The $D^*(\text{AFM})$ value measured for the larger area shown in Figure 5.26 was 0.14. It should be noted that the $D^*(\text{AFM})$ values reported for the lithia disilicate glass-ceramics, *i.e.*, the composite materials, were determined from sampling larger areas of the fracture surface that encompassed both crystalline and glassy regions. A large volume of this type of data was collected so that the mean values reported earlier were representative of the overall microstructure of these composite materials.

The relationship between the fractal dimensional increment of the composite glass-ceramic and the fractal dimensional increment of the glass and crystal phases was not studied in great detail. Analysis using quantitative stereology on selected two-dimensional AFM images of lithia disilicate glass-ceramics with $V_f \leq 0.30$ indicated that this relationship may follow the rule of mixtures. That is, the D^* value measured for a given glass-ceramic fracture surface area is approximately equal to the sum of the fractional amounts, on a area fraction basis, of the D^* value of each phase. This relationship has the following form:

$$D_{\text{glass-ceramic}}^* = A_{\text{fglass}} D_{\text{glass}}^* + (1 - A_{\text{fglass}}) D_{\text{crystal}}^* \quad (5.8)$$

where A_{fglass} is the area fraction of the glass phase on the selected fracture surface. Additional experimental analysis of the fracture surfaces of many different glass-ceramics and brittle matrix composites is necessary to assess the validity of this proposed relationship.

At present, to the author's knowledge, no other study has reported the fractal dimension of individual phases in composite materials. This is likely a result of the limited measurement techniques that have commonly been used in

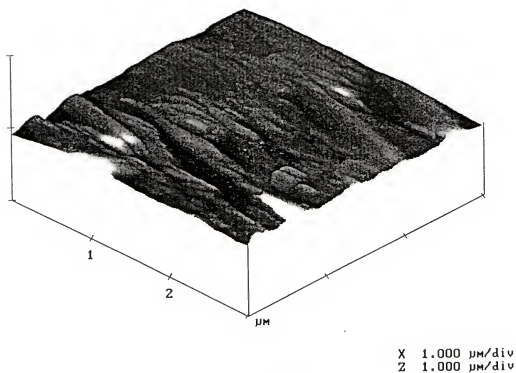


Figure 5.24. AFM image of a 100% glass region on the fracture surface of a lithia disilicate glass-ceramic with $V_f = 0.30$. Please note the relative smoothness of this region in relation to the appearance of the region in Figure 5.25.

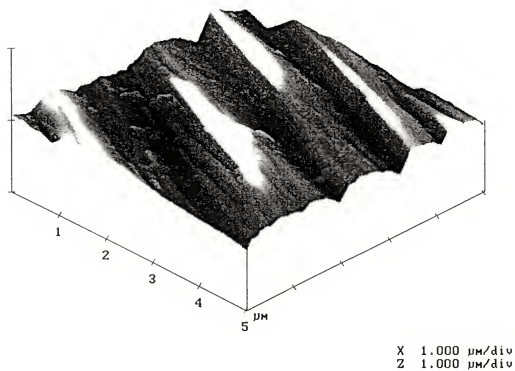


Figure 5.25. AFM image of a 100% crystalline region on the fracture surface of a lithia disilicate glass-ceramic with $V_f = 0.30$. Please note the relative roughness of this region in relation to the appearance of the region in Figure 5.24.

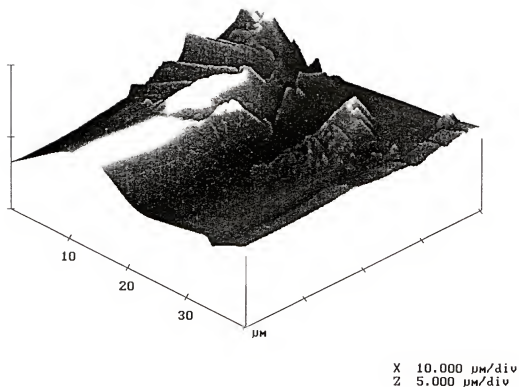


Figure 5.26. AFM image of the fracture surface of a lithia disilicate glass-ceramic with $V_f = 0.30$. The images shown in Figures 5.24 and 5.25 were taken from regions of the fracture surface of this specimen. Please note that the crystal region indicated by arrows is more tortuous than the glass region.

fractal analysis. Until very recently, it was impossible to measure the fractal dimension of fracture surfaces on the scale of a few micrometers. The introduction of scanning tunneling and atomic force microscopes have made this type of measurement possible. However, qualitatively, it appears that crystalline regions in slit island sections are more tortuous than the surrounding glass regions. This phenomenon can be seen in the region of a slit island section of the fracture surface of a lithia disilicate glass-ceramics specimen with $V_f = 0.10$ that is shown in Figure 5.27.

The general consensus has been that the fracture toughness of a brittle material is determined by the location within the microstructure where a crack begins to propagate catastrophically. A study by Jessen and Lewis (1990), using a series of graded composites, showed that if critical propagation was initiated within a glass region, then the composite, regardless of the subsequent microstructure that the crack had to traverse, would have a measured fracture toughness equivalent to the fracture toughness of a 100% glass specimen. The reverse behavior was found when critical propagation was initiated within a composite region, *i.e.*, a region containing the glass matrix and the dispersed phase. For specimens of this type, the measured fracture toughness was equal to the toughness measured in a composite specimen with a homogeneous microstructure. The results of Jessen and Lewis indicate that fracture toughness is determined by the microstructure adjacent to the primary propagating crack at the instant that its propagation becomes catastrophic.

The results of the present study indicate that the fracture toughness of a composite material varies locally depending on the phase through which a crack is forced to propagate. If the fractal dimensional increment is directly related to fracture toughness, as has been theorized, then no variation in fractal dimension should be measured in different regions of the same fracture surface

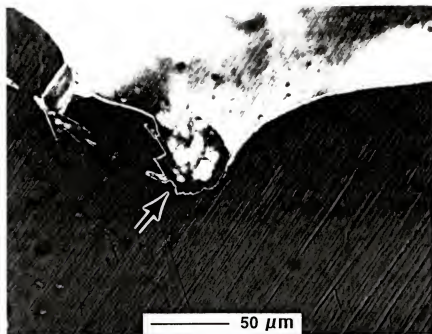


Figure 5.27. Optical image of a section of the slit island coastline of a lithia disilicate glass-ceramic with $V_t = 0.10$. A crystalline region is indicated by the arrow. Note that this region appears more tortuous relative to the adjacent smooth regions of glass.

for a given value of K_{IC} . The difference in fractal dimensional increment values observed in glass and crystal phase regions of lithia disilicate glass-ceramics suggest a different relationship. The $D^*(AFM)$ measurements suggest that the resistance of a composite material to catastrophic crack propagation, *i.e.*, the fracture toughness, does not have a uniform value that depends on the microstructure within which the crack began to propagate catastrophically. The $D^*(AFM)$ measurements further suggest that even after catastrophic crack propagation has begun, local areas of higher toughness provide a higher level of resistance to crack propagation. These findings may indicate that a crack propagating catastrophically can be arrested by interaction with a large volume of tough particles. In fact there is experimental evidence of crack arrest at the interface of a tough second phase material in ductile/brittle laminates (Evans *et al.*, 1990). The hypothesis as it applies to brittle particulate/brittle matrix composites can be tested by analysis of the relationship between fracture toughness and fractal dimensional increment of specimens similar to those described by Jessen and Lewis.

CHAPTER 6 CONCLUSIONS

The objectives of this study were to 1) characterize the effect of crystal volume fraction and crystal size on the fracture toughness of lithia disilicate glass and glass-ceramics with crystal volume fractions ranging from 0 to 0.98, 2) determine how thermal mismatch stresses, developed as a result of the thermal expansion mismatch between lithia disilicate glass and crystalline lithia disilicate, affect the physical and mechanical properties of lithia disilicate glass-ceramics, 3) characterize the relationship between the fracture toughness and the fracture surface fractal dimension of lithia disilicate glass-ceramics to determine the effect of the microstructure on crack propagation, 4) determine the fracture mechanisms that dominate the fracture behavior of lithia disilicate glass-ceramics, and 5) characterize the microstructural parameters that control these mechanisms.

Based on the conditions of this study, the following observations and conclusions can be made.

- (1) For specimens in this study, the fracture toughness increased from $1.01 \pm 0.03 \text{ MPa}\cdot\text{m}^{1/2}$ for lithia disilicate glass to $3.02 \pm 0.04 \text{ MPa}\cdot\text{m}^{1/2}$ for fully crystalline lithia disilicate glass-ceramic ($t_n = 100 \text{ h}$, $V_f \approx 0.98$). The fracture toughness of lithia disilicate glass-ceramics was found to increase with increasing crystal volume fraction except when large densities of microcracks were present. The presence of microcracks, formed as a

result of thermal residual stresses, minimizes the toughening obtained at higher crystal volume fractions.

- (2) The toughening at higher crystal volume fractions is attributed to a crack / microstructure interaction mechanism. The direction of thermal expansion mismatch between the glass and crystal phases produces a stress state within lithia disilicate glass-ceramics under which propagating cracks are drawn, or deflected from the primary fracture plane, toward individual crystals. This factor coupled with experimental evidence of transgranular fracture indicate that the crack interaction mechanism is likely a crack pinning and bowing mechanism.
- (3) Microcrack density and crystal size are directly related in lithia disilicate glass-ceramics. At constant crystal volume fractions > 0.30 , the fracture toughness decreased with increasing mean crystal size. The decrease in fracture toughness is a result of the higher microcrack densities that are associated with larger mean crystal sizes. It is concluded that increasing crystal volume fraction coupled with small crystal size will produce lithia disilicate glass-ceramics with optimal mechanical properties for this system.
- (4) The thermal expansion mismatch between the glass and crystal phases induces spontaneous microcracking in lithia disilicate glass-ceramics with mean crystal sizes above a critical dimension. The critical crystal size changes with crystal volume fraction. The critical crystal radius for detrimental spontaneous microcracking, determined experimentally, decreases from approximately $75\text{ }\mu\text{m}$ for $V_f = 0.10$ to approximately $27\text{ }\mu\text{m}$ for $V_f \approx 0.98$.
- (5) The presence of spontaneous microcracks has a significant effect on the mechanical properties of lithia disilicate glass-ceramics. At a constant

crystal volume fraction, the coefficient of thermal expansion, the elastic modulus and the fracture toughness each decrease with increasing microcrack density. It is concluded that the mean crystal size of lithia disilicate glass-ceramics must be kept below the critical crystal size to derive optimal mechanical performance.

- (6) The data suggest that the fracture behavior of lithia disilicate glass-ceramics is dominated by the occurrence and severity of spontaneous microcracking that occurs as a result of the thermal expansion mismatch between the glass phase and the crystal phase. The experimental data demonstrates that the occurrence of spontaneous microcracks is detrimental to the mechanical behavior of lithia disilicate glass-ceramics.
- (7) The fracture toughness and fracture surface fractal dimensional increment of lithia disilicate glass-ceramics are directly related. The fractal dimensional increment was approximately constant at constant crystal volume fraction, even though the fracture toughness increased with decreasing microcrack density. The fracture toughness and fractal dimensional increment data imply that the lithia disilicate glass-ceramics form a unique family in the K_{IC} versus D' plane, with the exception of the nonmicrocracked fully crystalline lithia disilicate glass-ceramic specimens ($t_n = 100$ h, $V_f \approx 0.98$). The nonmicrocracked fully crystalline specimens appear to belong to the family that includes fine-grained ceramics such as alumina.
- (8) The fractal dimensional increment of the glass and crystal phases of lithia disilicate glass-ceramics was found to be significantly different. This represents a novel finding in the field of fractal analysis. This result implies that even after catastrophic propagation of a primary crack has begun, there are still areas (the dispersed phase) in brittle matrix

composites that exhibit toughness levels higher than that of the matrix or composite. This further suggest that a crack propagating catastrophically can be arrested by interactions with a large volume fraction of tough dispersed particles.

APPENDIX A
FINITE ELEMENT ANALYSIS CODE FOR DETERMINATION OF
THERMAL MISMATCH STRESSES ADJACENT TO A SPHERICAL CRYSTAL
IN A GLASS MATRIX

<u>ANSYS Code</u>	<u>Procedure</u>
1 /FILNAM, sphercry	
2 /TITLE, spherical crystal in glass matrix	
3 /PREP7	enter preprocessor module
4 ET, 1, PLANE 82	2-D 8 node structural solid element type (axisymmetric option chosen)
5 CSYS, 1	select cylindeical coordinate system
6 MP, EX, 1, 70e3	define material 1 properties (glass matrix)
7 MP, NUXY, 1, 0.27	
8 MP, ALPX, 1, 12.8e-6	
9 MP, EX, 2, 145e3	define material 2 properties (crystal)
10 MP, NUXY, 2, 0.20	
11 MP, ALPX, 2, 10.8e-6	
12 K, 1, 0.000, 0.000	define keypoints
13 K, 2, 0.999, 0	
14 K, 3, 0.999, 90	
15 K, 4, 1.001, 0	
16 K, 5, 1.001, 90	
17 K, 6, 3.000, 0	
18 K, 7, 3.000, 90	
19 K, 8, 5.000, 0	
20 K, 9, 5.000, 90	
21 MAT, 1	select material 1
22 A, 6, 7, 8, 9	define area 1
23 ESIZE, , 20	define element size of areas
24 AMESH, 1	generate elements in area 1
25 A, 4, 5, 6, 7	define area 2
26 AMESH, 2	generate elements in area 2
27 MAT, 2	eslect material 2
28 A, 1, 2, 3	define area 3
29 AMESH, 3	generate elements in area 3
30 CSYS, 0	elect cartesian coordinate system
31 NSEL, S, LOC, Y, 0	elect nodes along x-axis
32 D, ALL, UY	specify degree of freedom constraints

33	NSEL, S, LOC, X, 0	at nodes along the x-axis
34	D, ALL, UX	select nodes along the y-axis
		specify degree of freedom constraints
35	CSYS, 1	at nodes along the y-axis
36	NSEL, S, LOC, X, 0.99, 1.01	select cylindrical coordinate system
		select nodes along the interface
37	CPINTF, ALL, 0.01	between the crystal and matrix
		couple nodes along the interface
38	DDELE, ALL	between the crystal and matrix
		delete degree of freedom constraints
		at nodes along the interface between
		the crystal and matrix
39	NSEL, ALL	select all nodes
40	TREF, 450	define initial temperature
41	TUNIF, 25	define final temperature
42	FINISH	
43	/SOLU	enter solution module
44	OUTRES, ALL, ALL	send solution to results file
45	SOLVE	calculate stress distribution

APPENDIX B FINITE ELEMENT ANALYSIS CODE FOR DETERMINATION OF THERMAL MISMATCH STRESSES ADJACENT TO AN ELLIPTICAL CRYSTAL IN A GLASS MATRIX

<u>ANSYS Code</u>	<u>Procedure</u>
1 /FILNAM, ellipcry	
2 /TITLE, elliptical crystal in glass matrix	
3 /PREP7	enter preprocessor module
4 ET, 1, PLANE 82	2-D 8 node structural solid element type (axisymmetric option chosen)
5 CSYS, 0	select cartesian coordinate system
6 MP, EX, 1, 70e3	define material 1 properties (glass matrix)
7 MP, NUXY, 1, 0.27	
8 MP, ALPX, 1, 12.8e-6	
9 MP, EX, 2, 145e3	define material 2 properties (crystal)
10 MP, NUXY, 2, 0.20	
11 MP, ALPX, 2, 10.8e-6	
12 K, 1, 0.000, 0.000	define keypoints
13 K, 2, 1.999, 0.000	
14 K, 3, 0.660, 0.900	
15 K, 4, 0.865, 0.600	
16 K, 5, 0.968, 0.300	
17 K, 6, 0.000, 0.999	
18 K, 7, 1.201, 0.000	
19 K, 8, 0.663, 0.900	
20 K, 9, 0.867, 0.600	
21 K, 10, 0.969, 0.300	
22 K, 11, 1.001, 0.000	
23 K, 12, 0.000, 3.200	
24 K, 13, 1.984, 2.400	
25 K, 14, 2.598, 1.600	
26 K, 15, 2.904, 0.800	
27 K, 16, 3.000, 0.000	
28 K, 17, 0.000, 5.200	
29 K, 18, 5.000, 5.200	
30 K, 19, 5.000, 0.000	
31 L, 1, 2	define lines
32 L, 1, 6	

33	L, 7, 12	
34	L, 11, 16	
35	L, 12, 17	
36	L, 17, 18	
37	L, 18, 19	
38	L, 16, 19	
39	BSPLIN, 2, 3, 4, 5, 6	
40	BSPLIN, 7, 8, 9, 10, 11	
41	BSPLIN, 12, 13, 14, 15, 16	
42	MAT, 1	select material 1
43	AL, 5, 6, 7, 8, 11	define area 1
44	ESIZE, , 20	define element size of areas
45	AMESH, 1	generate elements in area 1
46	AL, 3, 4, 10, 11	define area 2
47	AMESH, 2	generate elements in area 2
48	MAT, 2	select material 2
49	AL, 1, 2, 9	define area 3
50	AMESH, 3	generate elements in area 3
51	NSEL, S, LOC, Y, 0	select nodes along the x-axis
52	D, ALL, UY	specify degree of freedom constraints at nodes along the x-axis
53	NSEL, S, LOC, X, 0	select nodes along the y-axis
54	D, ALL, UX	specify degree of freedom constraints
55	LSEL, S, LINE, , 9, 10	select lines along the interface between the crystal and matrix
56	NSLL, S, 1	select nodes along the interface between the crystal and matrix
57	CPINTF, ALL, 0.01	couple nodes along the interface between the crystal and matrix
58	DDELE, ALL	delete degree of freedom constraints at nodes along the interface between the crystal and matrix
59	NSEL, ALL	select all nodes
60	TREF, 450	define initial temperature
61	TUNIF, 25	define final temperature
62	FINISH	
63	/SOLU	enter solution module
64	OUTRES, ALL, ALL	send solution to results file
65	SOLVE	calculate stress distribution

APPENDIX C FINITE ELEMENT ANALYSIS CODE FOR DETERMINATION OF THERMAL MISMATCH STRESSES ADJACENT TO TWO SPHERICAL CRYSTALS IN A GLASS MATRIX

ANSYS Code

Procedure

1 /FILNAM, twocrys	
2 /TITLE, two spherical crystals in glass matrix	
3 /PREP7	enter preprocessor module
4 ET, 1, PLANE 82	2-D 8 node structural solid element type (axisymmetric option chosen)
5 CSYS, 0	select cartesian coordinate system
6 MP, EX, 1, 70e3	define material 1 properties (glass matrix)
7 MP, NUXY, 1, 0.27	
8 MP, ALPX, 1, 12.8e-6	
9 MP, EX, 2, 145e3	define material 2 properties (crystal)
10 MP, NUXY, 2, 0.20	
11 MP, ALPX, 2, 10.8e-6	
12 K, 1, 0.000, 0.000	define keypoints
13 K, 2, 0.999, 0.000	
14 K, 3, 0.000, 0.999	
15 K, 4, 1.001, 0.000	
16 K, 5, 0.000, 1.001	
17 K, 6, 0.000, 2.001	
18 K, 7, 0.999, 3.000	
19 K, 8, 0.000, 3.999	
20 K, 9, 0.000, 1.999	
21 K, 10, 1.001, 3.000	
22 K, 11, 0.000, 4.001	
23 K, 12, 1.500, 0.000	
24 K, 13, 0.000, 1.500	
25 K, 14, 1.500, 3.000	
26 K, 15, 0.000, 4.500	
27 K, 16, 5.000, 0.000	
28 K, 17, 5.000, 5.000	
29 K, 18, 0.000, 5.000	
30 K, 19, 0.000, 3.000	
31 L, 1, 2	define lines
32 L, 1, 3	

33	L, 4, 12	
34	L, 5, 13	
35	L, 9, 13	
36	L, 8, 19	
37	L, 6, 19	
38	L, 7, 19	
39	L, 10, 14	
40	L, 11, 15	
41	L, 12, 16	
42	L, 16, 17	
43	L, 17, 18	
44	L, 15, 18	
45	LARC, 2, 3, 1, 0.999	
46	LARC, 4, 5, 1, 1.001	
47	LARC, 9, 10, 19, 1.001	
48	LARC, 10, 11, 19, 1.001	
49	LARC, 6, 7, 19, 0.999	
50	LARC, 7, 8, 19, 0.999	
51	LARC, 12, 13, 1, 1.500	
52	LARC, 13, 14, 19, 1.500	
53	LARC, 14, 15, 19, 1.500	
54	MAT, 1	select material 1
55	AL, 11, 12, 13, 14, 21, 22, 23	define area 1
56	ESIZE, , 20	define element size of areas
57	AMESH, 1	generate elements in area 1
58	AL, 3, 4, 16, 21	define area 2
59	AMESH, 2	generate elements in area 2
60	AL, 5, 9, 17, 22	define area 3
61	AMESH, 3	generate elements in area 3
62	AL, 9, 10, 18, 23	define area 4
63	AMESH, 4	generate elements in area 4
64	MAT, 2	select material 2
65	AL, 1, 2, 15	define area 5
66	AMESH, 5	generate elements in area 5
67	AL, 7, 8, 19	define area 6
68	AMESH, 6	generate elements in area 6
69	AL, 6, 8, 20	define area 7
70	AMESH, 7	generate elements in area 7
71	NSEL, S, LOC, Y, 0	select nodes along the x-axis
72	D, ALL, UY	specify degree of freedom constraints at nodes along the x-axis
73	NSEL, S, LOC, X, 0	select nodes along the y-axis
74	D, ALL, UX	specify degree of freedom constraints
75	LSEL, S, P	graphically select lines along the interface between the crystal and matrix
76	NSLL, S, 1	select nodes along the interface between the crystal and matrix
77	CPINTF, ALL, 0.01	couple nodes along the interface

78 DDELE, ALL

between the crystal and matrix
delete degree of freedom constraints
at nodes along the interface between
the crystal and matrix

79 NSEL, ALL

select all nodes

80 TREF, 450

define initial temperature

81 TUNIF, 25

define final temperature

82 FINISH

83 /SOLU

enter solution module

84 OUTRES, ALL, ALL

send solution to results file

85 SOLVE

calculate stress distribution

REFERENCES

- Abdel-Latif AIA, Bradt RC, Tressler RE (1981). "Multiple-Mist Regions on Glass Fracture Surfaces"; in *Fractography and Materials Science*, ASTM STP 733. Gilberston LN, Zipp RD, editors. Philadelphia, PA: American Society for Testing and Materials, pp. 259-270.
- Anstis GR, Chantikul P, Lawn BR, Marshall DB (1981). "A Critical Evaluation of Indentation Techniques for Measuring Fracture Toughness: I, Direct Crack Measurements," *J. Am. Ceram. Soc.*, 64 [9], 533-538.
- Baran GR, Roques-Carmes C, Wehbi D, Degrange M (1992). "Fractal Characteristics of Fracture Surfaces," *J. Am. Ceram. Soc.*, 75 [10], 2687-2691.
- Barsoum M, Zhou O (1988). "Microcracking in Ceramic/Ceramic Composites," *Adv. Ceram. Mater.*, 3 [4], 361-368.
- Beall GH, Duke DA (1983). "Glass-Ceramic Technology"; in *Glass: Science and Technology*, Volume 1. Uhlmann DR, Kreidl NJ, editors. New York, NY: Academic Press, pp. 403-445.
- Bertolotti RL, Fulrath RM (1967). "Effect of Micromechanical Stress Concentrations on Strength of Porous Glass," *J. Am. Ceram. Soc.*, 50 [11], 558-562.
- Binns DB (1962). "Some Physical Properties of Two-Phase Crystal-Glass Solids"; in *Science of Ceramics*, Volume 1. Stewart GH, editor. New York, NY: Academic Press, pp. 315-334.
- Borom MP (1977). "Dispersion-Strengthened Glass Matrices - Glass-Ceramics, A Case in Point," *J. Am. Ceram. Soc.*, 60 [1-2], 17-21.
- Borom MP, Turkalo AM, Doremus RH (1975). "Strength and Microstructure in Lithium Disilicate Glass-Ceramics," *J. Am. Ceram. Soc.*, 58 [9-10], 385-391.
- Bower AF, Ortiz M (1993). "The Influence of Grain Size on the Toughness of Monolithic Ceramics," *ASME Trans.*, 115, 228-236.
- Budiansky B, O'Connell RJ (1976). "Elastic Moduli of a Cracked Solid," *Int. J. Solids Struct.*, 12, 81-97.

- Buresch FE (1978). "A Structure Sensitive K_{Ic} Value and its Dependence on Grain Size Distribution, Density and Microcrack Interaction"; in *Fracture Mechanics of Ceramics*, Volume 4. Bradt RC, Hasselmen DPH, Lange FF, editors. New York, NY: Plenum Press, pp. 835-847.
- Buresch FE, Frye K, Muller T (1983). "Relationship Between Microcrack Zones and Toughness of Fine Grained Alumina and Coarse Grained Graphite"; in *Fracture Mechanics of Ceramics*, Volume 5. Bradt RC, Evans AG, Hasselmen DPH, Lange FF, editors. New York, NY: Plenum Press, pp. 591-608.
- Cai H, Moran B, Faber KT (1991). "Analysis of a Microcrack Prototype and Its Implications for Microcrack Toughening," *J. Am. Ceram. Soc.*, 74 [7], 1695-1698.
- Case ED, Smyth JR, Hunter O (1983). "Microcrack Healing During the Temperature Cycling of Single Phase Ceramics"; in *Fracture Mechanics of Ceramics*, Volume 5. Bradt RC, Evans AG, Hasselmen DPH, Lange FF, editors. New York, NY: Plenum Press, pp. 507-530.
- Case ED (1984). "The Effect of Microcracking Upon the Poisson's Ratio for Brittle Materials," *J. Mater. Sci.*, 19, 3702-3712.
- Chantikul P, Anstis GR, Lawn BR, Marshall DB (1981). "A Critical Evaluation of Indentation Techniques for Measuring Fracture Toughness: II, Strength Method," *J. Am. Ceram. Soc.*, 64 [9], 539-543.
- Charalambides PG, McMeeking RM (1988). "Near-Tip Mechanics of Stress-Induced Microcracking in Brittle Materials," *J. Am. Ceram. Soc.*, 71 [6], 465-472.
- Chen Z, Mecholsky JJ, Joseph T, Beatty CL (In press). "Application of Fractal Fracture to Advanced Engine Material," in *Proceedings of the 5th International Symposium on Ceramic Materials in Components for Engines*. Shanghai, China: Shanghai Institute of Ceramics, Chinese Academy of Sciences.
- Clarke DR, Faber KT (1987). "Fracture of Ceramics and Glasses," *J. Phys. Chem. Solids*, 48 [11], 1115-1157.
- Cleveland JJ, Bradt RC (1978). "Grain Size/Microcracking Relations for Pseudobrookite Oxides," *J. Am. Ceram. Soc.*, 61 [11-12], 478-481.
- Cook RF, Lawn BR (1983). "A Modified Indentation Toughness Technique," *J. Am. Ceram. Soc.*, 66 [11], C200-C201.
- Cornwall B, Krstic VD (1992). "Role of Residual Stress Field Interaction in Strengthening of Particulate-Reinforced Composites," *J. Mater. Sci.*, 27, 1217-1221.

- Curtin WA, Futamura K (1990). "Microcrack Toughening?" *Acta Metall. Mater.*, 38 [11], 2051-2058.
- Davidge RW, Green TJ (1968). "The Strength of Two-Phase Ceramic/Glass Materials," *J. Mater. Sci.*, 3, 629-634
- Davidson DL (1989). "Fracture Surface Roughness as a Gauge of Fracture Toughness: Aluminum-Particulate SiC Composites," *J. Mater. Sci.*, 24, 681-687.
- Devaney RL (1990). *Chaos, Fractals, and Dynamics*. Menlo Park, CA: Addison-Wesley Publishing Company.
- Dolgopolsky A, Karbhari V, Kwak SS (1989). "Microcrack Induced Toughening - An Interaction Model," *Acta Metall.*, 37 [5], 1349-1354.
- Eshelby JD (1957). "The Determination of the Elastic Field of an Ellipsoidal Inclusion, and Related Problems," *Proc. Soc. London A*, 241, 376-396.
- Evans AG (1972). "The Strength of Brittle Materials Containing Second-Phase Dispersions," *Philos. Mag.*, 26 [6], 1327-1344.
- Evans AG (1974). "Fracture Mechanics Determinations"; in *Fracture Mechanics of Ceramics*, Volume 1. Bradt RC, Hasselmen DPH, Lange FF, editors. New York, NY: Plenum Press, pp. 17-48.
- Evans AG (1974). "The Role of Inclusions in the Fracture of Ceramic Materials," *J. Mater. Sci.*, 9, 1145-1152.
- Evans AG (1978). "Microfracture from Thermal Expansion Anisotropy -- I. Single Phase Systems," *Acta Metall.*, 26, 1845-1853.
- Evans AG, Charles EA (1976). "Fracture Toughness Determinations by Indentation," *J. Am. Ceram. Soc.*, 64 [7], 394-398.
- Evans AG, Faber KT (1981). "Toughening of Ceramics by Circumferential Microcracking," *J. Am. Ceram. Soc.*, 59 [7-8], 371-372.
- Evans AG, Faber KT (1984). "Crack-Growth Resistance of Microcracking Brittle Materials," *J. Am. Ceram. Soc.*, 67 [4], 255-260.
- Evans AG, Fu Y (1985). "Some Effects of Microcracks on the Mechanical Properties of Brittle Solids II: Microcrack Toughening," *Acta Metall.*, 33 [8], 1525-1531.
- Evans AG, Rühle M, Dalgleish BJ, Charalambides PG (1990). "The Fracture Energy of Bimaterial Interfaces"; in *Acta--Scripta Metallurgica Proceedings Series*, Volume 4, *Metal--Ceramic Interfaces*. Rühle M, Evans AG, Ashby MF, Hirth JP, editors. New York, NY: Pergamon Press, pp. 345-364.

- Faber KT, Evans AG (1983a). "Crack Deflection Processes -- I. Theory," *Acta Metall.*, 31 [4], 565-576.
- Faber KT, Evans AG (1983b). "Crack Deflection Processes -- II. Experiment," *Acta Metall.*, 31 [4], 577-584.
- Faber KT, Evans AG, Drory MD (1983). "A Statistical Analysis of Crack Deflection as a Toughening Mechanism in Ceramic Materials"; in *Fracture Mechanics of Ceramics*, Volume 6. Bradt RC, Evans AG, Hasselmen DPH, Lange FF, editors. New York, NY: Plenum Press, pp. 77-92.
- Fagherazzi G, Enzo S, Gohardi V, Scarinci (1980). "A Structural Study of Metastable Tetragonal Zirconia in an $\text{Al}_2\text{O}_3\text{-ZrO}_2\text{-Na}_2\text{O}$ Glass-Ceramic System," *J. Mater. Sci.*, 15, 2693-2700.
- Fahmy Y, Russ JC, Koch CC (1991). "Application of Fractal Geometry Measurements to the Evaluation of Fracture Toughness of Brittle Materials," *J. Mater. Res.*, 6 [9], 1856-1861.
- Freiman SW (1968). "The Relation of the Kinetics of Crystallization to the Mechanical Properties of $\text{Li}_2\text{O-2SiO}_2$ Glass-Ceramics," PhD Dissertation, University of Florida, Gainesville, FL.
- Freiman SW, Hench LL (1972). "Effect of Crystallization on the Mechanical Properties of $\text{Li}_2\text{O-SiO}_2$ Glass-Ceramics," *J. Am. Ceram. Soc.*, 55 [2], 186-90.
- Freiman SW, Onoda Jr. GY, Hench LL (1974). "Mechanical Properties of 3BaO-5SiO_2 Glass-Ceramics," *J. Am. Ceram. Soc.*, 57 [1], 8-12.
- Frey WJ, Mackenzie JD (1967). "Mechanical Properties of Selected Glass-Crystal Composites," *J. Mater. Sci.*, 2, 124-130.
- Green AE, Sneddon IN (1950). "Stress Intensity Factors for Elliptical Cracks," *Proc. Cambridge Philos. Soc.*, 46, 159-163.
- Green DJ (1983). "Microcracking Mechanisms in Ceramics"; in *Fracture Mechanics of Ceramics*, Volume 5. Bradt RC, Evans AG, Hasselman DPH, Lange F, editors. New York, NY: Plenum Press, pp. 457-478.
- Green DJ (1981). "Stress-Induced Microcracking at Second-Phase Inclusions," *J. Am. Ceram. Soc.*, 64 [3], 138-141.
- Green DJ, Nicholson PS (1978). "Some Effects of Dispersed Phases on the Fracture Behavior of Glass"; in *Fracture Mechanics of Ceramics*, Volume 4. Bradt RC, Hasselman DPH, Lange F, editors. New York, NY: Plenum Press, pp. 945-960.

- Goodier JN (1933). "Concentration of Stress Around Spherical and Cylindrical Inclusion and Flaws," *J. Appl. Mech.*, 1, 39-44.
- Grossman DG (1982). "Glass-Ceramic Applications"; in *Advances in Ceramics, Volume 4, Nucleation and Crystallization in Glasses*. Simmons JH, Uhlmann DR, Beall GH, editors. Columbus, OH: American Ceramic Society, pp. 249-260.
- Gu WH, Faber KT, Steinbrech RW (1992). "Microcracking and R-Curve Behavior in SiC-TiB₂ Composites," *Acta Metall. Mater.*, 40 [11], 3121-3128.
- Han LX, Warren R, Suresh S (1992). "An Experimental Study of Toughening and Degradation Due to Microcracking in a Ceramic Composite," *Acta Metall.*, 40 [2], 259-274.
- Hasselman DPH, Fulrath RM (1965). "Effect of Alumina Dispersions on Young's Modulus of a Glass," *J. Am. Ceram. Soc.*, 48 [4], 218-219.
- Hasselman DPH, Fulrath RM (1966). "Proposed Fracture Theory of a Dispersion-Strengthened Glass Matrix," *J. Am. Ceram. Soc.*, 49 [2], 68-72.
- Hasselman DPH, Fulrath RM (1967). "Micromechanical Stress Concentrations in Two-Phase Brittle-Matrix Ceramic Composites," *J. Am. Ceram. Soc.*, 50 [8], 339-404.
- Hing P, McMillan PW (1973). "The Strength and Fracture Properties of Glass-Ceramics," *J. Mater. Sci.*, 8, 1041-1048.
- Hutchinson JW (1987). "Crack Tip Shielding by Microcracking in Brittle Solids," *Acta Metall.*, 35 [7], 1605-1606.
- Irwin GR, Paris PC (1971). "Fundamental Aspects of Crack Growth and Fracture"; in *Fracture III*. Liebowitz H, editor. New York, NY: Plenum Press, pp. 2-46.
- Ito YM, Rosenblatt M, Cheng LY, Lange FF, Lange AG (1981). "Cracking in Particulate Composites Due to Thermomechanical Stress," *Int. J. Fract.*, 17 [5], 483-491.
- Jessen TL, Lewis D, III (1990). "Fracture Toughness of Graded Metal-Particulate/Brittle-Matrix Composites," *J. Am. Ceram. Soc.*, 73 [5], 1405-1408.
- Käse HR, Tesk JA, Case ED (1985). "Elastic Constants of Two Dental Porcelains," *J. Mater. Sci.*, 20, 524-531.
- Knehens R, Steinbrech R (1982). "Memory Effect of Crack Resistance During Slow Crack Growth in Notched Al₂O₃ Bend Specimens," *J. Mater. Sci. Lett.*, 1 [8], 327-329.

- Krstic VD (1984). "Fracture of Brittle Solids in the Presence of Thermoelastic Stresses," *J. Am. Ceram. Soc.*, 67 [9], 589-593.
- Krstic VD (1988). "Grain-Size Dependence of Fracture Stress in Anisotropic Brittle Solids," *J. Mater. Sci.*, 23, 259-266.
- Kulawansa DM, Jensen LC, Langford SC, Dickinson JT (1993). "Scanning Tunneling Microscope Observation of the Mirror Region of Silicate Glass Fracture Surfaces," *J. Mater. Res.*, 10, 1123-1135.
- Kuszyk JA, Brandt RC (1973). "Influence of Grain Size on Effects of Thermal Expansion Anisotropy in MgTi_2O_5 ," *J. Am. Ceram. Soc.*, 56 [8], 420-423.
- Lange FF (1970). "The Interaction of a Crack Front with a Second-Phase Dispersion," *Philos. Mag.*, 22 [179], 983-992.
- Lange FF (1971). "Fracture Energy and Strength Behavior of a Sodium Borosilicate Glass- Al_2O_3 Composite System," *J. Am. Ceram. Soc.*, 54 [12], 614-620.
- Lange FF (1974). "Criteria for Crack Extension and Arrest in Residual, Localized Stress Fields Associated with Second Phase Particles"; in *Fracture Mechanics of Ceramics*, Volume 2. Bradt RC, Hasselmen DPH, Lange FF, editors. New York, NY: Plenum Press, pp. 599-613.
- Lange FF (1978). "Fracture Mechanics and Microstructural Design"; in *Fracture Mechanics of Ceramics*, Volume 4. Bradt RC, Hasselmen DPH, Lange FF, editors. New York, NY: Plenum Press, pp. 799-819.
- Lawn BR, Evans AG, Marshall DB (1980). "Elastic/Plastic Indentation Damage in Ceramics: The Median/Radial Crack System," *J. Am. Ceram. Soc.*, 63 [9-10], 574-581.
- Lawn BR, Marshall DB (1979). "Hardness, Toughness, and Brittleness: An Indentation Analysis," *J. Am. Ceram. Soc.*, 62 [7-8], 347-350.
- Lewis D, III (1981). "Fracture Strength and Mirror Size in a Commercial Glass-Ceramic," *J. Am. Ceram. Soc.*, 64 [2], 82-86.
- Mackert JR, Rueggeberg FA, Lockwood PE, Evans AL, Thompson WO (1994). "Isothermal Anneal Effect on Microcrack Density around Leucite Particles in Dental Porcelain," *J. Dent. Res.*, 73 [6], 1221-1227.
- Mandelbrot BB (1982). *The Fractal Geometry of Nature*. San Francisco, CA: W.H. Freeman.
- Mandelbrot BB, Passoja DE, Paulley AJ (1984). "Fractal Character of Fracture Surface of Metals," *Nature (London)*, 308 [5961], 721-722.

- Marotta A, Buri A, Branda F, Saiello S (1982). "Nucleation and Crystallization of $\text{Li}_2\text{O} \cdot 2\text{SiO}_2$ Glass - a DTA Study"; in *Advances in Ceramics, Volume 4, Nucleation and Crystallization in Glasses*. Simmons JH, Uhlmann DR, Beall GH, editors. Columbus, OH: American Ceramic Society, pp. 146-152.
- Marshall DB, Lawn BR (1979). "Residual Stress Effects in Sharp-Contact Cracking," *J. Mater. Sci.*, 14 [8], 2001-2012.
- Marshall DB, Noma T, Evans AG (1983). "A Simple Method for Determining Elastic-Modulus-to-Hardness Ratios using Knoop Indentation Measurements," *J. Am. Ceram. Soc.*, 65 [10], C175-C176.
- McMillan PW (1979). *Glass-Ceramics*. New York, NY: Academic Press.
- Mecholsky JJ (1982). "Fracture Mechanics Analysis of Glass-Ceramics"; in *Advances in Ceramics, Volume 4, Nucleation and Crystallization in Glasses*. Simmons JH, Uhlmann DR, Beall GH, editors. Columbus, OH: American Ceramic Society, pp. 261-276.
- Mecholsky JJ (1983). "Toughening in Glass-Ceramics through Microstructural Design"; in *Fracture Mechanics of Ceramics*, Volume 6. Bradt RC, Evans AG, Hasselman DPH, Lange FF, editors. New York, NY: Plenum Press, pp. 165-180.
- Mecholsky JJ (1991). "Quantitative Fractography: An Assessment"; in *Ceramic Transactions, Volume 17, Fractography of Glasses and Ceramics II*. Frechette VD, Varner JR, editors. Westerville, OH: American Ceramic Society, pp. 413-451.
- Mecholsky JJ, Freiman SW, Rice RW (1974). "Prediction of Fracture Energy and Flaw Size in Glasses from Measurements of Flaw Size," *J. Am. Ceram. Soc.*, 57 [10], 440-443.
- Mecholsky JJ, Freiman SW, Rice RW (1976). "Fracture Surface Analysis of Ceramics," *J. Mater. Sci.*, 11, 1310-1319.
- Mecholsky JJ, Freiman SW (1977). "Effect of Surface Finish on the Strength and Fracture of Glass"; in *International Congress on Glass*. Prague, Czechoslovakia: CVTS Dum Techniky Praha, pp. 489-497.
- Mecholsky JJ, Freiman SW, Rice RW (1977). "Effect of Grinding on Flaw Geometry and Fracture of Glass," *J. Am. Ceram. Soc.*, 60 [3-4], 114-117.
- Mecholsky JJ, Freiman SW, Rice RW (1978). "Fractographic Analysis of Ceramics"; in *Fractography in Failure Analysis*, ASTM STP 645. Strauss BM, Cullen WH, editors. Philadelphia, PA: American Society for Testing and Materials, pp. 363-379.

- Mecholsky JJ, Freiman SW (1991). "Relationship between Fractal Geometry and Fractography," *J. Am. Ceram. Soc.*, 74 [12], 3136-3138.
- Mecholsky JJ, Mackin TJ (1988). "Fractal Analysis of Fracture in Ocala Chert," *J. Mater. Sci. Lett.*, 7, 1145-1147.
- Mecholsky JJ, Mackin TJ, Passoja DE (1986). "Crack Propagation in Brittle Materials as a Fractal Process"; in *Fractal Aspects of Materials*. Laibowitz RB, Mandelbrot BB, Passoja DE, editors. Pittsburgh, PA: Materials Research Society, pp. 5-7.
- Mecholsky JJ, Mackin TJ, Passoja DE (1988). "Self-Similar Crack Propagation in Brittle Materials"; in *Advances in Ceramics, Volume 22, Fractography of Glasses and Ceramics*. Varner J, Frechette VD, editors. Westerville, OH: American Ceramic Society, pp. 127-134.
- Mecholsky JJ, Passoja DE (1985). "Fractals and Brittle Fracture"; in *Fractal Aspects of Materials*. Laibowitz RB, Mandelbrot BB, Passoja DE, editors. Pittsburgh, PA: Materials Research Society, pp. 117-119.
- Mecholsky JJ, Passoja DE, Feinberg-Ringel KS (1989). "Quantitative Analysis of Brittle Fracture Surfaces using Fractal Geometry," *J. Am. Ceram. Soc.*, 72 [1], 60-65.
- Mecholsky JJ, Plaia JR (1992). "Fractal Analysis on Fracture Surfaces of Glass using Replication Techniques," *J. Non-Cryst. Solids*, 146, 249-255.
- Miyata N, Jinno H (1972). "Theoretical Approach to the Fracture of Two-Phase Glass-Crystal Composites," *J. Mater. Sci.*, 7, 973-982.
- Miyata N, Tanigawa K, Jinno H (1983). "Fracture Behavior of Glass Matrix/Glass Particulate Composites"; in *Fracture Mechanics of Ceramics*, Volume 5. Bradt RC, Evans AG, Hasselmen DPH, Lange FF, editors. New York, NY: Plenum Press, pp. 609-623.
- Morena R, Nihara K, Hasselman DPH (1983) "Effect of Crystallites on Surface Damage and Fracture Behavior of a Glass-Ceramics," *J. Am. Ceram. Soc.*, 66 [10], 673-682.
- Nadeau JS, Bennett RC (1978). "Some Effects of Dispersed Phases on the Fracture Behavior of Glass"; in *Fracture Mechanics of Ceramics*, Volume 4. Bradt RC, Hasselmen DPH, Lange FF, editors. New York, NY: Plenum Press, pp. 961-972.
- Nadeau JS, Dickson JI (1980). "Effects of Internal Stresses Due to a Dispersed Phase on the Fracture Toughness of Glass," *J. Am. Ceram. Soc.*, 63 [9-10], 517-523.

- Naman A (1994). "Mechanical Property and Fractal Determination in $\text{Li}_2\text{O} \cdot 2\text{SiO}_2$ Glass-Ceramics," M.S. Thesis, University of Florida, Gainesville, FL.
- Nivas Y, Fulrath RM (1968). "Limitation of Griffith Flaws in Glass-Matrix Composites," *J. Am. Ceram. Soc.*, 53 [4], 188-191.
- Ortiz M (1988). "Microcrack Coalescence and Macroscopic Crack Growth Initiation in Brittle Solids," *Int. J. Solids Struct.*, 24 [3], 231-250.
- Palmer RA, Hench LL (1984). "Fracture Mechanics and Failure Predictions for $\text{Li}_2\text{O} \cdot 2\text{SiO}_2$ Glass and Glass-Ceramics"; in *Ultrastructure Processing of Advanced Structural and Electronic Materials*. Hench LL, editor. Park Ridge, NJ: Noyes Publications, pp. 53-84.
- Pande CS, Richards LE, Louat N, Dempsey BD, Schwoeble (1987). "Fractal Characterization of Fractured Surfaces," *Acta metall.*, 35 [7], 1633-1637.
- Parsell D (1993). "The Optimization of Glass-Ceramic Heat-Treatment Schedules," Ph.D. Dissertation, University of Florida, Gainesville, FL.
- Poncelet EF (1958). "The Markings on Fracture Surfaces," *Trans. Soc. Glass Tech.*, 52, 279-288.
- Randall PN (1967). "Plain Strain Crack Toughness of High Strength Metallic Materials"; in *ASTM STP 410*. Washington: American Society for Testing and Materials, pp. 88-126.
- Ravi-Chandar K, Knauss WG (1984). "An Experimental Investigation into Dynamic Fracture: II. Microstructural Aspects," *Inter. J. Fract.*, 28, 65-80.
- Ray CS, Day DE (1990). "Determining the Nucleation Rate Curve for Lithium Disilicate Glass by Differential Thermal Analysis," *J. Am. Ceram. Soc.*, 73 [2], 439-442.
- Rice RW (1989). "Relation of Tensile Strength-Porosity Effects in Ceramics to Porosity Dependence of Young's Modulus and Fracture Energy, Porosity Character and Grain Size," *Mater. Sci. Eng.*, A112, 215-224.
- Rice RW, Pohanka RC (1979). "Grain-Size Dependence of Spontaneous Cracking in Ceramics," *J. Am. Ceram. Soc.*, 62 [11-12], 559-563.
- Rice RW, Freiman SW, Becher PF (1981). "Grain-Size Dependence of Fracture Energy in Ceramics: I, Experiment," *J. Am. Ceram. Soc.*, 64 [6], 345-350.
- Rice RW, Freiman SW (1981). "Grain-Size Dependence of Fracture Energy in Ceramics: II, A Model for Nocubic Materials" *J. Am. Ceram. Soc.*, 64 [6], 350-354.

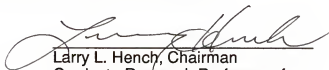
- Rose LRF (1986). "Effective Fracture Toughness of Microcracked Materials," *J. Am. Ceram. Soc.*, 69 [3] 212-214.
- Selsing J (1961). "Internal Stresses in Ceramics," *J. Am. Ceram. Soc.*, 44 [8], 419.
- Singh JP, Virkar AV, Shetty DK, Gordon RS (1979). "Strength-Grain Size Relations in Polycrystalline Ceramics," *J. Am. Ceram. Soc.*, 62 [3-4], 179-183.
- Sproull JF, Rindone GE (1973). "Correlation Between Strength of Glass and Glassy Microphases," *J. Am. Ceram. Soc.*, 56 [2], 102-103.
- Stett MA, Fulrath RM (1968). "Strengthening by Chemical Bonding in Brittle Matrix Composite," *J. Am. Ceram. Soc.*, 51 [10], 599-600.
- Stett MA, Fulrath RM (1970). "Mechanical Properties and Fracture Behavior of Chemically Bonded Composites," *J. Am. Ceram. Soc.*, 53 [1], 5-13.
- Strnad Z (1986). *Glass-Ceramic Materials -- Liquid Phase Separation, Nucleation and Crystallization in Glasses*. New York, NY: Elsevier Science Publishing Co.
- Sung J, Nicholson PS (1990a). "Inclusion-Initiated Fracture Model for Ceramics," *J. Am. Ceram. Soc.*, 73 [3], 639-644.
- Sung J, Nicholson PS (1990b). "Residual-Stress-Defect-Severity Relationships in Ceramics," *J. Am. Ceram. Soc.*, 73 [5], 1318-1322.
- Swanson PL, Fairbanks CJ, Lawn BR, Mai Y, Hockey BJ (1987). "Crack-Interface Grain Bridging as a Fracture Resistance Mechanism in Ceramics: I, Experimental Study on Alumina," *J. Am. Ceram. Soc.*, 70 [4], 289-294.
- Swearengen JC, Beauchamp EK, Eagan RJ (1978). "Fracture Toughness of Reinforced Glasses"; in *Fracture Mechanics of Ceramics*, Volume 4. Bradt RC, Hasselmen DPH, Lange FF, editors. New York: Plenum Press, pp. 973-987.
- Swiller TP, Simmons JH, Wright AC (In press). "Molecular Dynamics Study of Brittle Fracture in Silica Glass and Cristobalite," *J. Non Cryst. Solids*.
- Takayasu H (1990). *Fractals in the Physical Sciences*. New York, NY: John Wiley & Sons.
- Thompson JY, Anusavice KJ (1994). "Effect of Surface Etching on the Flexure Strength and Fracture Toughness of Dicot® Disks Containing Controlled Flaws," *J. Dent. Res.*, 73 [2], 505-510.

- Thompson JY, Mecholsky JJ, Anusavice KJ, Balasubramaniam B (1995). "The Effect of Microcracking on the Fracture Toughness and Fractal Dimension of Lithia-Based Glass-Ceramics," *J. Am. Ceram. Soc.*, submitted.
- Tsai YL, Mecholsky JJ (1991). "Fractal Fracture of Single Crystal Silicon," *J. Mater. Res.*, 6 [6], 1248-1263.
- Tvergaard V, Hutchinson JW (1988). "Microcracking in Ceramics Induced by Thermal Expansion or Elastic Anisotropy," *J. Am. Ceram. Soc.*, 71 [3], 157-166.
- Underwood EE (1970). *Quantitative Stereology*. Reading, MA: Addison-Wesley Publishing Company.
- Utsumi Y, Sakka S (1970). "Strength of Glass-Ceramics Relative to Crystal Size," *J. Am. Ceram. Soc.*, 53 [5], 286-287.
- Venkateswaran A, Donaldson KY, Hasselman DPH (1988). "Role of Intergranular Damage-Induced Decrease in Young's Modulus in the Nonlinear Deformation and Fracture of an Alumina at Elevated Temperatures," *J. Am. Ceram. Soc.*, 71 [7], 565-576.
- Wachtman, JB, Capps W, Mandel J (1972). "Biaxial Flexure Tests of Ceramic Substrates," *J. Mater.*, 7 [2], 188-194.
- Wantanabe A, Imada Y, Kihara S (1986). "Periodic Accumulation of Voids Observed in Calcium Phosphate Glass-Ceramics," *J. Am. Ceram. Soc.*, 69 [2], C31-C32.
- Wantanabe A, Imada Y, Kihara S (1989). "Preparation of Void-Free Calcium Phosphate Glass-Ceramics," *J. Am. Ceram. Soc.*, 72 [8], 1499-1500.
- Wu CC, Freiman SW, Rice RW, Mecholsky JJ (1978). "Microstructural Aspects of Crack Propagation in Ceramics," *J. Mater. Sci.*, 13, 2659-2670.

BIOGRAPHICAL SKETCH

Jeffrey Yates Thompson was born in Westover, Massachusetts on November 9, 1964. After high school, he entered the University of Florida in 1982. He received a Bachelor of Science in Chemical Engineering degree in 1986, and then worked as a process engineer for Milliken and Company in LaGrange, Georgia until August 1988. Mr. Thompson entered the Materials Science and Engineering graduate program at the University of Florida in the fall of 1988. On May 15, 1993, he married Maria Ruth Haridas in Ft. Lauderdale, Florida. Upon receiving his Doctor of Philosophy degree, Mr. Thompson will be employed as an Assistant Professor in the Department of Operative Dentistry at the University of North Carolina at Chapel Hill.

I certify that I have read this study and that in my opinion it conforms to acceptable standards of scholarly presentation and is fully adequate, in scope and quality, as a dissertation for the degree of Doctor of Philosophy.



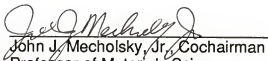
Larry L. Hench, Chairman
Graduate Research Professor of
Materials Science and Engineering

I certify that I have read this study and that in my opinion it conforms to acceptable standards of scholarly presentation and is fully adequate, in scope and quality, as a dissertation for the degree of Doctor of Philosophy.



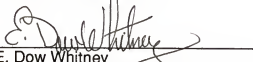
Kenneth J. Anusavice, Cochairman
Professor of Materials Science
and Engineering

I certify that I have read this study and that in my opinion it conforms to acceptable standards of scholarly presentation and is fully adequate, in scope and quality, as a dissertation for the degree of Doctor of Philosophy.



John J. Mecholsky, Jr., Cochairman
Professor of Materials Science
and Engineering

I certify that I have read this study and that in my opinion it conforms to acceptable standards of scholarly presentation and is fully adequate, in scope and quality, as a dissertation for the degree of Doctor of Philosophy.



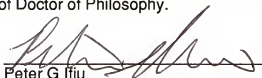
E. Dow Whitney
Professor of Materials Science
and Engineering

I certify that I have read this study and that in my opinion it conforms to acceptable standards of scholarly presentation and is fully adequate, in scope and quality, as a dissertation for the degree of Doctor of Philosophy.



Arthur E. Clark, Jr.
Professor of Materials Science
and Engineering

I certify that I have read this study and that in my opinion it conforms to acceptable standards of scholarly presentation and is fully adequate, in scope and quality, as a dissertation for the degree of Doctor of Philosophy.



Peter G. Ijju
Assistant Professor of Aerospace
Engineering, Mechanics, and
Engineering Science

This dissertation was submitted to the Graduate Faculty of the College of Engineering and to the Graduate School and was accepted as partial fulfillment of the requirements for the degree of Doctor of Philosophy.

May, 1995



Winfred M. Phillips
Dean, College of Engineering

Karen A. Holbrook
Dean, Graduate School